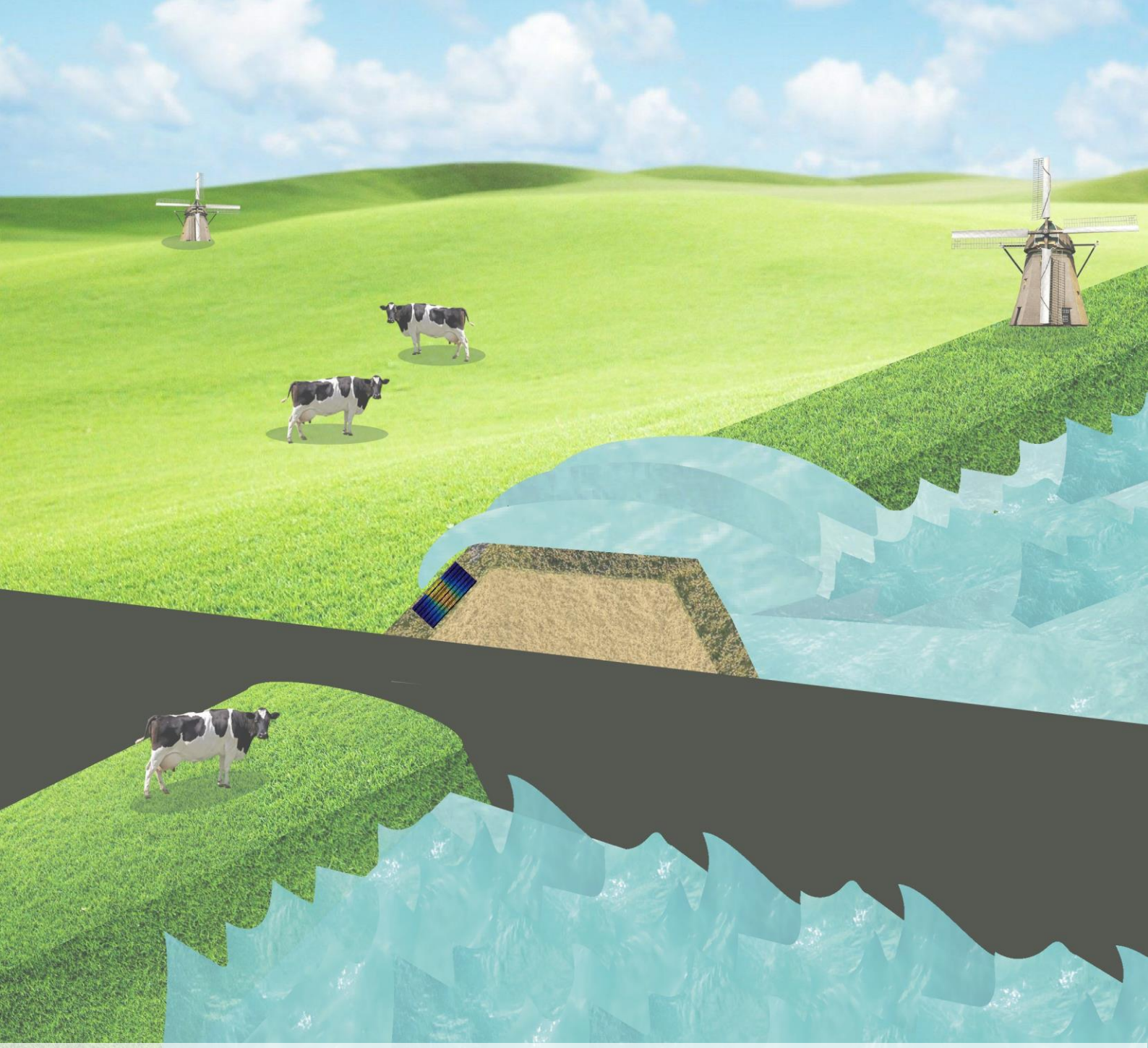

2D modelling of initiation of failure of a clay slope under wave overtopping load

A.B. (Bart) van Langevelde

TU Delft

INFRAM HYDREN
Hydraulic Engineering, Innovation & Research

Hydraulic Engineering

2D modelling of initiation of failure of a clay slope under wave overtopping load

In partial fulfillment of the degree of Master of Science at the Delft University of Technology, to be defended publicly on August 21, 2018.

August 8, 2018

Author

A.B. (Bart) van Langevelde

4169557

Thesis committee

Prof. dr. ir. S.G.J. Aarninkhof	TU Delft, Section Coastal Engineering
Dr. ir. M. van Damme	TU Delft, Section Hydraulic Structures and Flood Risk
Dr. ir. B. Hofland	TU Delft, Section Hydraulic Structures and Flood Risk
Ir. G.J. Steendam	Infram
Ir. R. Joustra	Infram

Faculty of Civil Engineering

Coastal Engineering Section

Delft University of Technology

Preface

This master thesis is the final act of my study Hydraulic Engineering at the TU Delft. Last couple of months, I've exerted to make it a decent act. During this time I've felt like a genius and sometimes I felt like a complete retard, depending on my grip on the problem and the progress I made. By now, I know both is not true and I have reached the point where I can present a result that I am satisfied with.

I want to thank the members of my graduation committee. Myron, thank you for spending such a large amount of time on thinking, acting and programming along with me and for adding enthusiasm when mine was fading. Rinse, thank you for the numerous discussions and critical questions which helped me focusing on the the research as a whole, without getting lost in details. Bas, thank you for your thorough feedback and being a contact for me on hydrological issues. Gosse Jan, thank you for sharing your field experience on overtopping, both as input and as questions, and allowing me the freedom to shift the focus of my research to a more fundamental level as initially intended. Stefan, thank you for spending your scarce time on discussing and reviewing my thesis during meetings.

Furthermore, I want to thank everybody who helped me with explanation on the subject of my research (either from the scientific point of view or practical point of view), reviewing parts of my thesis, discussing what I was doing to get my thoughts straight, showing interest or any other type of support.

Above all I want to thank Chris, for all of the above and so much more: For providing much needed distraction, cheering me up when I was tired of my graduation work, patiently listening when I was orating about some specific, - in my opinion - brilliant detail of what I was doing, etcetera, etcetera.

Bart van Langevelde
Delft, August 2018

Abstract

A growing risk of flooding in coastal areas and the corresponding development of legislation drive continuous development in the field of hydraulic engineering. Failure due to wave overtopping is not fully understood from a physical point of view. Existing knowledge gaps, processes that are not yet explained by physics or not even discovered, are explained by empirical relations. The fact that knowledge on the relevant processes for overtopping load and soil resistance is fragmented and limited, causes limited application of it in practice.
To improve the understanding of failure caused by overtopping, a model that computes the soil stresses (soil stress is related to failure) in a dike cover, during overtopping load, is developed. It is possible that this model approach leads to additional knowledge on wave overtopping, e.g. new failure mechanisms or shift in normative mechanisms.

It is shown that overtopping has a large variety of appearances and so does failure due to overtopping. Literature study shows the large number of processes and characteristics, all with variable magnitude, that is relevant in the wave load and the soil strength during wave overtopping. Main wave load processes are shear stress (gradients), turbulence and impact. The considered soil strength process is the ratio between the stress (relative to the strength), for which the Young's Modulus, Poisson's ratio, soil weight, hydraulic conductivity and the subsoil stiffness are shown to be the main soil characteristics.

The developed model, a numerical 2D model with the model domain oriented parallel to the flow direction, computes the stress distribution and development in a loaded soil. For this case it is focused on dike land side slopes loaded by overtopping waves in particular, that is on dealing with clay, saturated conditions, fast varying load and a sloped surface. Stress equations in the model are derived, based on equilibrium of forces (horizontal and vertical) and motionless soil. The model is able to indicate initiation of failure for failure mechanisms that are associated with soil stresses, e.g. lifting of soil and head cut erosion. Soil in the model is loaded by normal and shear stress. The latter is, deviant from conventional methods, modelled as a shear stress gradient.

Test runs for verification and validation show that the model gives good results for cases with constant loads. Comparison of load cases with non-continuous overtopping wave loads shows both similarities and differences in the resulting soil stress. The most outstanding difference is the magnitude of the stress at depth. The differences indicate starting points for further research.
Model employment demonstrates the future possibilities. A single wave load, computed by the model itself, is modelled. This run gives, at first view, plausible results.

The current model gives a reasonable representation of soil stress development. Further development is recommended to make the model useful for dike assessment and design.

To do so, the model should be improved by probabilistic parameter definition, addition of soil stress damping and considering the impulsive nature and turbulent oscillations of wave load. Furthermore, it can be extended by the comparison between soil stress and strength, addition of spatial variability of the soil, enabling computations of non-planar parts of the slope and enabling the connection with other hydrodynamical models.

Contents

Preface **i**

Abstract **iii**

1 Introduction **1**
1.1 Background of the research . . . 1
1.1.1 Motivation of the research . . . 1
1.1.2 Overtopping . . . 2
1.1.3 Failure mechanism . . . 3
1.2 Problem description and research aim . . . 4
1.3 Research approach . . . 5
1.4 Report outline . . . 7

2 Literature **9**
2.1 Different types of failure . . . 9
2.1.1 Load components . . . 10
2.1.2 Soil resistance . . . 10
2.2 Development of overtopping wave characteristics . . . 12
2.2.1 Wave development at the crest . . . 12
2.2.2 Wave development at the land side slope . . . 13
2.2.3 Temporal distribution of a single wave . . . 14
2.3 Hydrodynamic load . . . 15
2.3.1 Dynamic pressure induced by turbulence . . . 15
2.3.2 Shear stress induced by flow . . . 17
2.3.3 Normal and shear stresses induced by wave impact . . . 18
2.4 Composition of a cover layer . . . 21
2.5 Geomechanical resistance . . . 21
2.5.1 Soil strength . . . 22
2.5.2 Compression . . . 24
2.5.3 Factors influencing strength . . . 27
2.6 Soil pressure measurements . . . 28
2.7 Literature conclusions . . . 29
2.7.1 Conclusions on knowledge . . . 29
2.7.2 Conclusions on modelling . . . 32

3 Methodology **33**
3.1 Balance equations describing pressure development . . . 34
3.1.1 Impulse balance . . . 35
3.1.2 Mass balance . . . 35

3.1.3 Derivation of model equations . . . 36
3.2 Initial conditions . . . 38
3.3 Surface boundary conditions . . . 39
3.3.1 Boundary conditions for different load situations . . . 40
3.3.2 Ratio soil stress components . . . 42
3.3.3 Theoretical approximation on stress development . . . 43
3.4 Side boundary conditions . . . 46
3.5 Bottom boundary conditions . . . 47
3.6 Discretization . . . 48
3.6.1 Discrete model dimensions . . . 48
3.6.2 Effective stress . . . 48
3.6.3 Water pressure . . . 49
3.6.4 Surface boundary condition . . . 50
3.7 Overtopping load computation . . . 50
3.8 Model assumptions . . . 52
3.8.1 Principles . . . 52
3.8.2 Parameter values . . . 53

4 Results **55**
4.1 Soil stress model . . . 55
4.1.1 Current model . . . 55
4.1.2 Approaches on modelling the surface boundary condition . . . 57
4.2 Qualitative verification . . . 58
4.2.1 Unloaded slope . . . 59
4.2.2 Slope loaded by homogeneous normal stress . . . 59
4.2.3 Slope loaded by homogeneous shear stress gradient . . . 62
4.2.4 Comparison with pressure measurements . . . 63
4.3 Model employment . . . 65
4.3.1 Computed single wave load . . . 67
4.3.2 Resulting soil stresses . . . 69

5 Discussion **71**
5.1 Current model . . . 71
5.1.1 Model structure . . . 72
5.1.2 Verification and validation . . . 74
5.2 Limitations and points of improvement . . . 74

6 Conclusions **77**
6.1 Objectives . . . 77
6.2 Research aim . . . 78

7 Recommendations **79**
7.1 Model improvement . . . 79
7.2 Model extension . . . 80
7.3 Future model employment . . . 81

List of Figures **83**

List of Tables **89**

Nomenclature **91**

References **98**

A Appendix: Pictures of overtopping simulations **111**
A.1 Afsluitdijk . . . 112
A.2 Boonweg . . . 113
A.3 Kattendijke . . . 115
A.4 Sint Philipsland . . . 115
A.5 Tholen . . . 116
A.6 Tielrode . . . 117
A.7 Vechtdijk . . . 118
A.8 Wijmeers II . . . 120

B Appendix: Geotechnical resisting mechanisms **121**
B.1 Soil crack strength . . . 121
B.2 Pulling force of grass . . . 122
B.3 Shear strength, apparent root cohesion . . . 124
B.4 Slip circle . . . 125
B.5 Turf element model . . . 126

C Appendix: Phases of dike breaching **129**

D Appendix: Pressure impulse by wave impact **133**
D.1 Derivation of pressure impulse forcing . . . 133
D.2 Effect of impact angle . . . 134
D.3 Demonstration case . . . 135

E Appendix: Comparison with modelling in COMSOL multiphysics **137**

1 Introduction

First the research topic is introduced. In Section 1.1, background information on the research topic is given. It contains a motivation of the research, an introduction in the concept of wave overtopping and an illustration of the complexity of overtopping. Thereafter a description of the actual problem and the accompanying scoping of the research with resulting research questions are given in Section 1.2. Section 1.3 shows the approach per research question. The chapter ends with an outline of the continuation of the report in Section 1.4.

1.1 Background of the research

1.1.1 Motivation of the research

The worldwide large and rising number of people live in low laying coastal areas (CIESIN et al. [2011]) is expected to rise over a billion in 2050 (Merkens et al. [2016]). By 2070 30 trillion euros of assets depend on flood protection, considering port cities only (Kok et al. [2013]). In coastal plains and river flood plains, the risk of flooding is large. Several hundreds of millions of people worldwide are exposed to the risk of flooding in case of a once in 100 years storm event (Hinkel et al. [2014]). Along rivers the risk of flooding rises due to increasing peak discharges (de Wit et al. [2008], van Vliet et al. [2013]). Consequently, flood protection is an important matter. Coastal areas are protected against flooding by man-made flood defences. A much applied type of flood defence is the dike.

The Netherlands has a leading position in the field of flood protection due to decades of experience with flood protection. The Dutch policy in the field of water safety is still developing, stimulated by developments of knowledge in the field of hydraulic engineering (TAW [1996a]). In the past the design of flood defences was based on occurring water levels and wave heights during storm conditions (TAW [1996b], Kuijken [2015]). The

probability of occurrence of such a normative storm (e.g. 1/10.000 year storm) was used to indicate the design class of the dike. Since 2017 new design criteria have been implemented (Vergouwe [2016], Schultz van Haegen [2016]), which are based on the risk of flooding of the dike instead of the probability of occurrence of a storm (Slootjes and van der Most [2016]). The risk of flooding depends on the probability of failure of the dike section.

A dike that is unable to fulfill its water retaining function is considered to be failed. In the Netherlands, different types of failure mechanisms are distinguished (van Baars and van Kempen [2009], TAW [1998]). The possibility of failure must be determined for each failure mechanism individually. One of the distinct causes of failure is failure due to wave overtopping. According to Kortenhaus [2003] it is one of the main causes of dike failure.

1.1.2 Overtopping

An overtopping wave induces load on the land side slope of a dike. An incident wave runs through several stages before it imposes load on the land side slope. Schüttrumpf and Oumeraci [2005] distinguishes five different stages, see Figure 1.1. Those are, in sequence from sea side to land side: incident waves, wave impact, wave run-up and run-down, wave overtopping at the crest and wave overtopping at the land side slope.

An incident wave gets steeper when it enters shallow water (*shoaling*) until it becomes unstable and collapses (*wave breaking*). Breaking waves impose an impact on the outer slope of the dike. A broken wave still contains forward momentum and runs up the outer slope of the dike. This is called *wave run-up*. Some running up waves loose their forward momentum before they reach the crest of the dike and they are pulled back by gravity force. This is called *wave run-down*. Waves that run up till the crest of the dike are the overtopping waves. If the water level exceeds the crest level of the dike, continuous overflow will occur.

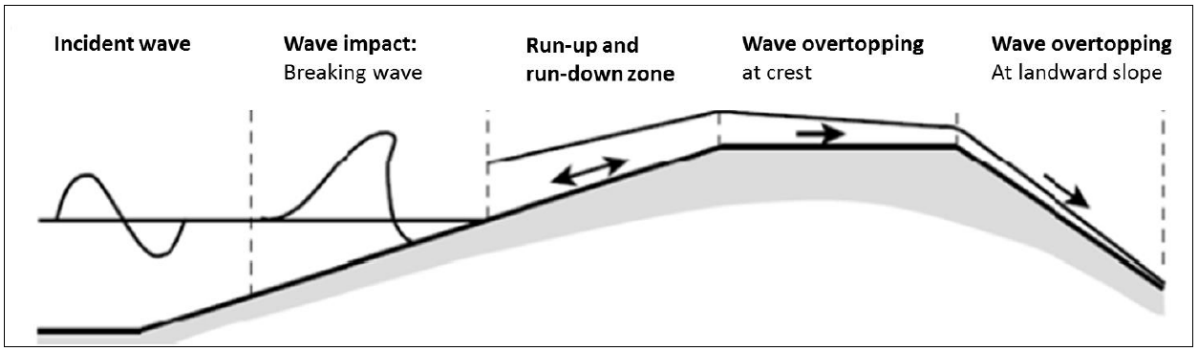

Figure 1.1: Distinction of stages an incident wave on a dike runs through Schüttrumpf and Oumeraci [2005])

Load induced by overtopping can cause initiation of failure of the slope on a small scale. The way failure develops partly depends on the geometry and structure of the dike. A frequent applied dike structure is a core of sand with a several decimeters cover layer

of clay which is overgrown with grass. Clay is more cohesive than sand, making it less vulnerable to erosion (Jain and Kothyari [2009]).

Development of failure runs through several phases, usually starting with cover failure (Visser [1998], d'Eliso [2007], van der Meer et al. [2007]). Local grass cover failure develops into large scale slope failure. The erosion resistance of bare clay is significantly lower than that of overgrown clay (Sprangers [1999]). The resistance of sand is even lower, causing, after cover penetrating damage, the damage to grow exponentially (Wan and Fell [2004]). A dike is assumed to loose its water retaining function, once damage of the cover ensues. Failure of the cover layer leads to a fast and almost certain dike failure. Dike failure is exceedence of the ultimate limit state (ULS) of the dike. It can therefore be considered to be dike failure itself.

1.1.3 Failure mechanism

Failure caused by overtopping is a complex problem for which multiple failure mechanisms are observed (Valk [2009], Trung and Verhagen [2014]). This is observed during tests, see Appendix A. Multiple observed failure locations are shown in Figure 1.2. This indicates multiple relevant physical processes. The extend to which different processes influence overtopping is an ongoing research (TAW [2001], de Visser [2017], Rijkswaterstaat [2017]). In general, soil is expected to fail when the soil stress exceeds the strength.

A distinction is made between hydrodynamic processes and geotechnical processes. Hydrodynamic processes impose the load on the slope cover. Geotechnical processes give the cover its strength. Relevant hydrodynamic processes are shear stress imposed by flowing water, normal stress imposed by turbulence and normal and shear stress imposed by wave impact. Geotechnical processes depend on multiple parameters like cohesion of soil, strength of grass, elasticity of soil, elasticity of grass and angle of repose of soil. Furthermore, geometrical aspects like the slope angle, objects on the slope and the roughness of grass cover are relevant.

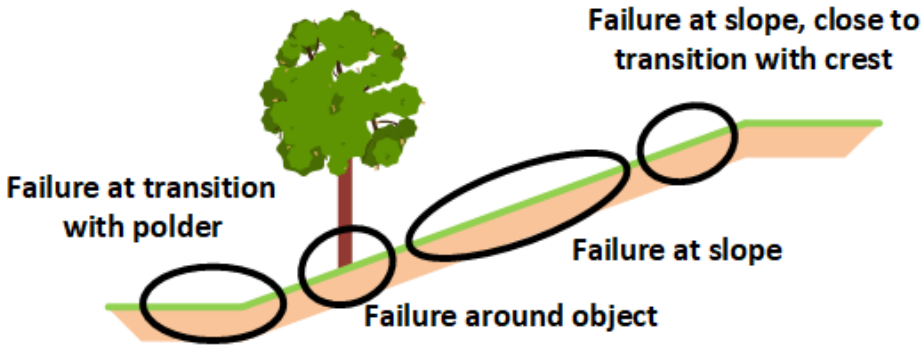

Figure 1.2: Locations of failure that are observed frequently during tests.

Due to this complexity a number of theories and methods have been developed to describe the failure process of overtopping. None of these failure mechanisms (hence accompanying theories) is all-embracing and none of them excludes all others. This indicates that multiple mechanisms can occur simultaneously. Dike assessments based on testing only one loading mechanism, like Bles et al. [2015], is therefore physically incorrect.

Some methods are supported mainly empirically (e.g. Emmerling [1973], d'Eliso [2007]). Empirical relations contain more uncertainty than physical relations. Furthermore, an empirical approach is a *black box* approach requiring *fit factors* to make the explanatory equations match the test results. The physical meaning of these factors is often not or barely known, as is their possible variation for changing conditions. The results of empirical research are not or very limited applicable on cases deviant from the test case.

Multiple methods have been developed to estimate the hydraulic load on the slope, relating the damage to a stress. Examples are the *Cumulative Overload Method* (Dean et al. [2010], van der Meer et al. [2010a]), the *dynamic pressure* (Hoffmans [2012]) and the direct shear stress methods (e.g. d'Eliso [2007]). A variation is the excess load approach based on work generated by the wave (Dean et al. [2010]). Recent observations show that an overtopping wave separates from the dike surface at the transition from crest to dike (van Damme et al. [2016]). This indicates that a dike cover can be loaded by wave impact. A more extended explanation on the models describing particular loading mechanisms is given is Section 2.3.

Multiple methods have been developed that aim to predict the strength of soil and the additional strength of grass. Examples are the *apparent root cohesion* (Wu et al. [1979]), the extended model for the strength of cracks (Führböter [1966], Richwien [2003]) and the *Turf Element Model* (Hoffmans [2012]). Variation of the cover strength in time is caused by fatigue and infiltration (Bijlard [2015], O´Kelly [2013]). Due to the complexity of a turf layer consisting of soil and grass, uncertainty exists on the strength of it. Grass is an anisotropic material, which further complicates the development of physical knowledge on its behaviour. A more extended explanation on the strength of the soil is given in Section 2.5 and on models describing particular failure mechanisms in Appendix B.

Spatial variation plays an important role. Wave load depends on the on the flow depth and velocity, which varies along the slope. The stresses due to wave impact act wider than the impact area (Tu and Wood [1996]). Soil, especially if grass covered, is very inhomogeneous, causing a spatial variable strength. Some geometrical aspects (mentioned previous) have a local influence on the strength.

1.2 Problem description and research aim

Current knowledge on the failure of a dike cover due to overtopping load is limited and fragmented. Methods that have been developed to describe and predict failure assume that one failure mechanism is normative for all cases. For instance the Cumulative Overload Method (Dean et al. [2010], van der Meer et al. [2010a]), currently used for evaluating dikes, is based on the assumption that failure is related to shear stress. However, it is observed that wave impact can occur (van Damme et al. [2016]). Furthermore it is noticed that for equal mean excess load the grass cover fails for certain overtopping velocities but is able to resist higher overflow velocities (van Damme et al. [2017]). This suggests that the pulsating nature of the overtopping load accelerates failure.

Knowledge on the effect of a wave load on the soil is lacking. Also a simple method to determine the soil reaction under a highly variable wave load is missing. Models to

compute soil stress exist but these are not able to deal with a variable combination of normal and shear stress load well, or are complex requiring a lot of input knowledge and computation time. No model exists that is able to compute both hydrodynamical load and geotechnical response.

The purpose of this study is to improve the knowledge on the processes leading to failure of a dike cover. It is focused on failure mechanisms caused by changes in soil stress. With improved knowledge on relevant processes in dike failure, better criteria for assessment and design can be drafted. Improvement of criteria can be in different ways, e.g. reducing uncertainties or shifting normative mechanism. This increases the certainty of the safety of existing dikes. Improved knowledge contributes to the improvement of the design and assessment of dikes.

The purpose of this research is summarized in the following main aim:

> *Improve the understanding of initiation geotechnical failure of a dike cover during overtopping wave load.*

Geotechnical failure is related to strain which is related to stresses and the gradients of stresses in the soil (Atkinson [2000]). Insight in the distribution and development of soil stresses during wave load, improves the understanding of geotechnical failure. Accurate modelling of the soil stresses can provide this insight. To achieve this, the following objectives have been set:

1. *Develop a model to compute the development of soil stresses for an imposed hydrodynamical overtopping load.*
2. *Validate the soil stress representation of the model.*
3. *Employ the model to predict geotechnical failure.*

1.3 Research approach

This section gives the approach to the research objectives and how they relate to the main aim of this study. The approach to the objectives is the following:

1. *Develop a model to compute the development of soil stresses for an imposed hydrodynamical overtopping load.*
   A literature study is preformed to evaluate possible types of load on the slope. It is investigated what processes are present in an overtopping wave. With this knowledge a case of an overtopping wave load distribution, developing in time, is determined. By literature study it is further investigated what soil characteristics influence the soil stress development, in what way.
   A 2D numerical model is developed to computed the stress development in the dike cover. A setup for this model is shown in Figure 1.3. Using the results of the literature study, this model computes the distribution and development of soil stresses, considering a given hydrodynamic load.
   This approach aims to give an accurate physical representation of the soil stress distribution and development in a loaded soil.

2. *Validate the soil stress representation of the model.*
   Several model runs are executed for comparison of their results. The results of runs with simple load cases are compared to the expected results based on physics, for qualitative verification of the model. Further, some overtopping waves, observed during measurements, are simulated in a model run. The soil stress results from the model are compared to those resulting from the measurements, for validation of the model.
   This approach aims to indicate the accuracy of the soil stress computation of the current model. Furthermore it indicates defects in the model outcome which form opportunities for improvement during further development.

3. *Employ the model to predict geotechnical failure.*
   Using the results of the literature study, the model computes overtopping wave loads. Considering an overtopping wave load, the soil stress distribution and development is computed.
   This approach aims to indicate the spots in the soil with soil stresses that are likely to cause failure. It furthermore shows the capabilities of the model.

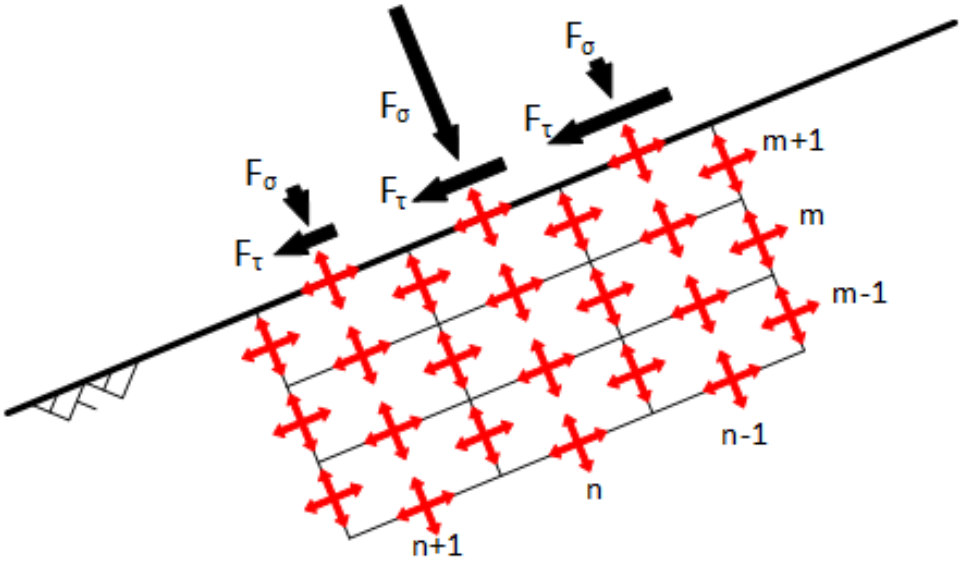

Figure 1.3: Sketch of the setup of a numerical model with soil divided in grid cells, spatial variable loading forces (black arrows) and possible reaction forces (red arrows).

The approaches to objectives 1 and 2 are carried out iteratively. Model tests lead to new development and model development requires additional testing. Intermediate results of iterative steps are not presented. The approach to objective 3 is carried out with the developed model, resulting from the iteration.

The numerical model is drafted from scratch in Matlab to be able to modify all parts of the model if wanted. It enables to use a stress computation method of choice. It furthermore enables to simplify model stress calculations where possible, which favours the computation time. Finally, it is possible to make a single model computing both the hydrodynamical physics and the geotechnical physics of an overtopping event. Use of

existing modelling software is considered but rejected because of drawbacks or impossibilities on these points.

Overtopping is a complex process. Within the available time frame of this study it is impossible to consider the entire process in detail. This study focuses on determining the geotechnical stresses caused by particular hydrodynamic loads. The load is put in as a boundary condition. The loss of accuracy in the description of the load that is associated with this method is expected to be acceptable. In this early stage of model development it is sufficient to know the order of magnitude of the load and to analyze its effect.
Furthermore, not the entire dike geometry is considered. The model only considers one part of the dike: the landward slope with a flat, sloped surface, see Figure 1.2. The cover layer is considered to be a bare clay layer. This survey is on local action of forces on the dike cover, so transition points of the slope angle and objects on the slope are not considered.

1.4 Report outline

In Chapter 2 an overview is given of the current relevant knowledge on wave overtopping. This contains both hydrodynamical and geotechnical processes and both a theoretical and a practical approach. In Chapter 3 the structure of the numerical model is given. First the model general equations representing physical processes in the soil and the equations that define the initial and boundary conditions are derived, followed by descretization steps to make them suitable for a numerical model. Further, the modelling of overtopping wave load is explained. Finally, an overview of used assumptions in model derivation is given. Subsequently, in Chapter 4, a brief recap of the resulting model is given, followed by results of model runs for qualitative verification and to demonstrate the model use for overtopping wave computations. Based on the results, the accomplishment of the research aim and objectives, set in Section 1.2, is discussed in Chapter 5. From the discussion conclusions are drawn in Chapter 6. Finally, in Chapter 7, recommendations are given for the future of the model. This is split up in recommendations for the improvement to a model that is able to give a correct representation of soil reaction for given load, recommendations for the extension to a widely applicable and useful model and recommendations on model employment that can be used as a goal in further model development.
In the appendices information is given that serves as support, frame or background for this research. It contains pictures showing different types of failure during overtopping simulations (Appendix A), different soil resistance processes which are acknowledged (Appendix B), information on the dike breaching process (Appendix C), a theory on impulsive wave load (Appendix D) and a soil stress computation using existing software (Appendix E).

2 Literature

A lot research is done on different phases and components of overtopping failure, leading to the existence of different theories and models. First of all Section 2.1 shows the diversity in appearances of dike breaching. Then, knowledge on hydrodynamic load is presented: Development of wave characteristics in different phases of overtopping is presented in Section 2.2 and theories on processes imposing the load are given in Section 2.3. Subsequently knowledge on geotechnical resistance is presented: Section 2.4 elaborates on the elements and composition of a dike cover and Section 2.5 discusses the strength properties of the cover layer components (soil and grass). Measurements of the soil stress development under overtopping load are shown in Section 2.6. Finally, a recap of the knowledge in this chapter is given and the contribution it is presented in Sections 2.7 and **??**.

2.1 Different types of failure

Failure depends on load on the soil and resistance of the soil. Both appear in multiple ways. This is further explained in Sections 2.1.1 and 2.1.2 for load and resistance respectively. This research focuses on the resistance of the soil. With the explanation of the soil resistance in Section 2.1.2, a further focusing of the research is given

Different combinations of types of loads and resistance lead to a large number of different types and locations of cover failure. This is shown by observations, given in Appendix A. This emphasizes the complexity of wave overtopping.

Failure of a dike initiates with the failure of the dike cover. More on the distinct phases of failure is given in Appendix C. The remainder of this report focuses on the failure of the cover layer.

2.1.1 Load components

An overtopping wave can be schematized as an incoming jet passing the crest and interacts with the slope. For a large impact angle this leads to interaction dominated by jet impact. Albertson et al. [1950] explains the complexity of such a load and the existence multiple regions with different dynamics. For a small impact angle the forcing is dominated by shear.
Loading forces that are considered are the dynamic pressure forces imposed by turbulence (e.g. Emmerling [1973]), the normal and shear impact forces imposed by wave impact (e.g. Ponsioen et al. [2017]) and the shear stress imposed by flowing water over a surface with certain roughness (e.g. d'Eliso [2007]).

2.1.2 Soil resistance

On the strength of soil multiple approaches exist. This arises from the number of ways in which soil can be loaded and the complexity of soil as a material. Failure on macro scale is distinguished from failure on smaller scale. Failure on macro scale in case of overtopping is the occurrence of sliding of a large part of the slope along a slip circle. An widely acknowledged and used method to determine the resistance against macro scale failure is the method of Bishop [1955].
During recent overtopping simulations, small scale failure is observed more frequently than macro scale failure (Appendix A). d'Eliso [2007] states that the location and way of failure is determined by the appearance of local weak spots. The non-uniform composition of soil and grass in a dike cover gives rise to multiple approaches on the strength of it. Soil strength is approached by the determination of the strength of uniform clean soil. This is extended by adding grass characteristics in the determination of the pulling strength (Trung and Verhagen [2014]) and the shear strength (Wu et al. [1979]).
The presence of cracks (weak spots) at the soils surface is a local weak spot, causes a different failure mechanism to appear (Führböter [1966]). Increase of water pressure in the cracks can push the walls of the crack away. This can lead to local soil removal.
An extended explanation on the different approaches to determine soil strength is given in Appendix B.

Different types of failure are observed. Trung and Verhagen [2014] distinguish three damage types at the cover: *head-cut*, *roll-up* and *collapse*. These are shown in Figures 2.1a, 2.1b and 2.1c respectively. Head-cut damage is the simultaneous removal of the turf and the clay layer, hence lifting of the soil. It is explained by the occurrence of a local weak spot at depth. Whether or not this type of damage occurs, largely depends on the soil composition. Roll-up damage is shear stress induced and occurs when a drag force acts on the cover over a certain height. The flow than lifts the turf and pushes it over, slowly down along the slope. This requires protrusion of the cover or presence of a significant crack or hole in the cover. The type of grass cover influences whether or not roll-up damage occurs. Collapse type of damage is observed at dikes consisting of predominantly non-cohesive sandy material. Once initial damage reaches the sandy core, the sand erodes at a large speed and the cover looses its support, increasing the erosion rate.
Another type of failure is the sliding off of large parts of a grass cover (Valk [2009],

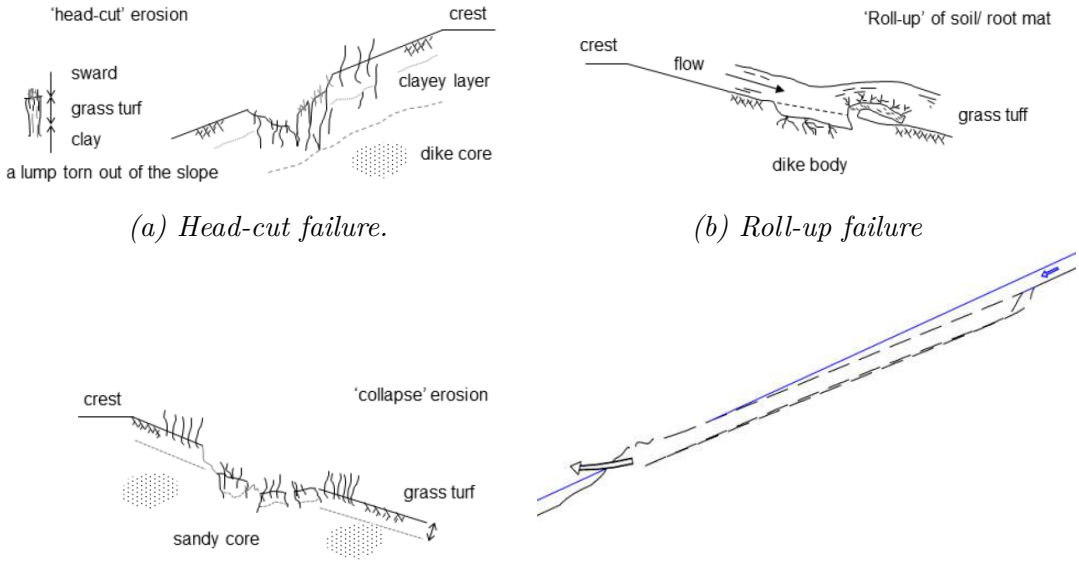

(a) Head-cut failure.

(b) Roll-up failure

(c) Collapse failure

(d) Shallow sliding failure.

Figure 2.1: Principle sketches of some distinguished types of failure due to overtopping (Valk [2009], Trung and Verhagen [2014]).

't Hart et al. [2016]), see Figure 2.1d. Infiltration can cause sliding of the slope to occur for a thin layer with approximately the thickness of the grass layer. This is a macro scale failure.
Furthermore, the Turf Element Model (Hoffmans et al. [2008]) acknowledges and explains failure of a cover by lifting of the soil. Based on vertical equilibrium of forces it gives a measure for the stability of a soil element. Note that the approach of equilibrium of forces can be used to determine throughout the soil in three perpendicular directions, to indicate (even subsurface) locations of soil failure.

Occurrence of failure is related to soil stress (Atkinson [2000]). The focus of this research is on the failure as a direct result of occurring soil stress and present soil strength. This does not include the development of damage after initial damage. Failure is expected when soil stress (gradient force) exceeds soil strength. In practice, three combinations of stress and strength are expected to appear:

- High soil stress overlaying a local weak spot. In this case the soil stress can exceed the soil strength, causing local collapse of the soil structure;
- Effective soil stress becoming negative, since soil has no tensile strength. This can be caused by pulling load at the surface or by pore water pressure increase without total stress increase. In this case the soil looses its coherence;
- Stress gradient force exceeding the soil strength. This can be caused either by very large stress differences or stress differences over a very short differences.

For prediction of macro scale failure a comprehensive and detailed knowledge on soil strength in the entire dike is required, which is unrealistic to obtain. The research focuses on initial, small scale failure. That is failure alike soil lifting and head-cut damage. Further, the understanding of failure due to overtopping is limited. If there are

blind spots in the knowledge on geotechnical failure due to soil stresses, the model can be able to reveal these spots.

2.2 Development of overtopping wave characteristics

This section gives approaches for characteristics of overtopping waves. These characteristics are used to determine overtopping loads. Considered characteristics are flow depth, flow velocity and temporal variation during one wave cycle.

2.2.1 Wave development at the crest

The wave thickness at the crest is depending on the thickness of the incoming wave running up the dike (Schüttrumpf and van Gent [2003]). The development of wave thickness over the crest provided with definitions of parameters is given in Figure 2.2. At the seaward edge of the crest the wave thickness decreases to a third of the incoming wave thickness, due to the change in flow direction (van der Meer et al. [2012]). After this decrease the wave thickness remains constant for a smooth crest. The incoming wave thickness at the crest ($h_{c,2\%}$) is related to the wave thickness that is exceeded by 2% of the waves, see Equation 2.1. $R_{2\%}$ is the run-up level exceeded by 2% of the waves, R_c is the crest freeboard and $c_{h,2\%}$ is a wave overtopping coefficient.

$$h_{c,2\%}(x_c = 0) = \frac{1}{3} c_{h,2\%}(R_{2\%} - R_c) \tag{2.1}$$

Applicable values for $c_{h,2\%}$ are 0.20 for slopes of 1:3 to 1:4 and 0.30 for slopes of 1:6. Coefficients for slopes with a value between these values are found by interpolation. The value of $R_{u2\%}$ is given by Equation 2.2. Here γ_b, γ_f and γ_β are influence factors for berms, slope roughness and oblique wave attack respectively, $\xi_{m-1,0}$ is the breaker parameter and H_{m0} is the incoming significant wave height.

$$\frac{R_{2\%}}{H_{m0}} = 1.65 \gamma_b \gamma_f \gamma_\beta \xi_{m-1,0} \tag{2.2}$$

The flow velocity of a wave overtopping the crest depends on the flow velocity of the wave reaching the crest and the width of the crest (van der Meer et al. [2016]). The development of wave thickness over the crest provided with definitions of parameters is given in Figure 2.2. The flow velocity of the wave decreases while passing the dike crest. The relation between the flow velocity at both edges of the crest is given by Equation 2.3. Here, x_c is the location at the crest and $T_{m-1,0}$ is the incoming significant wave period.
The incoming wave velocity (at $x_c = 0$) is approached by Equation 2.4. This equation gives the flow velocity for the 2% run-up waves. Applicable values for overtopping coefficient $c_{v,2\%}$ are 1.4-1.5 for slope angles from 1:3 to 1:6.

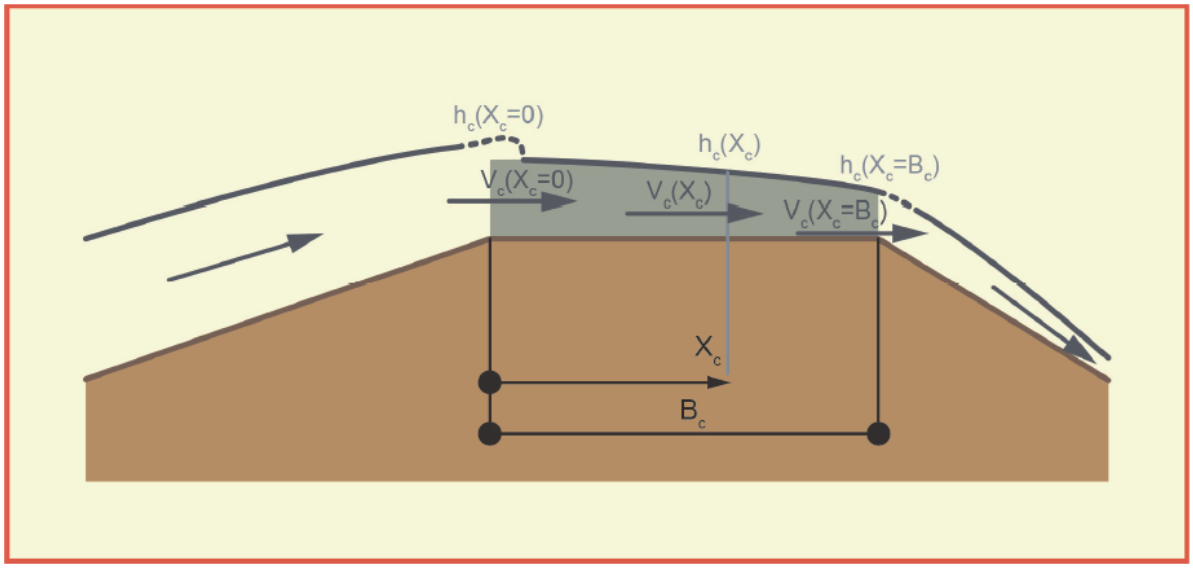

Figure 2.2: Development of flow overtopping parameters on the crest of a dike van der Meer et al. [2016])

$$v_{c,2\%}(x_c) = v_{c,2\%}(x_c = 0)\exp(\frac{-1.4x_c}{(\frac{gT_{m-1,0}^2}{2\pi})}) \tag{2.3}$$

$$v_{c,2\%}(x_c = 0) = c_{v,2\%}\sqrt{g(R_{2\%} - R_c)} \tag{2.4}$$

2.2.2 Wave development at the land side slope

The flow velocity and thickness at the land side slope (both relevant for load definition) depends on the wave that passes the crest, the slope angle and the location on the slope (Schüttrumpf and van Gent [2003], van der Meer et al. [2016]). Assuming negligible velocities normal to the slope, a constant pressure over the crest and negligible viscous effects in the direction parallel to the slope, a relation between flow velocity (v_b) and flow thickness (h_b) is given by Equation 2.5. The subscript 0 indicates the start of the slope (transition with crest). The parameters t and k_l are given by Equations 2.6 and 2.7 respectively. In these equations, s_b is the distance along the slope from the crest and θ is the slope angle.
In these equations the only unknowns are the flow velocity and the flow thickness. Using the mass balance based on the specific discharge (Equation 2.8), the flow velocity and thickness can be found iteratively.

$$v_b = \frac{v_{b,0} + \frac{h_b k_l}{0.01}\tanh\left(\frac{k_l t}{2}\right)}{1 + \frac{0.01 v_{b,0}}{h_b k_l}\tanh\left(\frac{k_l t}{2}\right)} \tag{2.5}$$

$$t = -\frac{v_{b,0}}{g\sin\theta} + \sqrt{\frac{v_b^2}{g^2\sin\theta^2} + \frac{2s_b}{g\sin\theta}} \tag{2.6}$$

$$k_l = \sqrt{\frac{0.02g \sin\theta}{h_b}} \tag{2.7}$$

$$h_b = \frac{v_{b,0} h_{b,0}}{v_b} \tag{2.8}$$

2.2.3 Temporal distribution of a single wave

The instantaneous wave load on the slope is considered. Besides the maximum wave load, the gradients in wave load are of interest for the wave forcing on the slope. The development of flow thickness and velocity during a wave cycle is given by analytical power-curve forms (Hughes [2011], Hughes et al. [2012]), given by Equations 2.9 and 2.10 respectively. This development is supported by measurements(van der Meer et al. [2010a]). From these relations follows a similar development relation can be drawn for the development of the discharge, see Equation 2.11.
Assuming negligible wave deformation in space, these equations are useful to describe the distribution of a wave in time and space. The local wave front flow velocity (u_{max}) gives the velocity with which the wave front moves over the slope. The local maximum values must be used as maximum values in the equations, to include the temporal change in wave front characteristics in the description.
In these equations t is the point in time in a wave and T_0 is the total duration of an individual wave. The exponents a and b express the extend to which the development of the flow thickness and the flow velocity respectively, follows the power curve. Since the specific discharge (q) is the product of the flow thickness and the flow velocity, the exponent that describes the development of the specific discharge equals $a+b$. According to Hughes [2011] it is a reasonable to assume a linear decrease of the flow depth and velocity, resulting in a value for a and b of 1. With linearization the tail of the wave is neglected. However, the tail of the wave is of lesser relevance for the overtopping load and accompanying damage. According to van der Meer et al. [2010b] neglecting the tail improves the approach of the relevant overtopping wave.

$$h(t) = h_{max}(1 - \frac{t}{T_0})^a \tag{2.9}$$

$$u(t) = u_{max}(1 - \frac{t}{T_0})^b \tag{2.10}$$

$$q(t) = q_{max}(1 - \frac{t}{T_0})^{a+b} \tag{2.11}$$

Gradients in water depth and flow velocity are linked to gradients in stresses, thus to stress gradient forces (see Section 2.3.2). At the wave front the water depth and flow velocity gradient are large, so the stress gradient forces are expected to be large as well. So far the wave front is assumed to have an infinite steepness. Measurements by van der Meer et al. [2010a] show wave developments in time at fixed locations. The results show

that the wave front steepness ranges from 0.3 m/s till 0.5 m/s. Accordingly the steepness of the wave velocity ranges from approximately 5 m/s/s till 45 m/s/s.

2.3 Hydrodynamic load

This section contemplates different types of load that are distinguished. First a dynamic pressure force, normal to the slope, caused by turbulence in the flow, is discussed in Section 2.3.1. Furthermore, shear force imposed by the flow over a slope with a certain roughness is distinguished. This is discussed in Section 2.3.2. Finally, normal and shear stress caused by wave impact from overtopping waves that have separated from the surface. This is discussed in Section 2.3.3.

2.3.1 Dynamic pressure induced by turbulence

A forcing mechanism, observed at the onset of slope dislocation, is the dynamic pressure force (described by Hoffmans [2012]). It has been subject of many studies and its development is advanced. The dynamic pressure force acts normal to the surface. The force originates from variability of surface pressure due to turbulent motions in the water. The pressure variability in time is shown in surface pressure measurements (Verheij et al. [2015]).
Eddy motions in a turbulent flow generate an instantaneous variable pressure field. Downward eddy motion imposes larger pressure than upward motion. The latter even can impose negative pressure. This causes an *instantaneous variable force* on the soil. At one instant, the surface water pressure on the grass varies in space. Negative pressure peaks are linked to a suction force (Kerman-Nejad et al. [2011]). This variability of the pressure field at one instant is called the *instantaneous pressure variability*. The concept of instantaneous pressure variability is shown in Figure 2.3.
Besides instantaneous pressure variability, which is variability in space, there is the *local pressure variability*, a variability in time at one location. This means that turbulent flow load also range from positive to negative on one location.
Note that the dynamic pressure describes the variation of pressure ($\approx$ twice the pressure signal amplitude). The dynamic pressure can be directed upward and downward. The upward pressure is considered to be normative for failure by Hoffmans [2012].

Dynamic pressure is induced by flow turbulence. Turbulence can be described by the depth averaged relative turbulence intensity (r_0). This is a function of the (longitudinal) turbulence intensity (σ_u) and the depth averaged flow velocity of the mean flow (U_0), see Equation 2.12 (Schiereck and Verhagen [2016]). The longitudinal relative turbulence intensity is the standard deviation of the streamwise velocity.

$$r_0 = \frac{\sigma_u}{U_0} \tag{2.12}$$

The turbulence intensity is a inconvenient parameter to work with. A simplification by Graf [1998] replaces σ_u by a turbulence coefficient (α_0) and the shear stress velocity

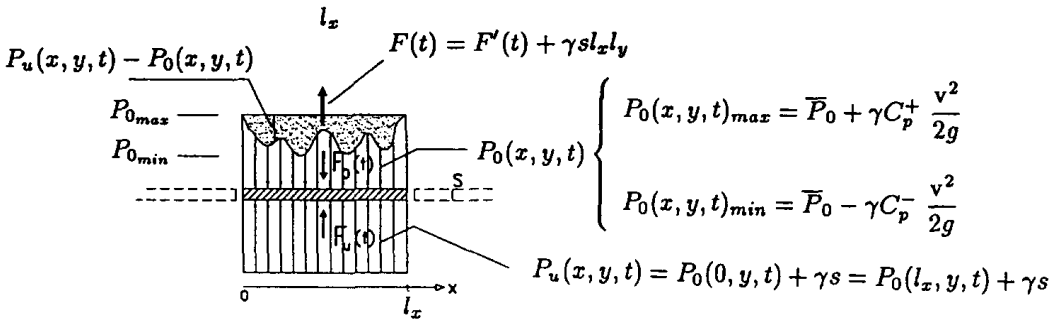

Figure 2.3: Conceptual scheme of instantaneous normal forcing on the soil surface generated by unbalanced pressure distributions (Bellin and Fiorotto [1995])

(u_*), see Equation 2.13. Subsequently by involving the Chezy value (C) it is given in an alternative way.

$$r_0 = \alpha_0 \frac{u_*}{U_0} = \alpha_0 \frac{\sqrt{g}}{C} \tag{2.13}$$

Based on tests, Emmerling [1973] found a relation expressing the maximum pressure fluctuation (the dynamic pressure) p_m in terms of the mean bed shear stress τ_0. This relation is given in Equation 2.14. In this relation, the turbulence coefficient $\alpha_\tau \approx 18$. Application of Equation 2.14 results in pressure fluctuations up to 10 kN/m^2 for wave overtopping cases.

$$p_m = \alpha_\tau \tau_0 \tag{2.14}$$

Equations 2.14 is rather incomplete considering physical parameters that influence the pressure. Measurements had shown that p_m is depth dependant, with a maximum where the flow depth is maximum (Hoffmans [2012]). Furthermore air concentration is considerable in a highly turbulent flow. Measurements also led to a correction factor for air concentration (η_a) in the flow. Applying these improvements leads to Equation 2.15 which gives the normative load by the dynamic pressure. The slope of the bed is represented by S_{bed}.

$$p_m = \alpha_\tau \rho g h_{max} (1 - \eta_a) S_{bed} \tag{2.15}$$

The symbol h_{max} represents the maximum flow thickness on the bed. On the slope an accelerating flow can be expected. Mass continuity requires that an accelerating flow gets shallower. The largest flow thickness is expected where the flow velocity is smallest, that is at the upper end of the slope. Consequently, the largest dynamic pressure force is expected at the upper end of the slope.

2.3.2 Shear stress induced by flow

A second load mechanism is the shear stress caused by the flow over the soil. The roughness of the surface and protruding elements cause friction between the flow and the surface. The flow imposes a force on the soil. Note that shear stress is not induced by turbulence, it is the other way around: shear stress causes a velocity gradient which is a continuous source of energy for the turbulence (Jimènez [1999]).

A widely used method to describe flow characteristics in relation to the bottom roughness, is the Manning formula (Manning [1891]). It gives the relation between the averaged flow velocity, the bottom roughness and the slope. For convenience the Manning formula is given in an alternative form in Equation 2.16), which directly gives the shear stress (van Damme [2016]). An approximation of the roughness of a grassed surface is a Manning coefficient of approximately 0.03 $s/m^{1/3}$ (Chow [1959], Chanson [2004], Abood et al. [2006]).

$$\tau = \frac{\rho g U_0^2 n^2}{h^{\frac{1}{3}}} \tag{2.16}$$

Gradients in shear stress, parallel to the wall or surface, are a load as well (Gijsen et al. [1997], Cherubini et al. [2015]). This is shown in Figure 2.4. These stress gradients can be large for variable loads, in particular for an overtopping wave front or turbulent load oscillations. This applies on variable loads in particular and can be an explanation for observed differences between overtopping and overflow (van Damme et al. [2017]).

Figure 2.4: Principle sketch of shear stress gradient load, with in red the shear stress and in blue the shear stress gradient force.

Excess overload method

Dean et al. [2010] approaches the normative load as a load that excesses a certain threshold. This load can be expressed in terms of velocity (U), shear stress (U^2) and work (U^3). The threshold value is expressed as a function of the critical flow velocity (U_c). Damage is expected when a load exceeds the threshold value (van der Meer et al. [2010a]).

The shear stress based approximation that is currently applied in The Netherlands, is the *Cumulative Overload Method*. It is given by Equation 2.17. The first term represents the load on the grass and the second term represents the strength. Note that this equation is is only valid if $\alpha_M U^2 > \alpha_s U_c^2$.
In this equation is D the damage factor and α_M a load factor for an increase in the velocity of the overtopping wave (U). Furthermore, α_s is a strength factor for a decrease in the strength of a grass sod, where the strength of the grass sod is expressed as critical velocity (U_c). The relation between this U_c and the actual strength of the soil is unclear. According to Steendam et al. [2014] the factor α_M can be related to the shear stress.

Apart from this relation and the proportionality to u^2, the relation between this method and the actual load is unclear. Both the load and strength definitions are no physical explanation for (the time dependency) failure.

$$D = \sum (\alpha_M U^2 - \alpha_s U_c^2) \tag{2.17}$$

2.3.3 Normal and shear stresses induced by wave impact

A third forcing mechanism is the impact of a plunging overtopping wave. An impacting wave can impose a large and very local load on the slope. In recent research van Damme et al. [2016] observed that overtopping waves separate from the surface at the transition of the dike crest to the land side slope (for a steep slope of 1:1.7), see Figure 2.5. This observation is supported by previous research on flow separation (Keutner [1934], Moss [1972], Ramamurthy and Vo [1993]). The wave motion is schematized as a ballistic projectile motion of a solid mass, starting with a horizontal motion on the dike crest. The physical explanation is done likewise. The forcing mechanism is shown in Figure 2.6.
In Figure 2.6 the x, z reference frame is oriented to the crest; axes are in horizontal and vertical direction. Hence, u_x equals u_{crest}. Figure 2.6 shows an additional χ, ζ reference frame that is oriented on the slope. This reference frame is rotated with slope angle θ with respect to the first reference frame. The distinction in frames of reference is made to be able to make a clear distinction between forces that are directed normal and parallel to the soil surface, both on the crest of the dike and on the slope. In the remainder of this report the distinct indications for the frames of reference are used only when both are relevant. Otherwise x and z are used instead of χ and ζ to indicate the reference frame oriented to the slope.

The wave impact force acts on the slope under and angle, which is decomposed into components normal and parallel to the slope. Ponsioen [2016] assumes that both forces are entirely transmitted to the grass. For the normal forcing this is a valid assumption. For shear forcing this is not, since a part of the momentum of the water moves down the slope. The equation giving shear force must contain a friction factor (c_f) to account for the portion of the shear momentum that is transmitted as a shear force on the surface. For this the shear stress equation with the Manning coefficient is used (Equation 2.16). In this equation ρU_0^2 represents the pressure potential in the wave. The remainder represents the portion of this pressure potential acting as a shear stress on the surface. This remainder is Manning's coefficient, rewritten to a friction factor by inclusion of the gravitational constant and the flow depth (Equation 2.18).

$$c_f = \frac{gn^2}{h^{\frac{1}{3}}} \tag{2.18}$$

For the decomposition of the incoming wave the velocity is decomposed in a component normal and parallel to the slope. This is given by Equations 2.19 and 2.20 respectively. The absolute velocity of the wave is given by $|u|$ and the impact angle is given by β.

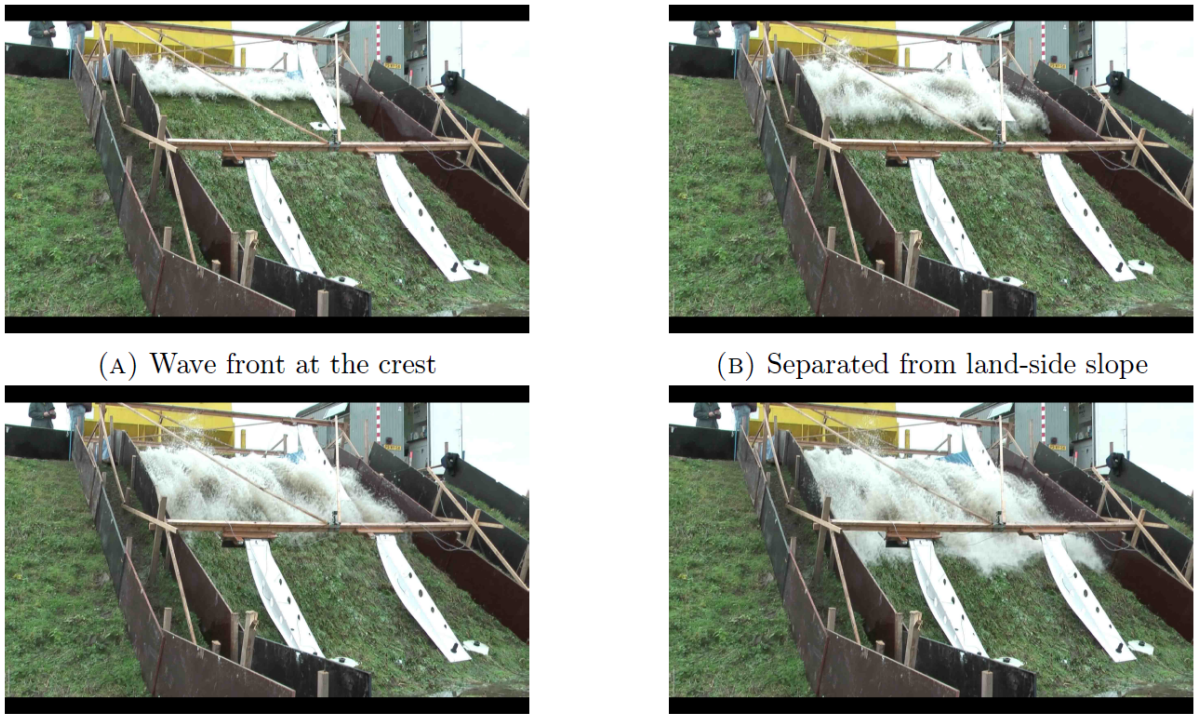

(A) Wave front at the crest

(B) Separated from land-side slope

(C) Still separated

(D) Moment of impact

Figure 2.5: Separation of an overtopping 1000 l wave before impacting on the land-side slope. (Ponsioen [2016])

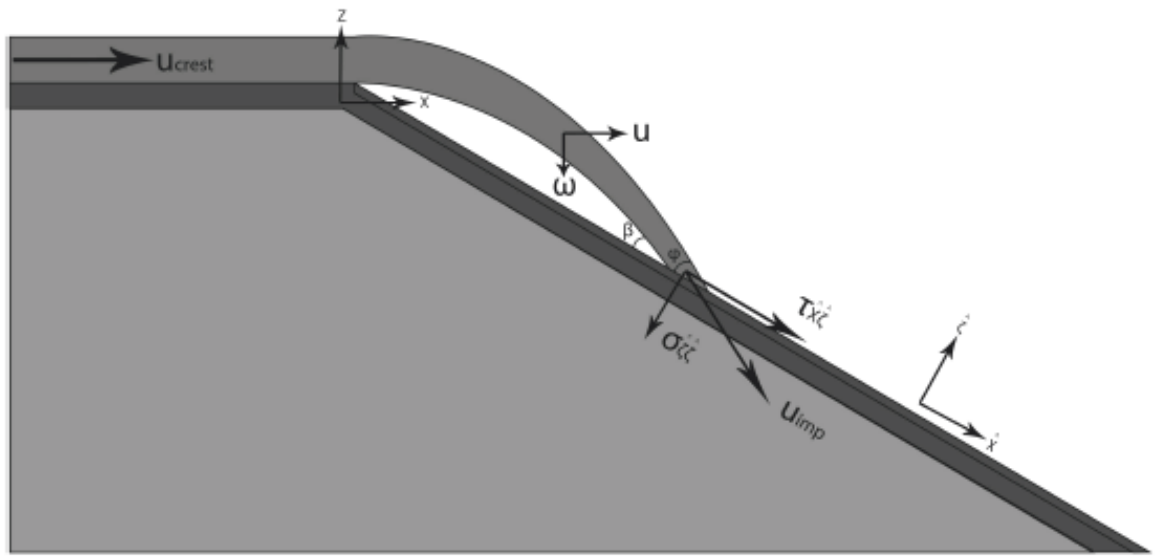

Figure 2.6: Approach for forcing on the slope by an impacting wave, per unit width (Ponsioen et al. [2017])

The decomposed velocities give expressions for the decomposed forces. This is shown in Equations 2.21 and 2.22 for the normal and shear stress respectively.

$$\vec{u_\zeta} = |u| \sin \beta \tag{2.19}$$

$$\vec{u_\chi} = |u|\cos\beta \tag{2.20}$$

$$\sigma_{\zeta\zeta} = \rho|u|\vec{u_\zeta} = \rho u^2 \sin\beta \tag{2.21}$$

$$\tau_{\chi\zeta} = c_f\rho|u|\vec{u_\chi} = c_f\rho u^2 \cos\beta \tag{2.22}$$

The wave impulse depends on the wave impact velocity (u_{imp}) which equals the absolute velocity of the wave. The impact velocity has a vertical and a horizontal component. The horizontal component is assumed to be equal to the horizontal velocity at the crest, since it experiences negligible resistance in the separated state. The vertical component is caused by gravitational acceleration, between the moment of wave separation and the moment of impact. The wave impact velocity is given by Equation 2.23. The flow velocity at the crest is given by u_{crest} and the travelled vertical distance by the water between the point of wave separation and the point of impact is given by Z_{wave}.
The travelled vertical distance is different for different parts of the overtopping wave. It is assumed that the wave is a laminar flow when separated. The water at the surface of the wave when it is at the crest has thus a have larger impact than water at the bottom of the wave. This difference is small and therefor the impact force is approached by the maximum impact force.

$$u_{imp} = |u| = \sqrt{u_{crest}^2 + 2gZ_{wave}} \tag{2.23}$$

Substitution of the wave impact location in Equation 2.23 and subsequent substitution of Equation 2.23 in stress Equations 2.21 and 2.22, gives an expressions for the normal and shear impact stresses, given by Equations 2.24 and 2.25 respectively. (For more detailed derivation, see Ponsioen [2016].) The angle of impact ϕ expressed by Equations 2.26. Further, θ represents the slope angle and h_{crest} the water depth at the crest.

$$\sigma_{\zeta\zeta,max} = \rho u_{crest}^2(1 + 2\tan^2\theta + 2\tan\theta\sqrt{\tan^2\theta + \frac{2gh_{crest}}{u_{crest}^2}})\cos\phi \tag{2.24}$$

$$\tau_{\chi\zeta,max} = c_f\rho u_{crest}^2(1 + 2\tan^2\theta + 2\tan\theta\sqrt{\tan^2\theta + \frac{2gh_{crest}}{u_{crest}^2}})\sin\phi \tag{2.25}$$

$$\phi = \tan^{-1}\left(\tan\theta + \sqrt{(\tan\theta)^2 + \frac{2gh_{crest}}{u_{crest}^2}}\right) - \theta \tag{2.26}$$

Spatial variation of stresses causes a pressure-gradient force, directed parallel to the slope from a point with a higher stress towards a point with a lower stress. Especially the variation between the stress in the impact area and just outside of it is large. Accordingly, a large pressure-gradient force is expected between the impact area and adjacent soil.

The approach of the wave impact load can be improved by application of the theory on *pressure impulse theory for liquid impact problems* (Cooker and Peregrine [1995]). This theory is further explained in Appendix D. In this research this improvement is omitted.

2.4 Composition of a cover layer

Strength of a dike cover layer strongly influenced by its heterogeneity. A cover consists of clay and grass with overlapping zones. Both are non-isotropic elements with different characteristics. Muijs [1999] recognizes distinct components in the cover layer, see Figure 2.7. The flexible, upper part of the grass is the *sward*, the lower and stiffer part the *stubble*. Together with the subsurface parts of the grass, the roots, they form the *herbage*. The subsurface zone with close packed roots and the stubble together form the *turf*. The cover layer below the turf is the *substrate*.

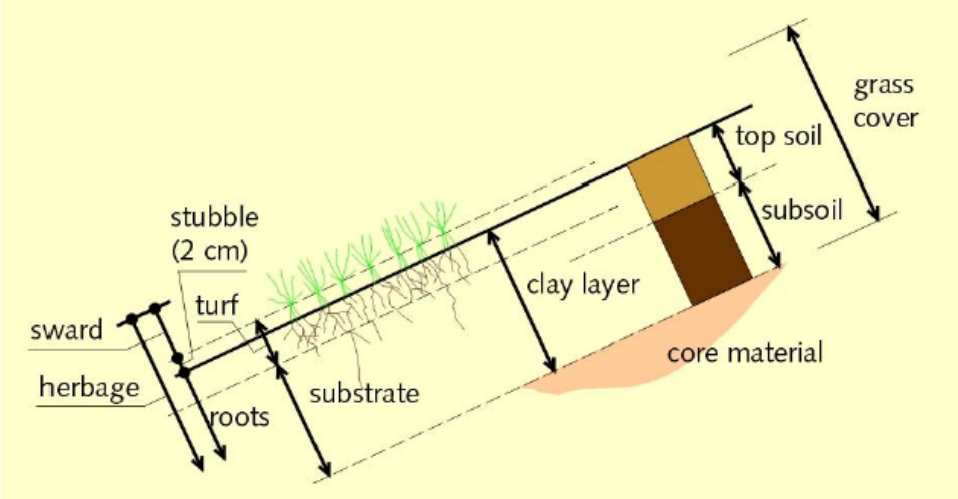

Figure 2.7: Distinction of components of a grass cover layer (Muijs [1999])

Clay in a dike cover is not uniform. It contains cracks and aggregates of various dimensions, especially when it is sparsely vegetated (TAW [1996a], Coppin and Richards [2007]). They are caused by burrowing animals, changing ground water conditions or geological conditions. Cracks and aggregates in the soil are weak spots that are vulnerable for erosion.

The purpose of grass is to protect and reinforce the soil below. A dense and regular grass cover is beneficial for the resistance against (Sprangers [1999]). An open spot in the vegetation is vulnerable for erosion and potentially the initiation location of failure. Grass roots are holding soil aggregates together (Stanczak et al. [2008]). Coppin and Richards [2007] show that vegetation protects soil from drying out; absence of vegetation can lead to additional cracks in the soil.

2.5 Geomechanical resistance

This section describes soil characteristics provide resistance. The first are the strength in the shear and in the normal direction, discussed in Sections 2.5.1 and 2.5.2 respectively. Soil strength variability and the conditions this variability depends on is discussed in Section 2.5.3.

Soil stress consists of effective soil stress (particles stress) and the pore water pressure. Equation 2.27 shows this relation with σ being the soil stress, σ' the effective soil stress and p the pore water pressure. Common geotechnical computations assume either fully drained ($p = 0$) or fully undrained soil ($p = \sigma$). However, in reality loading and unloading causes the degree of saturation to change (Lloret-Cabot et al. [2018]).

$$\sigma = \sigma' + p \tag{2.27}$$

2.5.1 Soil strength

The theory of Coulomb [1776] the critical shear stress that soil is able to withstand depends on cohesion and friction. The latter depends on angle of repose and the governing effective stress. The relation is given in Equation 2.28. Here τ_c is the critical shear strength, c is the cohesion, σ' is the normal effective stress and ϕ is the angle of repose. Mohr's circle (Mohr [1900]) describes and visualizes all possible combinations of shear stress and normal stress (stress states) for certain loading conditions.
The Mohr-Coulomb criterion states that for preventing failure of the soil all stress states must be below the critical stress states given by Equation 2.28. The Mohr-Coulomb criterion is visualized in Figure 2.8. The figure shows a case for which two stress states are critical (indicated by C and D) and all others (other points on the circle) are below critical. The Mohr-Coulomb criterion gives the expected angle of a failure plane.

$$\tau_c = c + \sigma' \tan \phi \tag{2.28}$$

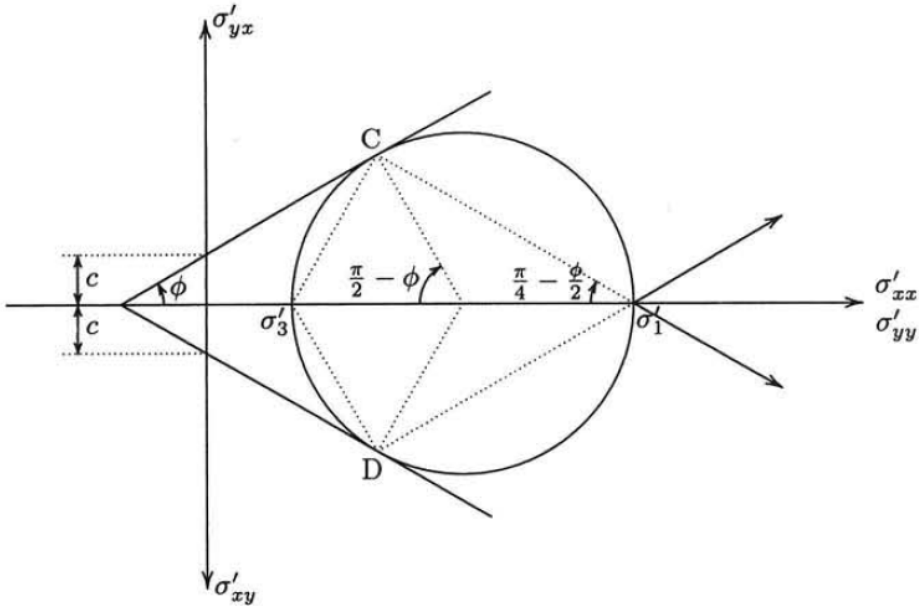

Figure 2.8: The Mohr-Coulomb criterion. The circle represents possible combinations of shear and normal effective stress. The straight lines represent critical combinations of shear and normal effective stress.

According to the Mohr-Coulomb criterion for all stress states a soil element orientation exists for which only normal stresses act on the element. These normal stresses are the major principle stress (σ'_1) and the minor principle stress (σ'_3). The relation between the normal and shear stresses and the principle stresses are given in Equation 2.29. Here α gives the rotation angle that a soil element must rotate with respect to the horizontal position for the shear stress to become zero. Equation 2.30 expresses the relation between the principle stresses (Verruijt and van Baars [2009]).

$$\begin{bmatrix} \sigma'_{xx} & \tau'_{xz} \\ \tau'_{zx} & \sigma'_{zz} \end{bmatrix} = \frac{1}{2}(\sigma'_1 + \sigma'_3)\begin{bmatrix} 1 & 0 \\ 0 & 1 \end{bmatrix} + \frac{1}{2}(\sigma'_1 - \sigma'_3)\begin{bmatrix} -\cos 2\alpha & \sin 2\alpha \\ \sin 2\alpha & \cos 2\alpha \end{bmatrix} \tag{2.29}$$

$$\sigma'_3 = \sigma'_1 \frac{1 - \sin\phi}{1 + \sin\phi} + 2c\frac{\cos\phi}{1 + \sin\phi} \tag{2.30}$$

Angle of repose

Particle interlocking causes soil to have an angle of repose. This is the steepest angle at which the an unsupported slope angle remains stable. Common design practice is to use the drained angle of repose, which is roughly between 15° and 30° for clay (Verruijt and van Baars [2009], NEN [2007]). The angle of repose goes to zero for a saturated soil, explained by the three phenomena listed below (Terzaghi [1932, 1936]).

1. *Soil strength depends on intergranular forces only;*
2. *The pore volume is large and interconnected enough to make the pore water pressure not affect intergranular forces;*
3. *The incompressible water fully carries pressure changes. Unless drainage occurs, the soil structure (hence the soil volume) remains unchanged.*

These phenomena and the angle of repose for among others clay are tested and shown to be just (Terzaghi [1936], Golder and Skempton [1948], Bishop and Eldin [1950]). The third phenomena is proved by Smeulders [1992] and van der Grinten [1987].

An accessible test to obtain the angle of repose is the *Simple Shear Test (SST)*, in which a soil is exposed to an angular deformation (Roscoe [1953]). The horizontal stress, required for the Mohr-Coulomb failure criterion, is not exactly known in the SST, introducing some uncertainty in the results. An accurate but extensive test to find the angle of repose is the *Triaxial shear test*. In this test a sample is exposed to both an axial and a radial stress, till failure. Based on the conditions at failure, the accompanying Mohr's circle is drafted. If the cohesion is known or if multiple tests are executed, the angle of repose can be determined.

Cohesion

Cohesion is shear strength that is independent from the governing normal stress. It originates from connections between individual particles. Cohesion is an umbrella term consisting of different connecting mechanisms. Mechanisms that contribute to the cohesion are chemical binding (cementation), particle interlocking, water affinity of clay particles and suction pressure (TAW [1996a], Mitchell [1993]). Cohesion is an isotropic

soil characteristic. According to Verruijt and van Baars [2009] cohesion of clay is between 5 kPa and 50 kPa (or even larger). Practical values of the cohesion are lower. NEN [2007] assigns values from 0 kPa (no cohesion) up to 15 kPa to the cohesion of clay. The cohesion of clay depends on the history of load. Loading and subsequently unloading (*overconsolidation*) increases the cohesion. This increase can be approached by the *Overconsolidation Ratio (OCR)* (Casagrande [1936]).
The cohesion of a soil can be determined by executing a Triaxial shear test. If the angle of repose is known or if multiple tests are executed, the cohesion can be determined.

2.5.2 Compression

The development of soil stresses and strain (ε) are related to each other. Every doubling of the stress generates an equal compression (Terzaghi [1940]). It is expressed in a logarithmic relation, see Equation 2.31 (Keverling Buisman [1941]). In this formula is σ the governing stress, σ_1 the stress before loading and C_{10} is a dimensionless compression coefficient that describes the relation between stress increases and compression. According to Verruijt and van Baars [2009] C_{10} of clay has a value between 4 and 40. Koppejan [1948] added time dependency with Equation 2.32. In this equation C_p and C_s are the primary and secondary compression coefficient respectively and t is the load time. The time is expressed in days, indicating the large time span of the calculated compression.

$$\varepsilon = \frac{1}{C_{10}} \log(\frac{\sigma}{\sigma_1}) \tag{2.31}$$

$$\varepsilon = -(\frac{1}{C_p} + \frac{1}{C_s} \log(t)) \log(\frac{\sigma}{\sigma_1}) \tag{2.32}$$

Verruijt [2008] gives the relation between effective stress and strain, see Equation 2.33. K is the compression modulus, which is a measure for the relation between stress and strain (comparable to the function of the C_i coefficients in previous relations). G is the shear modulus, expressing shear. These moduli cover the elasticity and the lateral effects of the soil compression.

$$\varepsilon_{ii} = -\frac{\sigma'_1}{2K + \frac{4}{3}G} \tag{2.33}$$

The history of loading influences the stiffness of the soil. Soil that has been loaded and unloaded repeatedly reacts more stiff during loading than soil during a virgin loading. This effect is shown in Figure 2.9.
The compression strength of soil is measured with the *oedometertest*. In this test a soil sample is put in a ring, to prevent occurance of horizontal deformation. Hence, vertical strain equals volume strain. The sample is covered by a circular, porous plate which is loaded. The relation between the compression (vertical displacement) and the load gives the compression strength.

Isotropy
Consolidation and settlement causes vertical soil compression. This and the lack of

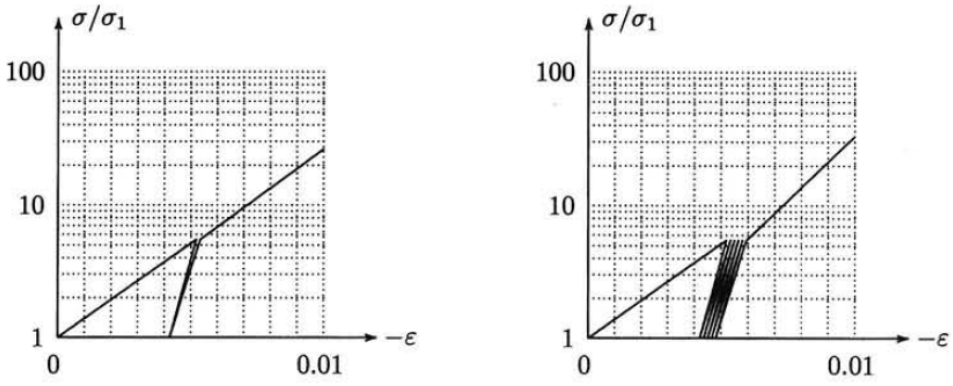

Figure 2.9: The effect of multiple loading events on the stiffness of soil (Verruijt and van Baars [2009]).

horizontal motion causes a layered composition of the clay particles. This is largely due to the flaky appearance of clay particles, as is explained by Buessem and Nagy [1953]. Logically, this layered state is especially present in clay that is in place for a long time or artificially compressed clay. Clay on a dike can only be the latter, or it is remolded and not layered at all. Ansal and Erken [1989] found that remolded clay samples are more resistant to cyclic shear stresses than layered ones.

Elasticity

Elasticity of soil is approached by the relation of Terzaghi and Young's modulus (E). The relation giving Young's modulus is given in Equation 2.34. Note that it describes a linear relation, but soil behaviour is not linear elastic. The Young's modulus of a type of soil thus changes for changing governing stress in the soil. The governing stress is given by σ, the compression by ε and Young's modulus by E.

$$E = \frac{\sigma}{\varepsilon} \tag{2.34}$$

The value of the Young's modulus of clay has a large spreading (Kezdi [1974], Prat et al. [1995]). Hardness and plasticity of the clay are variables that influence the elasticity. The Young's modulus of hard clays is an order of magnitude larger than that of soft clays. The Young's modulus of clays with limited plasticity is larger (slightly larger to several times larger) than that of highly plastic clays. The latter difference is larger for harder clays. Values of Young's modulus for soft clays lay between 0.3 and 5 MPa. For hard clays this is between 20 and 70 MPa. For one type of clay there is quite some spreading in the Young's modulus. The spreading in the value is larger for softer clays.

According to Bijlard [2015] previous research states that the modulus of elasticity of grass can be linked to the Young's modulus of pine wood ($\approx 9GPa$). Figure 2.10 shows that the Young's modulus of all wood like material (among which grass and pine wood) is in the same region. Research on in-situ grass by Bijlard [2015] shows that the Young's modulus of a grass cover has an order of magnitude 0.1 GPa.

Lateral effects

Equation 2.34 is a simplified approximation of elasticity, based on a one dimensional case. In practice stresses and deformations are three dimensional, complicating the relation between stress and strain. Stresses in a direction also affect the strain in transverse

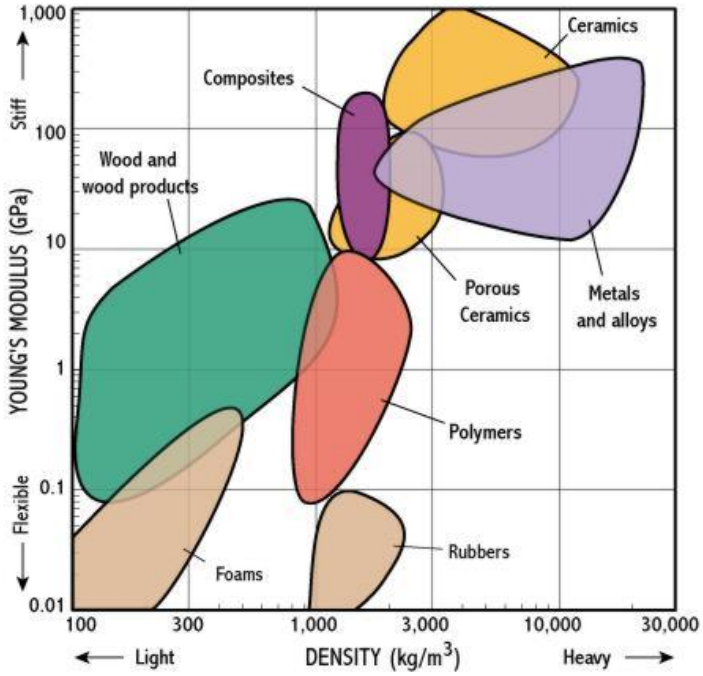

Figure 2.10: Young's modulus of distinct groups of materials (Cambridge University [2002])

directions. The ratio between axial and transverse strain is expressed with Poisson's ratio (ν). The value of Poisson's ratio is material dependent. Application of Poisson's ratio in Equation 2.34 gives Equation 2.35.

$$\begin{bmatrix} \varepsilon_{xx} \\ \varepsilon_{yy} \\ \varepsilon_{zz} \end{bmatrix} = \frac{1}{E} \begin{bmatrix} 1 & -\nu & -\nu \\ -\nu & 1 & -\nu \\ -\nu & -\nu & 1 \end{bmatrix} \begin{bmatrix} \sigma_{xx} \\ \sigma_{yy} \\ \sigma_{zz} \end{bmatrix} \tag{2.35}$$

Values of Poisson's ratio for clay show large variation (Patel et al. [2017]). An upper boundary of Poisson's ratio, applying to saturated undrained clay, is 0.5 (Yokota and Konno [1980], Pickering [1970]). Partially saturated clay has a Poisson's value roughly somewhere between 0.4 and 0.5. The Poisson's ratio shows dependencies on soil conditions (Pan et al. [2010]). The occurring shear strain is of large influence on the Poisson's ratio. For small strains ($\eta \approx 0.0001$), Poisson's ratio can get as small as 0.2. The ratio of the axial over the normal (in lab tests: radial) stress and the effective confining soil pressure are of minor influence.

Modeling damped elastic behaviour

A simple way to model elastic behaviour of the soil is drafted by Winkler [1867]. In this model soil is represented by a number of discrete, independent, linear elastic springs. Each spring represents a certain surface of the soil. The strain is related to the applied force with the spring constant. Using the represented surface per spring, the force can be translated into a stress. With this stress Young's modulus is determined, relating the spring constant in the model to the Young's modulus of the soil (Lysmer and Kuhlmeyer [1969]).

An extension to this model is the Kelvin-Voigt model (Figure 2.11) where damping is included by adding a dashpot parallel to the spring. This is applied in the Winkler model

in Figure 2.12. This model is found to be representative for the behaviour of soil (Cuomo et al. [2011], Al-Kafaji [2013]).

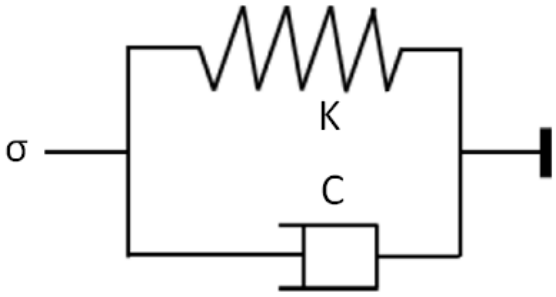

Figure 2.11: Kelvin-Voigt diagram with a spring element, representing elasticity (K), and a dashpot element representing damping (C).

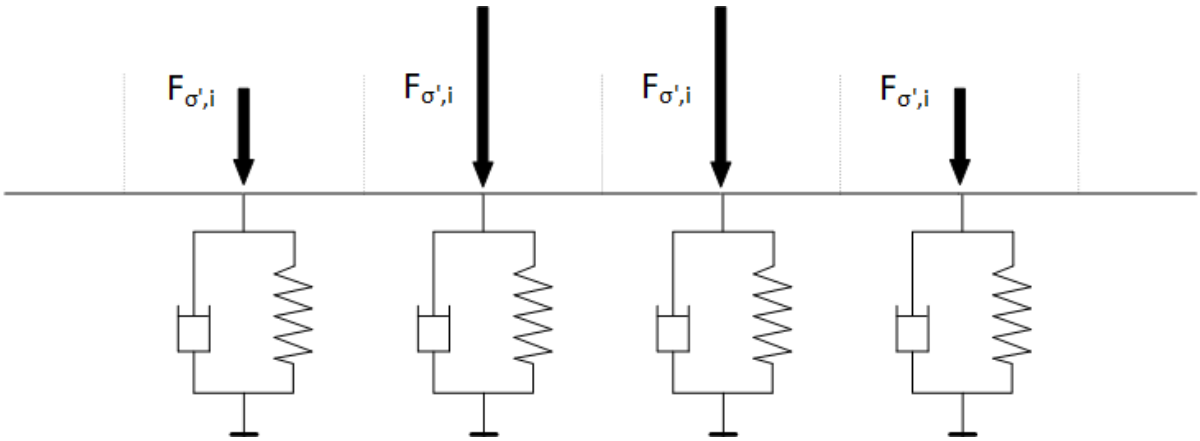

Figure 2.12: Soil layer springy and damping support modelled by a Winkler model with Kelvin-Voigt diagrams, for a random load.

2.5.3 Factors influencing strength

Degree of saturation

The degree of saturation of the soil influences the state of the soil and its behaviour. A conventional geotechnical model uses either a fully saturated or a fully unsaturated approach. However, correct modelling of degrees of saturation in between is required to properly represent soil behaviour (Elsafti [2015]).

The Atterberg limits demarcate distinct soil states (Casagrande [1932]). The soil states are, from most solid to most liquid, *solid*, *semi-solid*, *plastic* and *liquid*. The limits that separate the soil states are called the *Atterberg Limits*. They are, from most solid to most liquid, the *Shrinkage Limit*, the *Plastic Limit* and the *Liquid Limit*. Each limit is based on a different test.

The infiltration rate of soils is described by the hydraulic conductivity (Green and Ampt [1911], Hendriks [2010]). The hydraulic conductivity is expressed by Darcy's law (Darcy [1856]). Although Darcy's law neglects factors that are considered by more elaborate

models, it gives an order of magnitude of the infiltration rate. According to Bear [1972] the hydraulic conductivity for clay is 10^{-6} m/s or smaller.

It is a common approach to assume saturated soil during overtopping (e.g. Hoffmans et al. [2008]). No strength reduction by soil infiltration is expected during overtopping. Moreover, from Bear [1972] is concluded that soil saturation is not influenced by a single overtopping wave. Infiltration can be influential on unsaturated soils.

Fatigue
Load repetition influences the strength of clay by remolding of the particle composition (Yasuhara et al. [1982]). The strength of the soil decreases after multiple load cycles (Bijlard [2015]). Further, the modulus of deformation increases. Based on axial loading laboratory tests, shear strength reductions up to 65% are found (Ansal and Erken [1989]). The existence of a strong relation between the applied cyclic stress and the number of load repetitions before failure is shown by Yasuhara et al. [1992]. He also shows that clay fails for repetitive load below the critical stress.

Fatigue itself is not a soil characteristic. It influences other characteristics, such as Young's modulus. Its influence is only relevant for an overtopping event with multiple overtopping loads.

2.6 Soil pressure measurements

Measurements of pressure development in the soil are done during overtopping simulations at dikes at *Millingen aan de Rijn* (Verheij et al. [2015]). Pressure is measured at the surface and at a certain distance below it. Reference pressure is the pressure at the an unloaded surface, that is the atmospherical pressure. The measured pressure at the surface and in the soil is the (pore) water pressure. At the surface, this equals the total pressure. Sensors measured signals with a 5000 Hz frequency.

Surface pressure is measured by a pressure sensor placed at surface level in the soil. Pressure in the soil is measured by a pressure sensor at approximately 10 cm below the surface. It is installed by boring a hole from outside the test area to the sensor location. The test setup is shown in Figures 2.13 and 2.14.

Results are presented in a 10 s time span per wave. Besides pressure, the results contain measurements on other wave characteristics, such as velocity and thickness. Two measured waves are selected from the results. These waves are selected because all considered measurements are complete and the results show a clear reaction of soil stresses. Selected pressure measurements are shown in Figure 4.12. The dark red line gives the surface pressure and the blue line the soil pressure. The results show that the pressure reaction in the soil is marginal. This indicates damping and the diffusion of the absolute value and the amplitude of pressure over depth. The suction pressure shown in Figure 2.15a is explained with the presence of unsaturated soil during the first tests by Verheij et al. [2015].

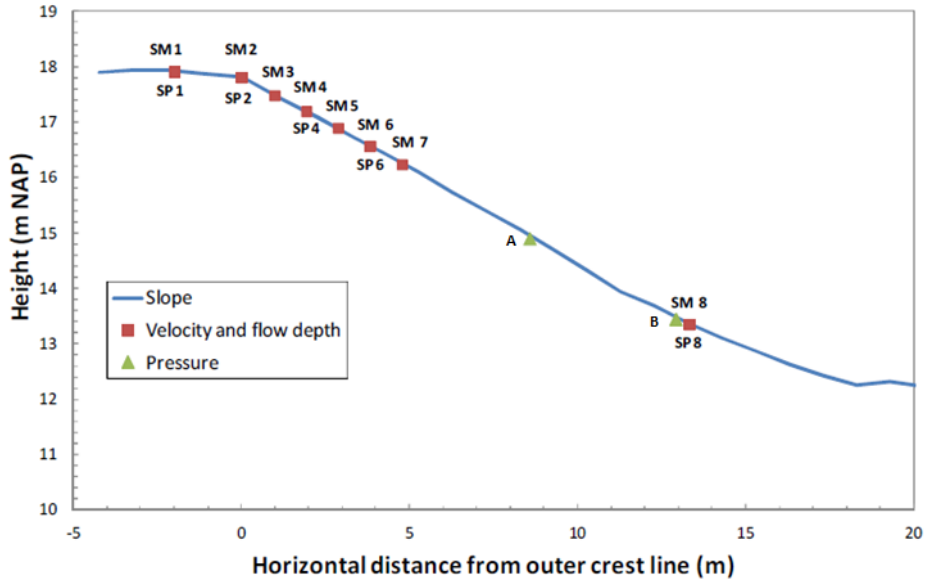

Figure 2.13: Cross section of the test setup during the measurement campaign that includes pressure measurement during wave overtopping simulations (Verheij et al. [2015], edited).

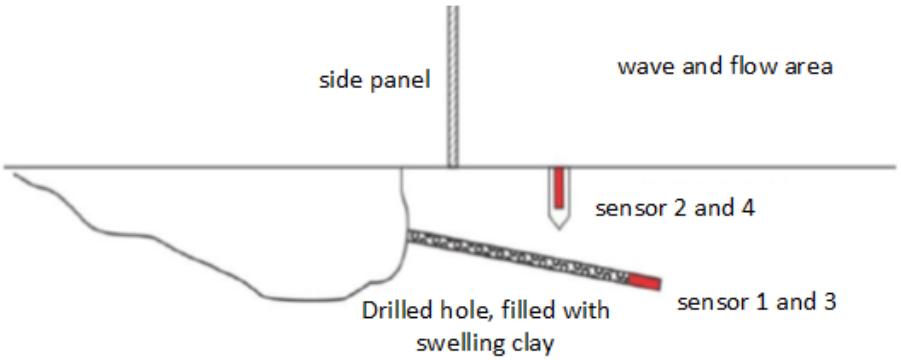

Figure 2.14: Test setup for pressure measurement during wave overtopping simulations (Verheij et al. [2015]).

2.7 Literature conclusions

Conclusions, based on literature, are given in this section. First, in Section 2.7.1, the current knowledge on the process of failure due to changing soil stress is summarized. Next, in Section 2.7.2 a model outline is drafted.

2.7.1 Conclusions on knowledge

Due to the complexity of overtopping, there are many types of failure due to overtopping (Section 2.1). Some types are related directly to the stress in the soil, e.g. head-cut failure or soil lifting failure (described by the Turf Element Model). Some types, like collapse failure or layer sliding failure, also depend on local variations in soil strength.

The different appearances arise from the different load mechanisms within one overtop-

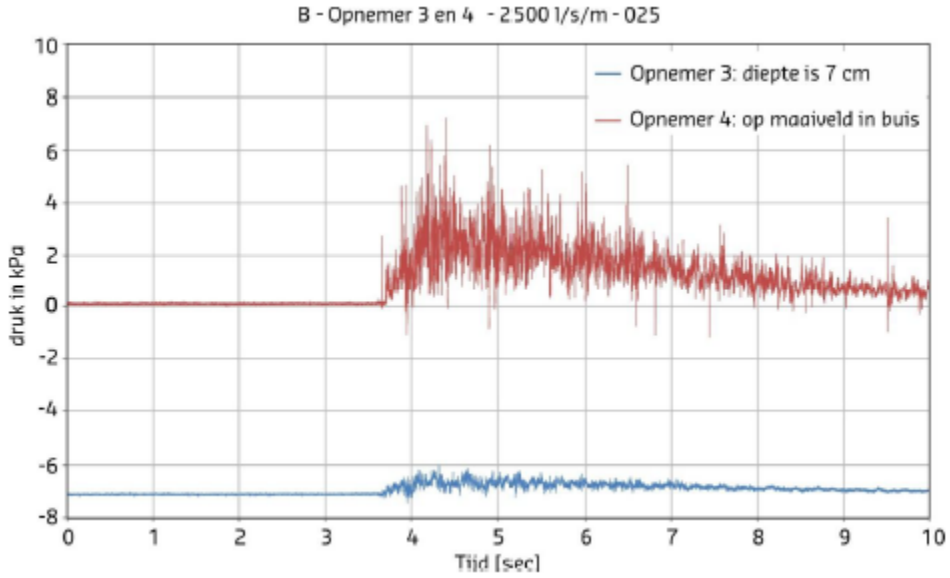

(a) Pressure development for an overtopping wave volume of 2500 l/m, at location B, during test series 1.

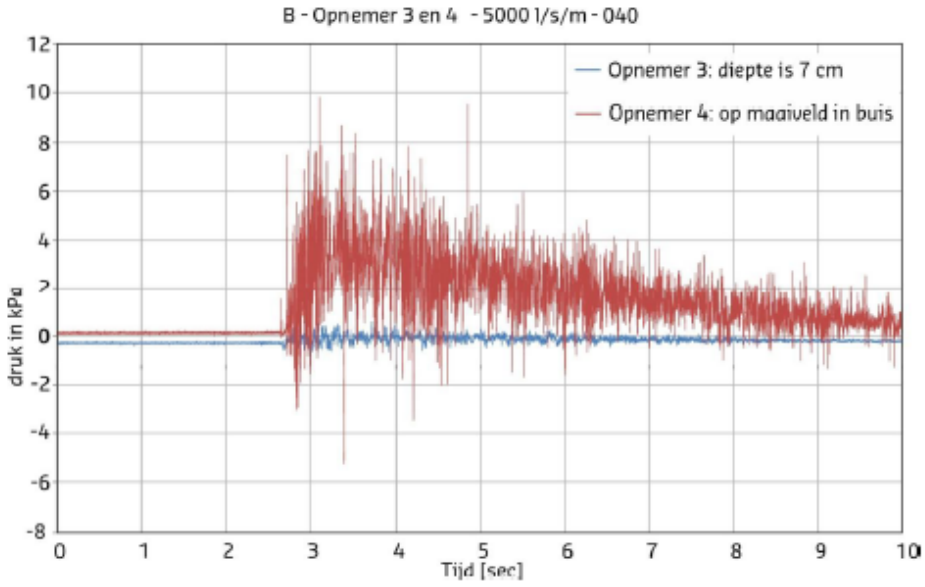

(b) Pressure development for an overtopping wave volume of 5000 l/m, at location B, during test series 1.

Figure 2.15: Pressure development as function of time for sensor 3 below surface and sensor 4 at surface (Verheij et al. [2015].

ping wave (Section 2.3) and the wave development during one overtopping wave cycle (Section 2.2). The magnitude of load on the slope differs in space and time during one cycle and also between overtopping wave cycles. The normative load can be different for each overtopping wave.

Parts of the wave load, that are likely to be normative, are the locations of the wave impact and the wave front. At the location of the wave impact the normal stress peaks very locally. At the location of the wave front there are large stress gradients. Furthermore, at this location the stresses are the largest of the entire wave (excl. wave impact).

A difference exists between the reaction of different soil stress components to load (Section 2.5). Load (assume pushing) on the soil causes an increase in the total soil stress. Initially this increase is fully carried by the pore water pressure. The influence of loads of short duration on the effective stress is negligible.
For a constant load at a finite area the following chain of events is expected. The load causes an increase in soil pressure, causing an initially equal increase in pore water pressure. This causes a water pressure gradient, hence water outflow which decreases the pressure gradient. The water flow continues as long as a pressure gradient exists. Soil volume decreases (negative strain) due to water outflow. The decrease in pore water pressure and the decrease in volume cause an increase in effective stress. The described chain of events is shown in Figure 2.16. Failure is expected to occur when, during this soil reaction, one of the conditions that is listed further down in this section, is met.

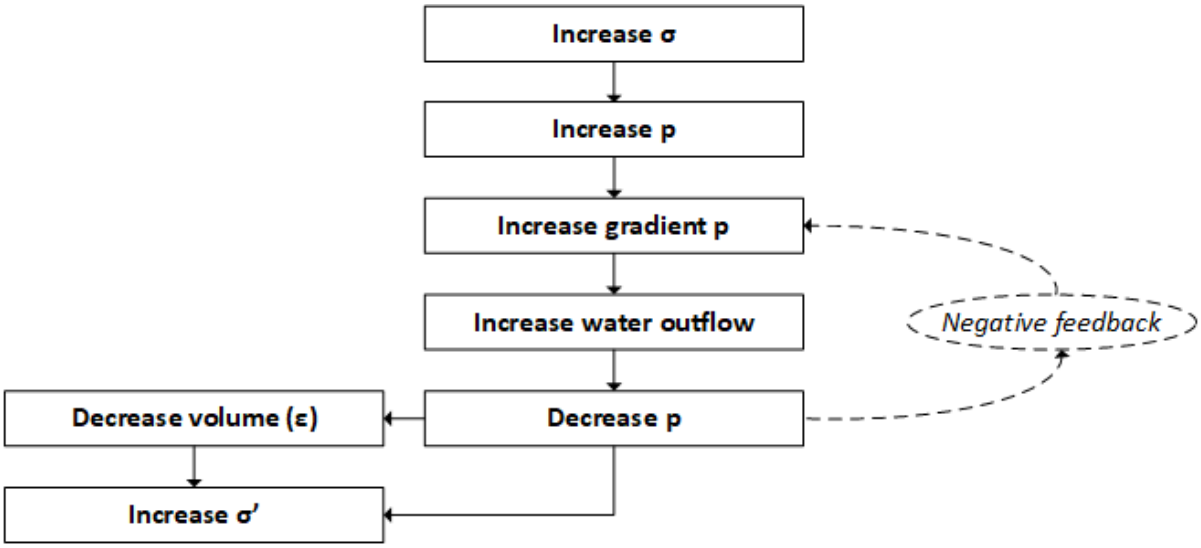

Figure 2.16: Chain of events that is expected as a reaction on surface load.

Soil stress is influenced by a large number of characteristics (Section 2.5). The most important soil characteristics are the cohesion, angle of repose, the (lateral) elasticity and hydraulic conductivity (which defines the infiltration speed). The cohesion is a measure for the extend to which soil particles are connected to each other. It defines the strength of the soil on very small scale. The angle of repose is a measure for the ability of the soil to pile up. A large angle of repose is favorable for the soil strength against collapsing. However, the angle of repose of saturated clay is very small. The elasticity of the soil (expressed by Young's modulus and Poisson's ratio) is a measure for the relation between the occurring stress and strain. It influences the speed to which the soil can adapt to the new load situation. The hydraulic conductivity is a measure for the flow velocity of pore water, which also influences this adaptations speed. This adaptation speed is relevant regarding geotechnical failure. A low adaptation speed can lead to local pressure build-up and large stress gradients. During model development it is shown that some soil characteristics can be neglected (Section 3.1.3).

In practice uncertainty exists on the values of specific soil characteristics. A reason for this is the spatial variability of soil. This means that also strength characteristics are location dependent. This is of influence on geotechnical failure.

Geotechnical failure is related to soil stresses but knowledge on short term soil behaviour under variable loading conditions is limited. Suitable modelling of short term soil stress reaction can provide additional insight in this behaviour. The distribution and development of soil stresses provide information on causes of failure. When soil strength is considered as well, failure can be predicted. Geotechnical failure can be expected from three combinations of stress and soil strength:

- High soil stress on local weak spot;
- Negative effective soil stress;
- Stress gradient force exceeding the soil strength.

2.7.2 Conclusions on modelling

To improve knowledge on geotechnical failure related to soil stress, a soil stress model is developed. Stresses are computed in a 2D space, representing a part of the cross section of the land side slope of the dike. Stresses are approached numerically, in a finite element grid. The model represents soil behaviour, as summarized in Section 2.7.1. It shows the distribution and development of total stress, effective stress and pore water pressure for a given load.

The soil stress model must be able to deal with load variation on short scale in space and time.
The model results must show stress increase for a pushing load and a stress decrease for a pulling load. It must show that the pore water pressure initially carries load changes and gets relieved in time. On the contrary, the effective stress is initially not influenced by load changes but starts carrying the load as time passes.
The soil stress at the surface must adapt to the surface load. It must carry the load, by the effective stress and the pore water pressure. Both side boundaries of the model must be of no influence on the model. They must be such that the model can be a representation of a random section of an infinite long, loaded clay layer. At the bottom of the model an interface between a clay layer and a sand layer (commonly constructed sublayer) must be represented. Sand is stiffer than clay, causing more effective stress build-up at the bottom, and more permeable than clay, causing no restrictions on flow of water through the bottom.

A good image of the distribution and development of stresses, indicates occurrence of immediate failures (that is during a certain stress state). Failure caused by soil lifting, head-cut failure or of different scale (Turf Element Model) can be predicted well by the model. Furthermore, the model possibly reveals blind spots on knowledge on geotechnical failure. Additional knowledge on the spatial variability of soil strength improves the capability of the model to indicate collapse failure and layer sliding failure. During gradually developing failure, such as roll-up failure, soil stresses change, in particular around the changed geometry of the location of initial failure. This applies to development of failure (after initial damage) as well. The model is not yet suited to predict these types and paths of failure.

3

Methodology

This chapter presents the approach to the third objective. A first step is to derive model equations, that describe soil pressure development for a given load. These equations are derived from accepted theory on soil forces such as impulse and mass balances. Derivation of model equations is given in Section 3.1.
Subsequently, a model is drafted from the model equations, initial conditions and boundary conditions. The boundary condition at the surface determines the ratio between the water pressure and the effective stress. Since this develops during load and since the load is applied on the surface boundary, the surface boundary condition is more complicated and of larger effect on the model results, than other boundary conditions. The initial and boundary conditions are given in Sections 3.2, 3.3, 3.4 and 3.5.
The model is set up in a model framework with distinct point in space and time. The stress equations, boundary conditions and initial conditions are discretized to be able to apply them on the model framework. These steps are explained in Section 3.6.
To determine the load on the geomechanical part of the model, different modes are optional. With the *manual* mode the surface stresses on each point in space and time must be defined manual, which is suitable for simple loads (e.g. constant in space or time). Application of this mode is suitable for model verification computations and simple indicative computations. With *wave load* mode the surface stress during an overtopping wave is computed. The background of this mode is given in Section 3.7. Application of the wave load mode is suitable for model verification by comparison with measurements and predictive computations when the model is ready to use.
In drafting the model a number of equations is made, which are put together in Section 3.8.

Once drafted the model is used, see Chapter 4. Results of model use shows to weaknesses, flaws and/or usability limits of the model. This can be used to improve the model, leading to a continuous iterative process of modelling and model use.

3.1 Balance equations describing pressure development

A numerical model computing the propagation of soil pressure under an overtopping load is drafted. It models soil in a two-dimensional space along the cross section of the dike. The soil is divided in distinct rectangular cells. Normal and shear forces act on the the edges of the cell, shown in Figure 3.1. These forces originate from soil stress in adjacent cell or, for model boundary cells, boundary conditions.

Forces in the soil are described by balance equations describing horizontal and vertical impulse and mass of water and particles, given in Sections 3.1.1 and 3.1.2. In Section 3.1.3, these balance equations are transformed to a single equation, expressing the stress in the soil in terms of the major principle stress. Derivation of the model equations is based on van Damme [2018b]. All stresses are expressed in a frame of reference with an x-axis parallel to and a z-axis normal to the soil slope.

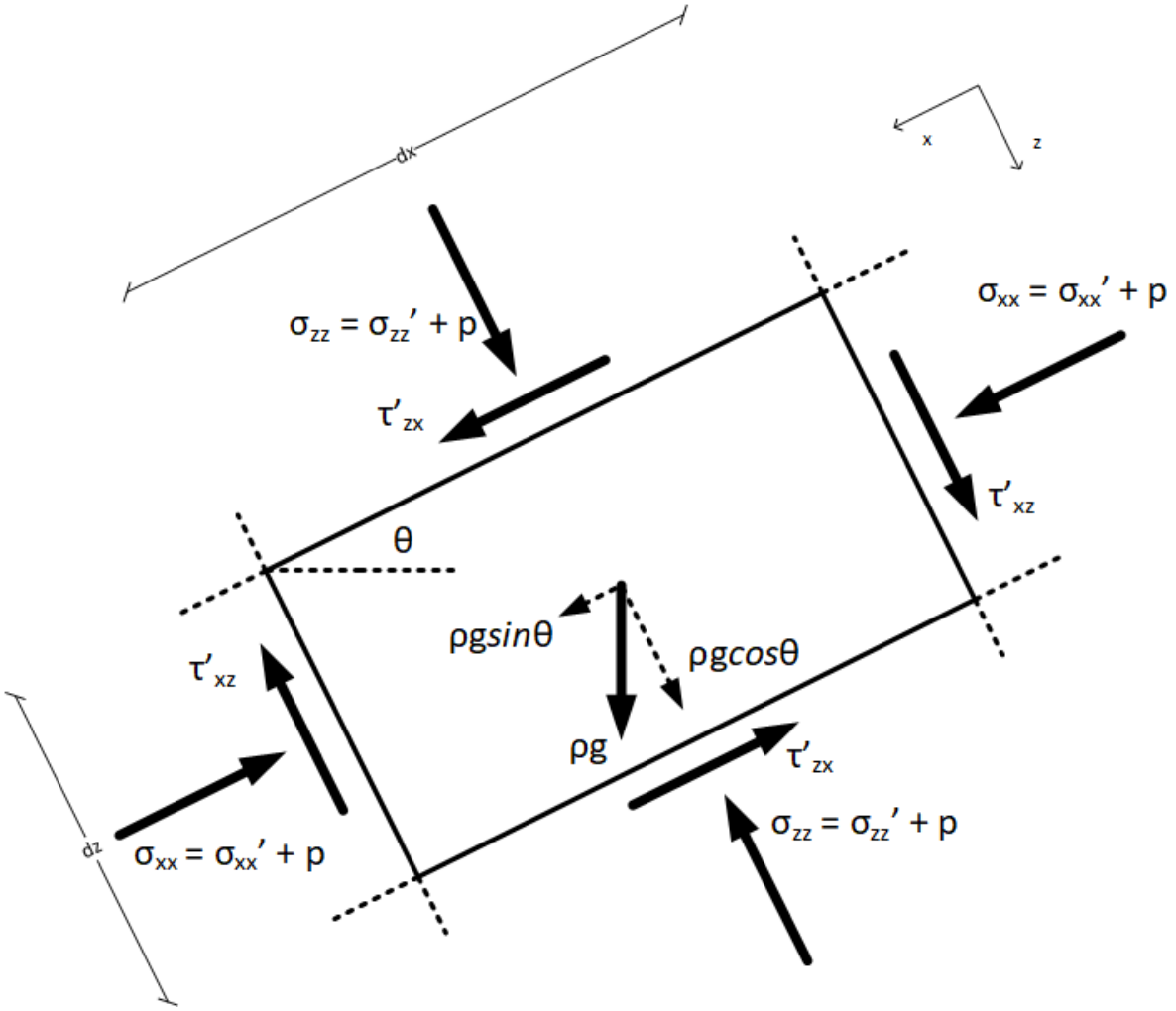

Figure 3.1: Forcing on an inclined soil element of finite dimensions.

3.1.1 Impulse balance

The impulse balances in x and z direction for a saturated sloping soil are given by Equations 3.1 and 3.2 respectively (Verruijt and van Baars [2009]). Soil is likely to be saturated during an overtopping event (e.g. Bijlard et al. [2017]). The gradients in effective shear stress (τ'), effective normal stress (σ') and the pore water pressure (p) and the gravitational force contribute to the balance. The pore water pressure is isotropic, the effective soil stress and the effective shear stress are not. The slope angle is given by θ and the soil density by ρ_s. The described forces on the soil are displayed in Figure 3.1.

$$\frac{\partial \sigma'_{xx}}{\partial x} + \frac{\partial \tau'_{zx}}{\partial z} + \frac{\partial p}{\partial x} = \rho_s g \sin\theta \tag{3.1}$$

$$\frac{\partial \sigma'_{zz}}{\partial z} + \frac{\partial \tau'_{xz}}{\partial x} + \frac{\partial p}{\partial z} = \rho_s g \cos\theta \tag{3.2}$$

3.1.2 Mass balance

Initiation of failure is considered, that is before occurrence of plastic deformation. In this situation, the principle of mass balance is applicable. The mass balance for soil particles is given by Equation 3.3 and for pore water by Equation 3.4. Here n is the porosity and u is the average velocity of a soil particle. The subscripts w and p denote water and particles respectively.

$$\frac{\partial \rho_p (1-n)}{\partial t} + \nabla (1-n)\rho_p u_p = 0 \tag{3.3}$$

$$\frac{\partial \rho n}{\partial t} + \nabla n \rho u_w = 0 \tag{3.4}$$

It is more likely that stress increase causes a volume change than compression of individual soil particles, giving that soil density is constant in time. Assuming homogeneity of soil, the density is constant is space. Constant soil density reduces Equation 3.3 to Equation 3.5. Water is considered to be incompressible and homogeneous, similarly reducing Equation 3.4 to Equation 3.6.

$$\frac{\partial (1-n)}{\partial t} + \nabla (1-n) u_p = 0 \tag{3.5}$$

$$\frac{\partial n}{\partial t} + \nabla n u_w = 0 \tag{3.6}$$

3.1.3 Derivation of model equations

The effective stresses and the principle stresses in the soil are described by Mohr's circle (see Figure 2.8) and accompanying relations (Equations 2.29 and 2.30, repeated by Equations 3.7 and 3.8).

$$\begin{bmatrix} \sigma'_{xx} & \tau'_{xz} \\ \tau'_{zx} & \sigma'_{zz} \end{bmatrix} = \frac{1}{2}(\sigma'_1 + \sigma'_3)\begin{bmatrix} 1 & 0 \\ 0 & 1 \end{bmatrix} + \frac{1}{2}(\sigma'_1 - \sigma'_3)\begin{bmatrix} -\cos 2\alpha & \sin 2\alpha \\ \sin 2\alpha & \cos 2\alpha \end{bmatrix} \tag{3.7}$$

$$\sigma'_3 = \sigma'_1 \frac{1 - \sin\phi}{1 + \sin\phi} + 2c\frac{\cos\phi}{1 + \sin\phi} \tag{3.8}$$

The derivatives of stresses, obtained from Equation 3.7, are substituted in the impulse balance equations (Equations 3.1 and 3.2). By substituting Equation 3.8 into it, the impulse balances are expressed as a function the major principle stress as only stress. The cohesion of clay is assumed to be constant in space and time causing the last term of Equation 3.8 to be constant and dropping out with derivation. The resulting derivatives of the normal stresses are given in Equations 3.9 and 3.10 and of the shear stresses in Equations 3.11, 3.12, 3.13 and 3.14.

$$\frac{\partial \sigma'_{xx}}{\partial x} = \frac{\partial}{\partial x}\left(\frac{1 + \cos 2\alpha \sin\phi}{1 + \sin\phi}\sigma'_1\right) \tag{3.9}$$

$$\frac{\partial \sigma'_{zz}}{\partial z} = \frac{\partial}{\partial z}\left(\frac{1 - \cos 2\alpha \sin\phi}{1 + \sin\phi}\sigma'_1\right) \tag{3.10}$$

$$\frac{\partial \tau'_{xz}}{\partial x} = 2\frac{\partial}{\partial x}\left(\frac{\sin\phi \sin 2\alpha}{1 + \sin\phi}\sigma'_1\right) \tag{3.11}$$

$$\frac{\partial \tau'_{xz}}{\partial z} = 2\frac{\partial}{\partial z}\left(\frac{\sin\phi \sin 2\alpha}{1 + \sin\phi}\sigma'_1\right) \tag{3.12}$$

$$\frac{\partial \tau'_{zx}}{\partial x} = 2\frac{\partial}{\partial x}\left(\frac{\sin\phi \sin 2\alpha}{1 + \sin\phi}\sigma'_1\right) \tag{3.13}$$

$$\frac{\partial \tau'_{zx}}{\partial z} = 2\frac{\partial}{\partial z}\left(\frac{\sin\phi \sin 2\alpha}{1 + \sin\phi}\sigma'_1\right) \tag{3.14}$$

The angle of repose of clay is a value close to zero (Terzaghi [1932, 1936]), assuming saturated undrained clay, which is valid for the clay layer under overtopping load. If $\phi \to 0$, then $\sin\phi \approx \phi$ (ϕ expressed in radians). Neglecting $\sin\phi$ reduces Equation 3.9 to Equation 3.15 and Equation 3.10 to Equation 3.16. Furthermore it reduces Equations 3.11, 3.12, 3.13 and 3.14 to Equation 3.17, showing that shear stresses are of no influence.

$$\frac{\partial \sigma'_{xx}}{\partial x} = \frac{\partial \sigma'_1}{\partial x} \tag{3.15}$$

$$\frac{\partial \sigma'_{zz}}{\partial z} = \frac{\partial \sigma'_1}{\partial z} \tag{3.16}$$

$$\frac{\partial \tau'_{xz}}{\partial x} = \frac{\partial \tau'_{xz}}{\partial z} = \frac{\partial \tau'_{zx}}{\partial x} = \frac{\partial \tau'_{zx}}{\partial z} = 0 \tag{3.17}$$

According to Darcy's law the water pressure gradient is proportional to the flow through the soil (Equation 3.18, Darcy [1856]). The specific discharge (q) equals the porosity multiplied by the relative velocity of the fluid with respect to the solid (see Equation 3.19). The mass balances in both directions (Equations 3.3 and 3.4) are summed and with substitution of Equation 3.19 rewritten to Equation 3.20. The spatial gradient in discharge is related to the temporal gradient in strain as given by Equation 3.21. In this equation ε gives the volume strain, γ_w the volumetric weight of water and k_s the hydraulic conductivity of the soil. When $\frac{\gamma_w}{k_s}$ is constant, Equations 3.18 and 3.21 are substitutable in each other.

$$\frac{\partial p}{\partial x} + \frac{\partial p}{\partial z} = -\frac{\gamma_w}{k_s} q_x - \frac{\gamma_w}{k_s} q_z \tag{3.18}$$

$$q = n(w_w - w_p) \tag{3.19}$$

$$\frac{\partial n(u_{w,x} - u_{p,x})}{\partial x} + \frac{\partial n(u_{w,z} - u_{p,z})}{\partial z} + \frac{\partial u_{p,x}}{\partial x} + \frac{\partial u_{p,z}}{\partial z} = \frac{\partial q_x}{\partial x} + \frac{\partial q_z}{\partial z} + \frac{\partial \varepsilon}{\partial t} = 0 \tag{3.20}$$

$$-\frac{\gamma_w}{k_s}\left(\frac{\partial q_x}{\partial x} + \frac{\partial q_z}{\partial z}\right) = \frac{\gamma_w}{k_s}\left(\frac{\partial \varepsilon}{\partial t}\right) \tag{3.21}$$

A relation between strain and effective stresses is given by Equation 3.22, assuming a Hookean relation for small displacements and an isotropic material (Verruijt and van Baars [2009]). Here ε is volume strain and ε_{ii} is one dimensional strain, with subscript ii giving the direction. The relation between volume strain and one dimensional strain in a two-dimensional space is given in Equation 3.23 (Verruijt [2008]). Equation 3.22 shows that if $\sigma'_{xx} = \sigma'_{zz} = \sigma'_1$, perpendicular strains are equal ($\varepsilon_{xx} = \varepsilon_{zz}$). Subsequently, Equation 3.24, giving the strain, is derived from Equation 3.23.

$$\begin{bmatrix} \sigma'_{xx} & \tau'_{xz} \\ \tau'_{zx} & \sigma'_{zz} \end{bmatrix} = -(K - \frac{1}{3}G) \begin{bmatrix} \varepsilon & 0 \\ 0 & \varepsilon \end{bmatrix} - 2G \begin{bmatrix} \varepsilon_{xx} & \varepsilon_{xz} \\ \varepsilon_{zx} & \varepsilon_{zz} \end{bmatrix} \tag{3.22}$$

$$\varepsilon_{xx} = \varepsilon_{zz} = -\frac{\sigma'_1}{2K + \frac{4}{3}G} \tag{3.23}$$

$$\varepsilon = \varepsilon_{xx} + \varepsilon_{zz} = \frac{\partial u_x}{\partial x} + \frac{\partial u_z}{\partial z} = -\frac{\sigma'_1}{K + \frac{2}{3}G} \tag{3.24}$$

Parameters K and G in Equations 3.22 and 3.23 are the compression modulus (or bulk modulus) and the shear modulus of the soil respectively. They are expressed as a function of Young's modulus (E) and Poisson's ratio (ν), as is shown in Equations 3.25 and 3.26 (Hölscher [2016]).

$$K = \frac{E}{3(1-2\nu)} \tag{3.25}$$

$$G = \frac{E}{2(1+\nu)} \tag{3.26}$$

To obtain a single equation describing the soil stress state the divergent of Equations 3.1 and 3.2 is summed, giving Equation 3.27.

$$\frac{\partial^2 \sigma'_{xx}}{\partial x^2} + \frac{\partial^2 \tau'_{xz}}{\partial x \partial z} + \frac{\partial^2 p}{\partial x^2} + \frac{\partial^2 \sigma'_{zz}}{\partial z^2} + \frac{\partial^2 \tau'_{zx}}{\partial x \partial z} + \frac{\partial^2 p}{\partial z^2} = 0 \tag{3.27}$$

The terms describing the effective stress and the shear stress are given by the derivatives of Equations 3.15, 3.16 and 3.17. An expression for the terms describing the water pressure is obtained by substituting Equation 3.18 into Equation 3.21, resulting in Equation 3.28. Substituting Equations 3.23, 3.25 and 3.26 into Equation 3.28 and substitution of the result, together with the expressions for the other terms of Equation 3.27 into Equation 3.27, results in Equation 3.29. When the Young's modulus (E), Poisson's ratio (ν), the hydraulic conductivity (k_s) and the weight of water (γ_w) are known, the major principle stress is the only unknown.

$$\frac{\partial^2 p}{\partial x^2} + \frac{\partial^2 p}{\partial z^2} = \frac{\gamma_w}{k_s} \frac{\partial \varepsilon}{\partial t} \tag{3.28}$$

$$-\frac{\partial^2 \sigma'_1}{\partial x^2} - \frac{\partial^2 \sigma'_1}{\partial z^2} + 3\frac{\gamma_w}{k_s} \frac{\partial}{\partial t}\left(\frac{\sigma'_1}{\frac{E}{1-2\nu} + \frac{E}{1+\nu}}\right) = 0 \tag{3.29}$$

3.2 Initial conditions

The initial stress distribution is that of an unloaded slope in stress equilibrium. Note that the soil has two contributing elements to the equilibrium: water and soil particles. Along each line parallel to the slope surface, the soil is at the same depth. Consequently, both the effective stress and water pressure along the x-axis is constant. This gives a zero stress gradient, see Equations 3.30 and 3.31.
In equilibrium groundwater is assumed to flow parallel to the surface. This represents a saturated dike without water outflow. Soil stress (both pore water pressure and effective stress) at the surface is zero. To obtain no outflow, pore water pressure increases linearly along the z-axis, see Equation 3.33. Effective stress increases linearly with the actual depth, which has an angle θ with the z-axis. The effective stress gradient along the z-axis

is given by Equation 3.32. Figure 3.2 shows the differences between the water pressure gradient and the effective stress gradient.

$$\frac{\partial \sigma'}{\partial x} = 0 \qquad at\ t = 0 \tag{3.30}$$

$$\frac{\partial p}{\partial x} = 0 \qquad at\ t = 0 \tag{3.31}$$

$$\frac{\partial \sigma'}{\partial z} = (\rho_s - \rho)g \qquad at\ t = 0 \tag{3.32}$$

$$\frac{\partial p}{\partial z} = \rho g \cos\theta \qquad at\ t = 0 \tag{3.33}$$

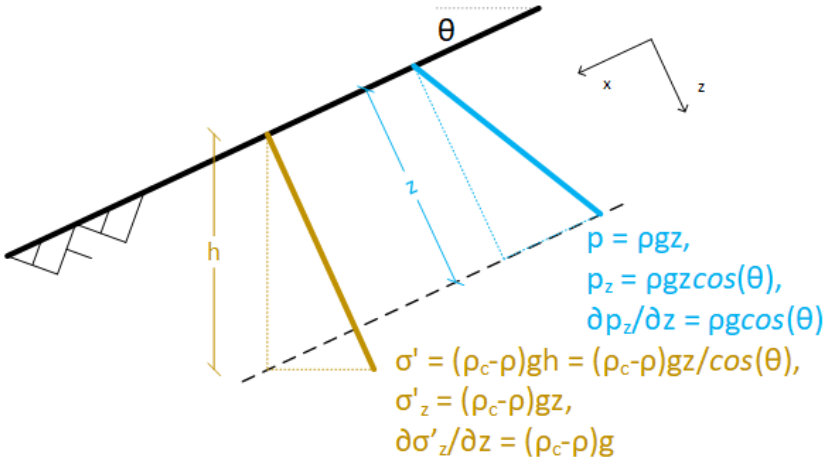

Figure 3.2: Water pressure increase along the z-axis (blue) and effective stress increase along the actual depth (brown).

3.3 Surface boundary conditions

Correct modelling of the surface boundary condition is the hardest problem in the entire model. The surface boundary condition must be able to handle loaded and unloaded situations, also when they occur at the same time at different locations. The configuration of loaded/unloaded locations and the magnitude of the load varies in time. Furthermore, the surface boundary condition must be able to give a correct definition of the increase in pore water pressure and the effective stress w.r.t. the load. Because these ratio's change during a load cycle.

At the soil surface (z=0) a surface boundary condition is set. This boundary condition is a Dirichlet or a Cauchy boundary condition (Cheng and Cheng [2005]), depending on the load situation. At unloaded points on the slope a Dirichlet boundary condition. At loaded points a Cauchy boundary condition is applied, to represent load by both

stress and stress gradient correctly. The spatial distribution of the surface boundary conditions application is shown in Figure 3.3. The figure shows application of different boundary conditions for loaded and unloaded soil. Note that wave propagation causes temporal variation as well. Additionally, Figure 3.4 shows an overview of the all boundary conditions on the model, including the surface boundary condition.

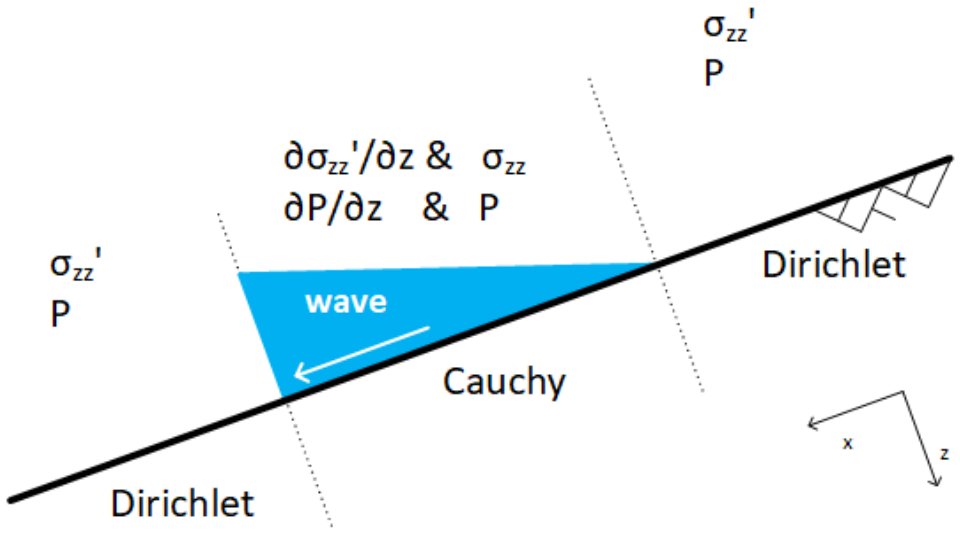

Figure 3.3: Overview of the spatial variable use of Dirichlet and Cauchy boundary conditions on the surface boundary at the locations with and without wave load.

3.3.1 Boundary conditions for different load situations

Four load situations are distinguished: no load, load by normal stress, load by shear stress and load by normal stress and shear stress. When the soil is unloaded a Dirichlet boundary conditions, stating that the water pressure and the effective stress at the surface equal 0 Pa, is applied. When only normal stress load is considered a Dirichlet boundary condition is applied. When only shear stress or both shear and normal stress are considered, a Cauchy boundary condition is applied. The derivation of the stress gradient in the Cauchy boundary condition, based on the equilibrium of a soil element, is explained below.

The impulse balance equations in x- and z-direction (Equations 3.1 and 3.2) are rewritten to Equations 3.34 and 3.35. The forces represented by the terms of these equations are shown in Figure 3.5.

$$\frac{\partial \sigma_{xx}}{\partial x} + \frac{\partial \tau_{zx}}{\partial z} - \gamma sin\theta = 0 \tag{3.34}$$

$$\frac{\partial \tau_{xz}}{\partial x} + \frac{\partial \sigma_{zz}}{\partial z} - \gamma cos\theta = 0 \tag{3.35}$$

Assuming irrotationality of a soil element, perpendicular shear stresses must be equal, see Equation 3.36. This is substituted into Equation 3.35 giving Equation 3.37.

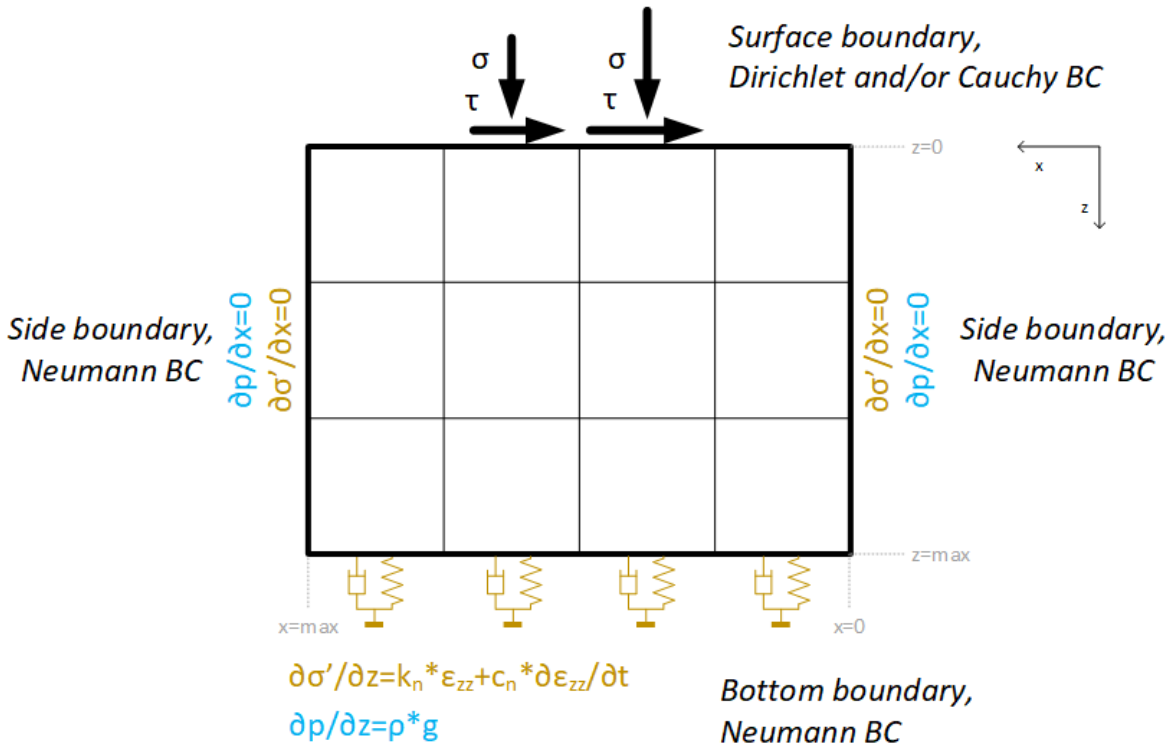

Figure 3.4: Schematic representation of all boundary conditions (BC) on the soil model. The surface BC is explained in Section 3.3, the side BC in Section 3.4 and the bottom BC in Section 3.5. The BC for effective stress are shown in brown and the BC for water pressure are shown in blue. The surface BC for effective stress and water pressure are linked and are variable in configuration. More detail of this BC is given in Figure 3.3.

The total stress equals the sum of the water pressure and the effective stress. The gradients of these stresses are related likewise, transforming Equation 3.37 into Equation 3.38. These equations show that the shear stress gradient in x-direction is inversely proportional related to the effective stress gradient and total stress gradient in z-direction. For a stress state that is conditioned by stress at the surface, which is the case for a Cauchy boundary condition, a positive shear stress gradient causes a pulling force on the soil.

$$\tau_{zx} = \tau_{xz} \tag{3.36}$$

$$\frac{\partial \sigma_{zz}}{\partial z} = -\frac{\partial \tau_{zx}}{\partial x} + \gamma cos\theta \tag{3.37}$$

$$\frac{\partial \sigma'_{zz}}{\partial z} = -\frac{\partial \tau_{zx}}{\partial x} + \gamma cos\theta - \frac{\partial p}{\partial z} \tag{3.38}$$

The ratio between the water pressure and the effective stress is unknown. Moreover, this ratio develops during loading. Their sum, the total stress, is known. Furthermore it is known that a stress increase initially is entirely carried by pore water pressure (van der Grinten [1987], Smeulders [1992]). The determination of the development of

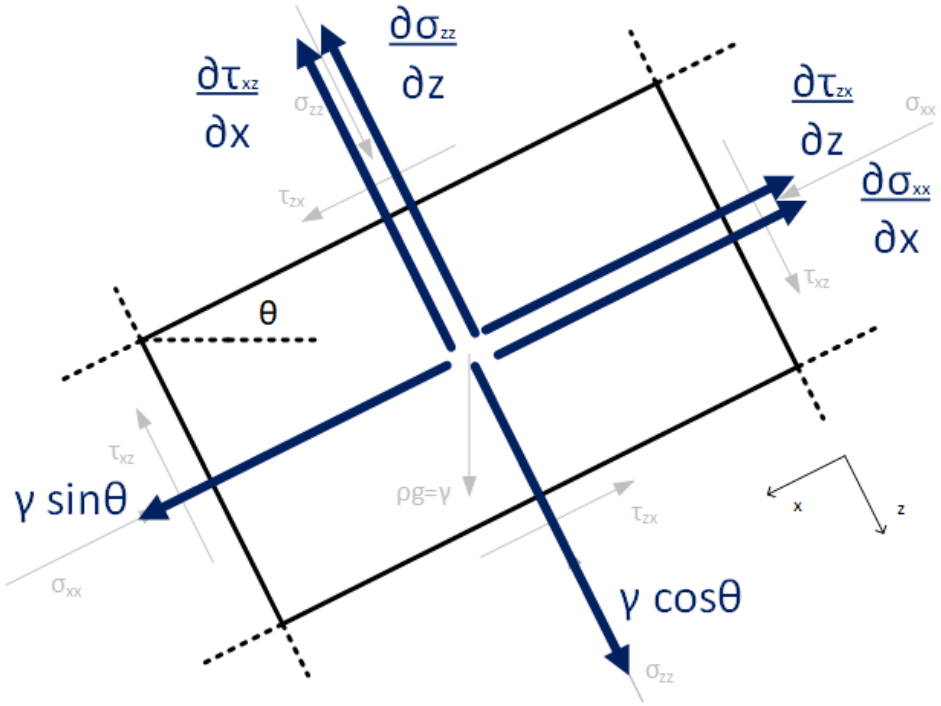

Figure 3.5: Forces originating from stress gradients and gravity, that contribute to the 2D force equilibrium on a soil element. Displayed forces are not to scale.

water pressure and effective stress as a function of the total stress is given in Section 3.3.2.

3.3.2 Ratio soil stress components

To determine the ratio between the effective stress and the water pressure as a function of the total stress at the surface, a relation between the total stress and the effective stress is derived. It is derived from Equations 3.39 and 3.40. These are expressions for the development of strain (van Damme [2018a]) and water pressure (Equation 3.28) in space and time, respectively.

$$\frac{\partial^2 \varepsilon}{\partial x^2} + \frac{\partial^2 \varepsilon}{\partial z^2} = \frac{\gamma_w}{k_s 4(\lambda + \mu)} \frac{\partial \varepsilon}{\partial t} \tag{3.39}$$

$$\frac{\partial^2 p}{\partial x^2} + \frac{\partial^2 p}{\partial z^2} = \frac{\gamma_w}{k_s} \frac{\partial \varepsilon}{\partial t} \tag{3.40}$$

In Equation 3.39, λ and μ denote the 1^{st} and 2^{nd} Lamé parameter respectively. These parameters represent the elasticity of the soil and can be rewritten to an expression for the elasticity in terms of compression modulus K and shear modulus G, as shown in Equations 3.41 (Mavko et al. [2009]).

$$\lambda = K - \frac{1}{3}G, \qquad \mu = G \tag{3.41}$$

Substituting Equations 3.24, 3.23 and 3.41 into Equations 3.39 and 3.40 results in Equations 3.42 and 3.43, respectively. Equation 3.42 relates the effective stress distribution in space to the effective stress development in time. Equation 3.43 relates the water pressure distribution in space to the effective stress development in time.

$$\frac{\partial^2 \sigma_1'}{\partial x^2} + \frac{\partial^2 \sigma_1'}{\partial z^2} = \frac{\gamma_w}{4k_s(K + \frac{2}{3}G)} \frac{\partial \sigma_1'}{\partial t} \tag{3.42}$$

$$\frac{\partial^2 p}{\partial x^2} + \frac{\partial^2 p}{\partial z^2} = \frac{-\gamma_w}{k_s(K + \frac{1}{3}G)} \frac{\partial \sigma_1'}{\partial t} \tag{3.43}$$

The sum of Equations 3.42 and 3.43 is Equation 3.44, giving the relation between the total stress distribution in space and the effective stress development in time. The total stresses at the surface are known, so the derivative in x-direction is known as well. If Equation 3.44 is solved explicitly (based on values at previous time step) the derivative in the z-direction is known as well. Then the effective stress gradient is the only unknown. Equation 3.44 is applied to determine the portion of the total stress that acts on the effective stress. From these stresses follows the portion that acts on the water pressure.

$$\frac{\partial^2 \sigma}{\partial x^2} + \frac{\partial^2 \sigma}{\partial z^2} = \Big(\frac{\gamma_w}{4k_s(K + \frac{2}{3}G)} + \frac{-\gamma_w}{k_s(K + \frac{1}{3}G)} \Big) \frac{\partial \sigma_1'}{\partial t} \tag{3.44}$$

Executing model runs shows that this approach gives realistic results for cases with Dirichlet surface boundary conditions (that is a normal stress) only. For cases with a Cauchy surface boundary condition, considering both normal stress at the surface and stress gradient through the surface, it gives non-realistic results. To be able to run such cases an approximation on the stress development is drafted, see Section 3.3.3.

3.3.3 Theoretical approximation on stress development

The development of water pressure in time in a loaded soil is approached with a Laplace transform method (Verruijt [2008], Churchill [1972]) resulting in the exponential functions given by Equation 3.45. Here p denotes the water pressure, t the time and s a positive parameter that determines the shape of the function.

$$\frac{dp}{dt} = -se^{-st}, \qquad p = e^{-st} \tag{3.45}$$

Equation 3.45 describes only the shape of the function giving the development of water pressure. The actual water pressure starts at the initial water pressure and develops to an equilibrium value, which is zero for the surface load. The initial value, denoted by $\Delta\sigma$, is the difference between the governing water pressure and the equilibrium value. It equals the sum of the total stress increase and the exponential decrease. The effective stress development follows from the water pressure development and the total stress development.
The exponential function is based on a constant load and is therefore adjusted to suit

a variable load. For a variable load the value of σ must be updated every time step, automatically updating $\Delta\sigma$ as well. Additionally, the change in total stress is added on the water pressure. After this update the exponential decrease of the water pressure and increase of the effective stress starts again.
A second adjustment is the correctional load factor f_{load} is added. This factor equals varying load integrated over time divided by the load at previous time step (a constant value) integrated over one time step, see Equation 3.46 and Figure 3.46. Consequently it is a measure for the actual accumulated load during a time step, with respect to the accumulated load during that time step if the load would be constant. Here t denotes the time, σ denotes the total stress which is the load and the subscripts t and $t-1$ indicate current and previous time step respectively.

$$f_{load} = \frac{\int_{t-1}^{t} \sigma_t dt}{\int_{t-1}^{t} \sigma_{t-1} dt} \tag{3.46}$$

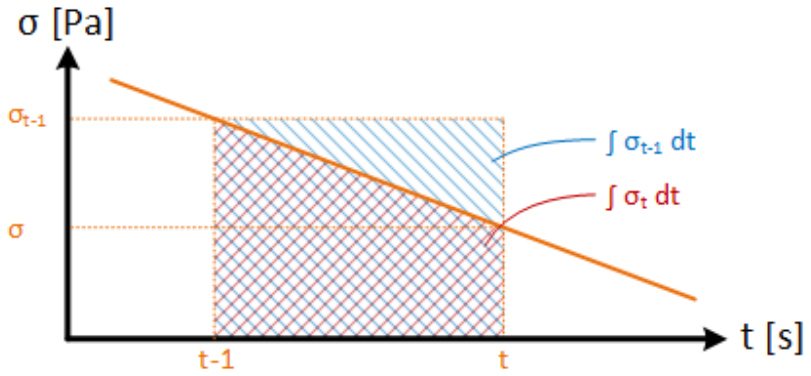

Figure 3.6: Origin of the numerator and denominator in the definition of f_{load} (Equation 3.46).

Applying the exponential development function (Equation 3.45) with the load decrease factor and considering the stress update during load increase, Equations 3.47 and 3.48 are drafted. The development of the water pressure is given by Equation 3.47. The development of the water pressure is given by Equation 3.48.

$$p = \sigma - \Delta\sigma f_{load} e^{-st} \tag{3.47}$$

$$\sigma' = \Delta\sigma f_{load} e^{-st} \tag{3.48}$$

Based on the model runs with Dirichlet boundary conditions the value of s is determined. Figure 3.7 shows the effective stress development resulting from a such a run and an approach of the effective stress development with the exponential function in Equation 3.45. From this comparison it results that $s \approx 6.4 * 10^{-4}$.
Figure 3.7 shows that the modelled effective stress and the effective stress derived from the theoretical approximation, develop accordingly. This indicates that the stresses resulting from modelling are reasonable. Furthermore, it shows that the exponential function slightly overestimates effective stresses in the first phase of load. In the subsequent

phase it underestimates the effective stresses. The development of water pressure is the inverse of that of effective stress.

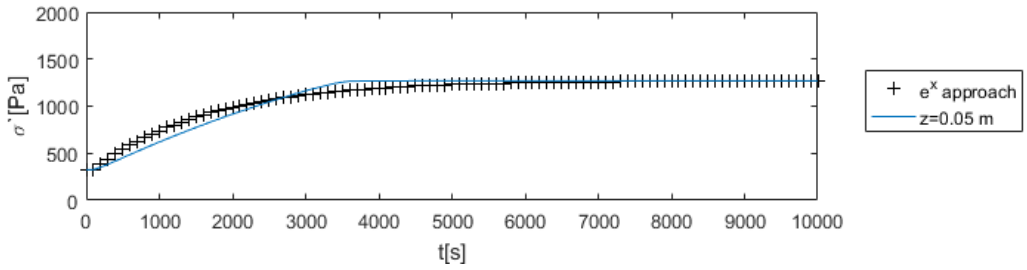

Figure 3.7: Effective stress development in the soil resulting from a model with Dirichlet surface boundary conditions and an approach of this development with the exponential function derived from theory (Equation 3.48) with $s = 6.4 * 10^{-4}$.

For validation of the theoretical approximation on the load a comparison is made between the resulting soil stresses from model runs with a Dirichlet surface boundary condition and with a Cauchy surface boundary condition with theoretical approximation. This comparison is shown in Figure 3.8. The comparison is done for a case with a normal stress load of 1000 Pa during the first 500 seconds and 0 Pa during the subsequent 500 seconds. It shows that the theoretical approximation on the load approximates the results of the model without the approximation. It gives an underestimation of the speed of adaptation of effective stress and water pressure, at the start of load decrease (approx between 500 and 600 s) .

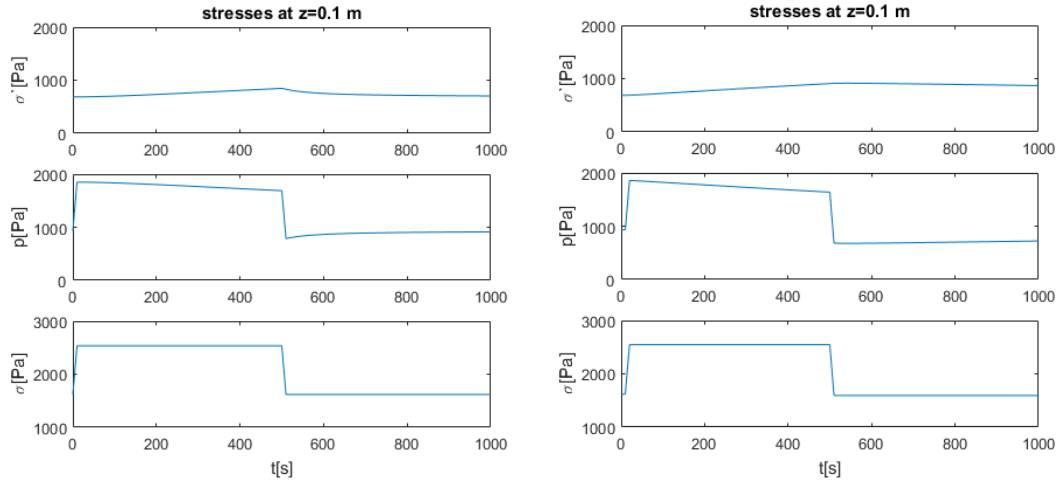

(a) Dirichlet, without theoretical approximation.

(b) Cauchy, with theoretical approximation.

Figure 3.8: Resulting effective stresses, water pressures and total stresses from model runs with application of different boundary conditions.

3.4 Side boundary conditions

At the sides of the model ($x = x_{min}$ and $x = x_{max}$), a side boundary condition is set. This boundary condition is a Neumann boundary condition (Cheng and Cheng [2005]). The application of boundary conditions is shown in Figure 3.4.
The side boundaries represent the soil at a section normal to the slope at a random location. These boundaries must be permeable for soil stresses, without influencing the stress development inside the model. Therefore, the effective stress and the water pressure at the boundary is set to get the same value as the effective stress and the water pressure in the soil adjacent to it, see Equations 3.49 and 3.50.

$$\frac{\partial \sigma'}{\partial x} = 0 \tag{3.49}$$

$$\frac{\partial p}{\partial x} = 0 \tag{3.50}$$

The side boundary conditions can have a small reflective influence on the soil stress propagation. To eliminate the effect of this, the model is nested. At both sides of the model nesting cells are added, as shown in Figure 3.9. The dimensions of the nesting cells equal that of the model cells. The boundary conditions are applied on the outer boundaries of the nested model. The nesting cells are considered in computation, but not in output generation. Consequently, no potentially influencing conditions are set on the side boundaries of the model cell domain. The width of the nest is adjustable to the range of appearing boundary influences.

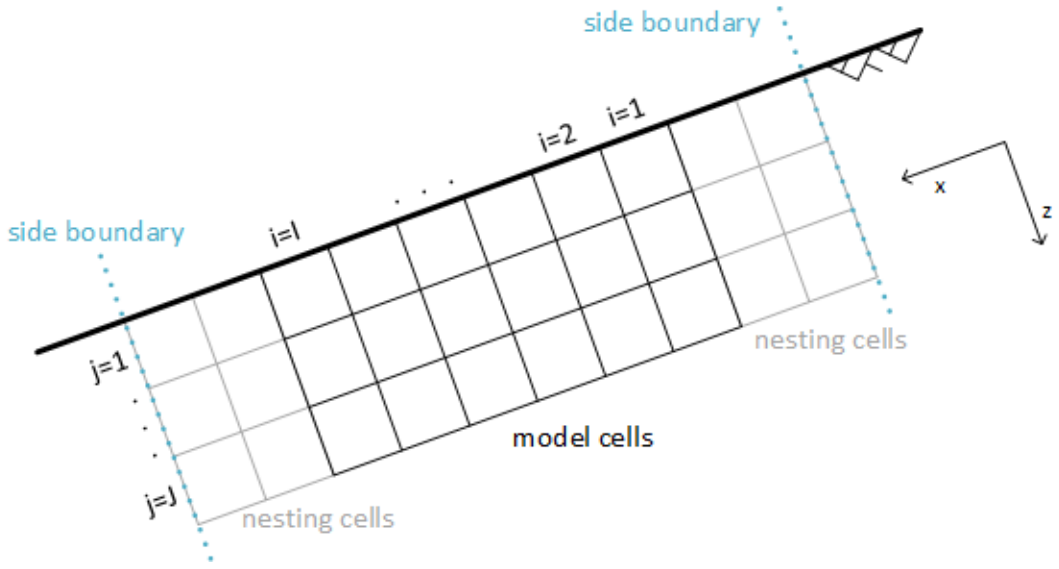

Figure 3.9: Model nesting as applied.

3.5 Bottom boundary conditions

At the bottom of the clay layer ($z = z_{max}$) a bottom boundary condition is set. This boundary condition is a Neumann boundary condition (Cheng and Cheng [2005]). The application of boundary conditions is shown in Figure 3.4.
The bottom boundary represents the interface between the clay layer and the sublayer. Assuming that the sublayer is made of sand, the sublayer stiffness has a larger, finite value than the clay layer stiffness ($E_{sand} > E_{clay}$), causing damping at the bottom. A Kelvin-Voigt boundary is used to model this boundary, see Section 2.5.2. According to Tan [2016] the force at the absorbing boundary is given by Equation 3.51. S is the area of the absorbing boundary, N^T is the transposed shape function and σ_{bot} is the bottom boundary stress.

$$F_{vb} = \int_S N^T \sigma_{bot} dS \tag{3.51}$$

N^T is the shape function giving the interpolation of values in between points of calculation, the nodes in a discretized soil grid (Egger [2015]). Only the nodes of calculation are considered, where the shape function equals 1.
The bottom boundary stress consists of spring traction (σ_{spring}) and dashpot traction ($\sigma_{dashpot}$). Spring traction is the product of the spring coefficient (k_n) and the displacement (u). Dashpot traction is the product of the dashpot coefficient (c_n) and the displacement velocity ($\dot{u} = \frac{\partial u}{\partial t}$). The relation giving the bottom boundary stress (σ_{bot}) is shown in Equation 3.52.

$$\sigma_{bot} = \sigma_{spring} + \sigma_{dashpot} = k_n u + c_n \dot{u} \tag{3.52}$$

The spring and dashpot coefficients are given by Equation 3.53 and 3.54 respectively. E_c is the constrained Young's modulus which is a function of Young's modulus and Poisson's coefficient, see Equation 3.55. Furthermore, ρ is the soil density. The coefficient δ denotes the virtual thickness of the layer that is modelled as a spring. It is assumed that the sublayer is of such thickness that it is the only layer of influence at the bottom boundary. It is modelled that $\delta = 10m$. Coefficient α_n is a factor giving the magnitude of the dashpot effect. For $\alpha_n = 0$ the boundary acts like a spring only and for $\alpha_n = \infty$ the boundary acts rigid. Tan [2016] uses values of approximately $\alpha_n = 1$ for an absorbing bottom boundary.

$$k_n = \frac{E_c}{\delta} \tag{3.53}$$

$$c_n = \alpha_n \sqrt{E_c \rho_s} \tag{3.54}$$

$$E_c = \frac{(1-\nu)E}{(1-2\nu)(1+\nu)} \tag{3.55}$$

The stiffness of the bottom boundary depends on the displacement, which is unknown. The spatial derivative of the displacement normal to the boundary is known as a function of the strain (Equation 3.24). This is applied in Equation 3.56. The strain is a function of the effective major principle stress (Equations 3.23).

$$\frac{\partial \sigma_{bot}}{\partial z} = k_n \varepsilon_{zz} + c_n \frac{\partial \varepsilon_{zz}}{\partial t} \tag{3.56}$$

For the water pressure at the bottom boundary a Neumann boundary condition is applied. Due to incompressibility water adapts immediately to stress increase, without any damping. The only spatial variation in stresses is caused by its own weight. The stress gradient is therefor equal to that in unloaded state. This gives Equation 3.57 as a boundary condition.

$$\frac{\partial p}{\partial z} = \rho g \tag{3.57}$$

3.6 Discretization

3.6.1 Discrete model dimensions

The model gives the development of stresses in discrete steps in space and time. The model consists of a rectangular spatial grid on each time step, as shown in Figure 3.10. Default spatial grid dimensions are given in Table 3.1.

Table 3.1: Default spatial model dimensions.

model dimension	cell size	number of cells	total length dimension
parallel to slope	dx = 0.05 m	I = 100	x = 5.00 m
normal to slope	dz = 0.05 m	J = 10	z = 0.50 m

3.6.2 Effective stress

The effective soil stress is computed with Equation 3.29. This is a diffusion equation with the form of Equation 3.58.

$$-\frac{\partial^2 \sigma'}{\partial x^2} - \frac{\partial^2 \sigma'}{\partial z^2} + \frac{\partial \sigma'}{\partial t} = 0 \tag{3.58}$$

Equation 3.58 is discretized with a *Theta-Central scheme*, with $\theta = 1$, which is a combination of the *Central scheme* for space integration and the *Implicit Euler scheme* for time integration (Zijlema [2015]). This scheme is unconditionally stable. As a measure of accuracy the truncation error is $\tau_{\Delta t \Delta x \Delta z} = O(\Delta t, \Delta x^2, \Delta z^2)$. Figure 3.11 shows the dependencies of a computation point with adjacent points in space and time. The discretized equation is given by Equation 3.59.

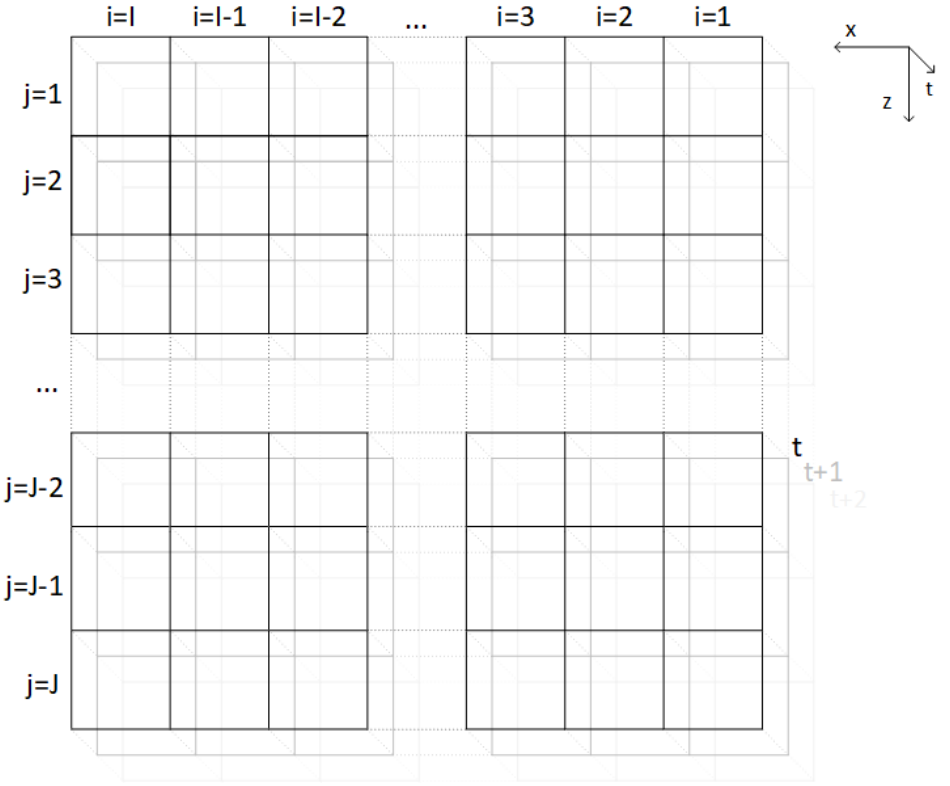

Figure 3.10: A 3 dimensional discrete model grid with a width of I cells and a depth of J cells on each time step t.

$$\frac{-\sigma'^{n+1}_{i-1,j} + 2\sigma'^{n+1}_{i,j} - \sigma'^{n+1}_{i+1,j}}{\Delta x^2} + \frac{-\sigma'^{n+1}_{i,j-1} + 2\sigma'^{n+1}_{i,j} - \sigma'^{n+1}_{i,j+1}}{\Delta z^2} + \frac{\sigma'^{n+1}_{i,j} - \sigma'^{n}_{i,j}}{\Delta t} = 0 \qquad (3.59)$$

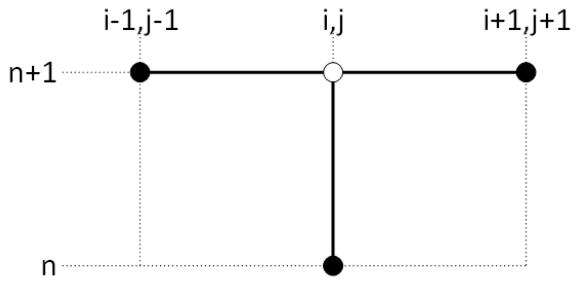

Figure 3.11: Stencil of the Theta-Central scheme with $\theta = 1$. In horizontal direction integration steps in space (i,j) and in vertical direction integration steps in time (n) are shown. The white dot is the computed value $\sigma'^{n+1}_{i,j}$.

3.6.3 Water pressure

A relation between the water pressure and the strain (Equation 3.28) is used to compute the water pressure. This relation is a diffusion equation of the form of Equation 3.60.

Water pressure is related to the previous time step by the strain gradient in time ($\frac{\partial \varepsilon}{\partial t}$), which is known. The equation applies on the same grid as the effective stress, presented in Table 3.1 and Figure 3.10.

$$-\frac{\partial^2 p}{\partial x^2} - \frac{\partial^2 p}{\partial z^2} = \frac{\partial \varepsilon}{\partial t} \tag{3.60}$$

Equation 3.60 is discretized with a *Central scheme* for space integration. As a measure of accuracy the truncation error is $\tau_{\Delta x \Delta z} = O(\Delta x^2, \Delta z^2)$. Figure 3.12 shows the dependencies of a computation point with adjacent points in space. The discretized equation is given by Equation 3.61. Note that the strain gradient is known and therefor not discretized.

$$\frac{-p_{i-1,j} + 2p_{i,j} - p_{i+1,j}}{\Delta x^2} + \frac{-p_{i,j-1} + 2p_{i,j} - p_{i,j+1}}{\Delta z^2} = \frac{\partial \varepsilon}{\partial t} \tag{3.61}$$

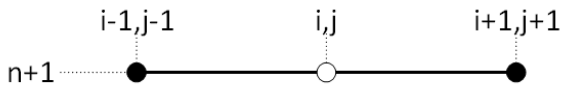

Figure 3.12: Stencil of the Central scheme. In horizontal direction integration steps in space (i,j) are shown. The white dot is the computed value $p_{i,j}^{n+1}$.

3.6.4 Surface boundary condition

The ratio between the effective stress and the water pressure as a function of the total stress at the surface boundary is computed with Equation 3.44. This is a diffusion equation of the form of Equation 3.62.

$$-\frac{\partial^2 \sigma}{\partial x^2} - \frac{\partial^2 \sigma}{\partial z^2} = \frac{\partial \sigma'}{\partial t} \tag{3.62}$$

Equation 3.62 is discretized with the explicit *FTCS scheme* (Zijlema [2015]). (FTCS means *Forward in Time, Central in Space.*) As a measure of accuracy the truncation error is $\tau_{\Delta t \Delta x \Delta z} = O(\Delta t, \Delta x^2, \Delta z^2)$. Figure 3.13 shows the dependencies of a computation point with adjacent points in space and time. The discretized equation is given by Equation 3.63.

$$\frac{\sigma'^{n+1}_{i,j}}{\Delta t} = \frac{\sigma'^{n}_{i,j}}{\Delta t} - \frac{-\sigma^n_{i-1,j} + 2\sigma^n_{i,j} - \sigma^n_{i+1,j}}{\Delta x^2} - \frac{-\sigma^n_{i,j-1} + 2\sigma^n_{i,j} - \sigma^n_{i,j+1}}{\Delta z^2} \tag{3.63}$$

3.7 Overtopping load computation

Load computation is based incoming wave characteristics and dike geometry, in accordance with Section 2.3. This includes dynamic loading as a measure of the turbulent

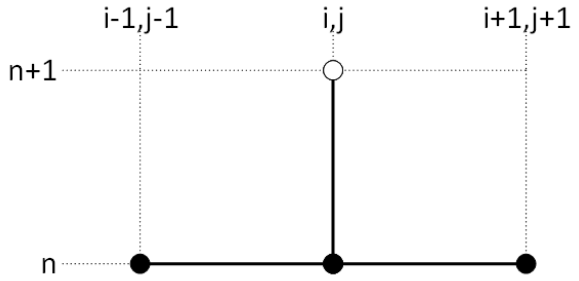

Figure 3.13: Stencil of the FTCS scheme. In horizontal direction integration steps in space (i,j) and in vertical direction integration steps in time (n) are shown. The white dot is the computed value $\sigma'^{n+1}_{i,j}$.

load. Required input for this is obtained in accordance with Section 2.2. The computation input values and their origin are given in this section. The resulting loads are presented in Section 4.3.

Multiple overtopping cases can be considered by changing one or more input parameters. Used values of parameters are based on the *CLASH database* (Steendam et al. [2004], Verhaeghe [2005]). In this research only a default case is considered, shown in Table 3.2. Incoming waves are represented by wave height H_{m0} and wave period $T_{m-1,0}$, both values at the outer toe of the dike. The dike geometry is represented by crest height R_c, slope angle $cot\theta$ and crest width x_c. For the computations a slope length of 10 m is considered. Negative values of the slope angle in CLASH neglected. The maximum considered slope angle of $cot\theta = 1.7$ is based on a case where wave separation was observed (Ponsioen et al. [2017]).
Some combinations of values give non-existing situations during computations, e.g. negative distances. If so, parameter values deviating from CLASH are used. Possible existence of a correlation between different variables is ignored.

Additionally a number of coefficients, given in Table 3.3, is used. The coefficient values are based on van der Meer et al. [2016]. Wave impact reducting elements are considered to be of no reducing influence, considering the maximum wave impact for the prevailing conditions: $\gamma_b, \gamma_f, \gamma_\beta = 0$. The coefficients describing flow characteristics on the dike crest, given by c, have a value corresponding with an outer slope angle of $cot\theta = 5$.

To describe spatial distribution of the wave characteristics the temporal distribution of Hughes [2011] (see Section 2.2.3) is applied. Because of the number of unknowns, an approximation is used. The total wave duration depends on the average wave velocity which, considering a linear decreasing wave velocity (see Section 2.2), is approached by half the maximum wave velocity. The development of the wave height and velocity in time, for the entire wave is based on the wave front velocity in stead of the actual velocity of each point of the wave. Then the passing time (t) equals the distance over the velocity (x/u_{max}), which gives a spatial distribution. This is applied in the formulae from Section 4.3. For instance, Equation 2.9 turns into Equation 3.64. The approximation steepens the tail of the wave and so shortens the modelled wave with respect to the reality. Since the front of the wave in particular is interesting in overtopping, the assumption is considered suitable.

Table 3.2: Values of parameters used for indicative load computations, based on CLASH.

Symbol	Unit	Explanation	Default value
H_{m0}	m	Significant wave height	1.0
$T_{m-1,0}$	s	Mean wave period	4.0
R_c	m	Crest freeboard	1.0
$cot\theta$	-	Slope angle	3.0
x_c	m	Crest width	0.3
q	$m^3/s/m$	Overtopping discharge	0.1

Table 3.3: Values of non-variable coefficients used for indicative load computations.

Symbol	Explanation	Value
γ_b	Coefficient for influence of a berm	1.0
γ_f	Coefficient for influence of slope roughness	1.0
γ_β	Coefficient for influence of oblique wave attack	1.0
$c_{h,2\%}$	Coefficient for flow thickness at the crest	0.25
$c_{v,2\%}$	Coefficient for flow velocity at the crest	1.47

$$h(t) = h_{max}(1 - \frac{(\frac{x}{u_{max}})}{T_0})^a \tag{3.64}$$

3.8 Model assumptions

In model derivations assumptions are made. Some of them are the assumption about principles (or sometimes facts) that are valid, see Section 3.8.1. Others are about default values for specific model parameters, see Section 3.8.2.

3.8.1 Principles

Assumptions, made for model development, are listed below. These assumptions influence the applicability of the model and frame the possibilities for further model development.

The first list gives assumptions that are fundamental for this way of modelling and are therefor considered to be unchangeable.

- *The dike cover layer consists of clay.* The assumption to focus on one soil type is made because of the differences in the action of forces in different soil types. Clay is chosen because it is much used dike cover material. This assumption underlies other assumptions;
- *The density of soil particles (ρ_s) and of water (ρ) is spatial invariable.* This assumptions enables neglecting terms in model derivation (Section 3.1.2), so it simplifies model equations;

- *The cohesion of clay in the model is constant in space and time.* This assumptions enables neglecting terms in model derivation (Section 3.1.3), so it simplifies model equations;
- *The saturation of the soil is such that the angle of repose of clay is small.* This assumptions enables neglecting terms in model derivation (Section 3.1.3), so it simplifies model equations and reduces required knowledge of soil characteristics;
- *A soil element in the dike cover is irrotational.* This assumption to link shear stress in perpendicular directions to each other and subsequently to link the shear stress gradient to the normal stress gradient in perpendicular direction (Section 3.3.1). This is used to apply the shear stress on the model in which the calculations are based on principle stresses, which are normal stresses.

The second list gives assumptions done to reduce the workload to a reasonable amount within the frame of this thesis. These assumptions can easily be changed during further development of the model.

- *Ground water flows parallel to the soil surface.* This assumption is based on an entirely saturated dike in, which is an approach for a dike during storm conditions, under overtopping load (Sections 3.2, 3.4 and 3.5). It enables to write simple equations on spatial variation of the hydrostatic pore water pressure.
- *Soil stress development in time under a variable overtopping load, can be approached by an exponential function.* This assumption is based on the approach of the soil stress development under a constant load. It is applied for a variable load with matching adjustments (Section 3.3.3). This assumption is made to overcome a deadlock in modelling the surface boundary conditions such that the model generates realistic results;
- *Load by wave impact and load by a flowing wave, both having a shear and normal stress component, both occur in one overtopping wave cycle* This assumption is based on the lack of support for excluding one of the load mechanisms from the total load (Section 3.7). It is chosen to use one load case because comparison of load cases is not the focus of this research;
- *The spatial distribution of an overtopping wave is related to the flow velocity of the wave front instead of the local velocity.* This assumption is made to enables to determine the distribution of wave thickness and velocity within one overtopping wave, with the minimal number of known wave characteristics (3.7). It steepens and shortens in particular the tail of the wave, which is of lesser interest.

3.8.2 Parameter values

A number parameters, describing a soil characteristic, are used. Some of them have a value in a large range, but are assigned a value that is representative for this case. These values are given in Table 3.4. For background information on the parameters, see Sections 2.5 and 3.5.

Table 3.4: Default parameter values for soil pressure modelling.

Symbol	**Unit**	**Explanation**	**Value**
E	MPa	Young's modulus	10
k_s	m/s	Hydraulic conductivity	$1.0E^{-7}$
α_n	-	Dashpot effect factor	1
δ	m	Virtual sublayer thickness	10
ν	-	Poisson's ratio	0.4
ρ	kN/m^3	Water density	1000
ρ_s	kN/m^3	Clay density	1700

4 Results

In the previous chapter a soil stress model is described. In Section 4.1, in a brief recap, the model is presented. Subsequently, the model is used for different load cases and the results are analyzed for qualitative verification of the model. These cases are simple and comparisons with results are obtained in various ways. Verification is reported in Section 4.2. Finally, the model is fully applied on overtopping. The effect of a single overtopping wave running over the dike slope is computed. This is reported in Section 4.3.

4.1 Soil stress model

This section describes the developed soil stress model. Section 4.1.1 describes the current version of the model. Section 4.1.2 describes and explains development approaches that have not lead to result. These are useful to be taken notice of in further development.

4.1.1 Current model

A 2D soil stress model is developed. It computes the soil stress response, in space and time, on a load on the surface. The model is developed to compute soil stresses during wave overtopping events. Model development consisted of theoretical derivation and numerical programming.
The model dimensions are variable (see Table 4.1). The total modelled length of two spatial dimensions can be set, as well as the total timespan. Furthermore, the grid size of the model in two dimensions and the time steps can be set as well.

The model computes soil stresses for an load defined as a normal stress, shear stress or a combination of both. The model functions for a load that is constant or variable in time and for a load that has a positive or a negative value. There are three different load

Table 4.1: Changeable variables in the soil stress model. Sections from top to bottom contain variables considering the following characteristics: numerical, geotechnical, geometrical and hydrodynamical characteristics.

Symbol	Explanation
I	Number of model cells in x-direction
J	Number of model cells in z-direction
t_n	Number time steps
dx	Length of a cell in z-direction
dz	Length of a cell in z-direction
dt	Length of a time step
f_{nest}	Nesting width factor
E	Young's modulus
k_s	Hydraulic conductivity
n	Manning's roughness coefficient
α_n	Dashpot effect factor
δ	Virtual sublayer thickness for damping
ρ_s	Soil density
ν	Poisson's ratio
R_c	Freeboard
x_c	Width crest
θ	Dike slope
θ_{sea}	Dike slope at water side
$c_{h,2\%}$	Coefficient for flow thickness at crest
$c_{v,2\%}$	Coefficient for flow velocity at crest
H_{m0}	Incoming wave heigth
q	Overtopping discharge
$T_{m1,0}$	Incoming wave period
α_τ	Turbulence coefficient
γ_b	Coefficient for berm influence
γ_f	Coefficient for slope roughness influence
γ_β	Coefficient for wave attack obliqueness influence
η_a	Air concentration

modes included, with necessary supporting functions, to write input load files.
The three load modes are *manual*, *manual wave* and *waveload*. In the mode *manual* the load must be defined manually. This is suited for simple load cases, like a constant load on a specific area. In the mode *manual wave* a wave load is defined by assigning values to specific wave characteristics. This is suited to make calculations matching overtopping measurements. In the mode *wave load* a wave load is defined by assigning values to a characteristics of the incoming wave conditions and the dike geometry.
Based on the variable input load and predefined stress relations and boundary conditions the soil stresses are computed. A distinction is made between the total stress, effective stress and water pressure. The model does not compute fully saturated conditions but it describes the development of stress components from an initial saturated situation to a new (not saturated) equilibrium.
The results of the computation are presented numerically and graphically. The graphical

representation is optional and can be switched on and off. The numerical representation are 3D matrices with the values of the results. The graphical representation consists of animations showing the development of stresses during the model run and 2D plots showing, among others, stress development in time, stress distribution in depth, stress distribution along the surface and plots of stress gradients.
The model has a number of variables, see Table 4.1. Some of the variables, mostly the ones concerning geotechnical characteristics, are in the main part of the model. Others are in supporting functions. All variables have predefined values, representative for the case of an overtopping wave load on a dike with a cover layer.

4.1.2 Approaches on modelling the surface boundary condition

In an attempt to model the surface boundary conditions correct, several approaches have been applied which eventually turned out to give incorrect results. These approaches and the resulting flaws are explained below and a brief overview is given in Table 4.2. The knowledge that these approaches are defective is useful in further development. The approach that used in the final model is explained in Section 3.3.2 and is not discussed in this section.

Table 4.2: Overview of applied defective approaches on modelling of the surface boundary condition and corresponding flaws in the results.

Approach	**Flaw**
Dirichlet surface boundary condition only	Excessive numerical stability
Neumann surface boundary condition only	Numerical instability
Iteration between σ' and p	Numerical instability

It is tried to impose a Neumann or Dirichlet surface boundary condition only, instead of a combination of both or a more complex Cauchy boundary condition. Imposing a Dirichlet boundary condition only is done by calculating an imposed stress at the surface from the soil stress near the surface at the previous time step and the stress gradient at the surface. This led to excessive stability, resulting in no development of soil stresses between time steps, after initial response to load.
Imposing a Neumann boundary condition only is done by rewriting stress at the surface as a stress gradient, using the difference between soil stress at previous time step and the imposed stress at the considered time step. To prevent from values going to infinity, one of the outer nested cells at the surface had a predetermined value, based on the surface load. This approach led to instability, resulting in unrealistic soil stresses, even exceeding imposed load.

Since the load on the surface equals the total stress and the ratio of the stress components develops during loading, it is necessary to find the ratio between the effective stress and the pore water pressure on each time step. It is tried to do this iteratively. The iteration starts from an assumed ratio between those values. Each iteration step the effective stress, the total stress and the pore water pressure are updated, based on previous values of the other two. Application of this iteration led to instability, resulting in unrealistic soil stresses, even exceeding imposed load.

4.2 Qualitative verification

To verify the representation of the soil stresses a number of simple, steady state load cases is computed. These cases are shown in Figure 4.1. The figure shows the normal stresses and the shear stress gradients that are applied as a surface boundary condition. Both stresses are applied on the pore water initially. During a load case they increasingly apply on the soil particles and decreasingly on the pore water pressure, as is described in Section3.3.2. The cases are reported in Sections 4.2.1, 4.2.2 and 4.2.3. Furthermore a comparison is made with the results from pressure measurements during overtopping simulations, see Section 4.2.4. An additional verification run is done with other software. This led just to conclusions that are not relevant for verification. This is presented in Appendix E.

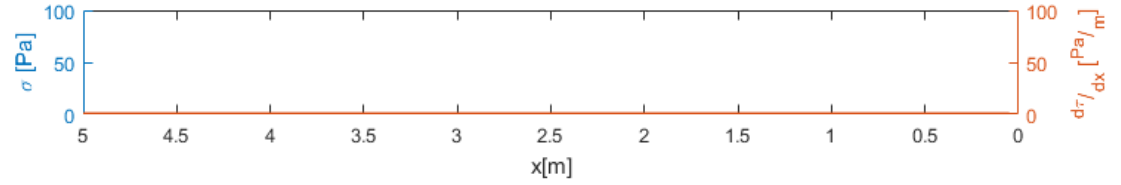

(a) Unloaded.

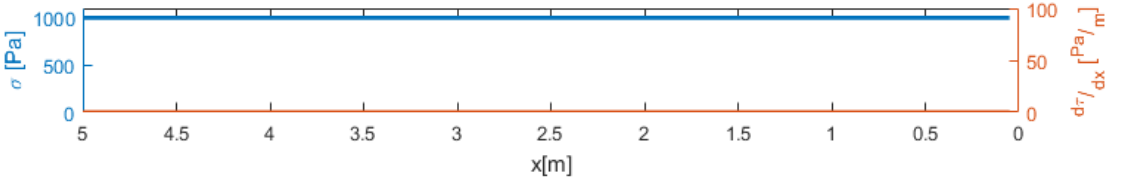

(b) Normal stress of $\sigma = 1000Pa$.

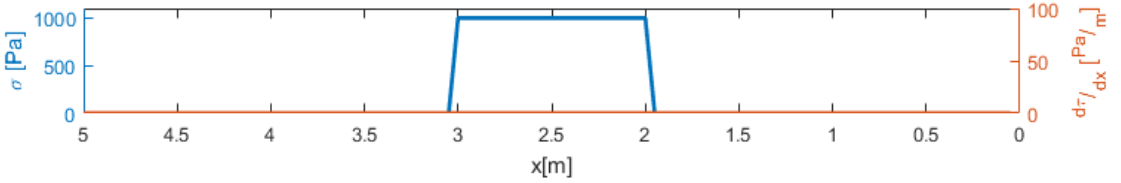

(c) Local normal stress of $\sigma = 1000Pa$.

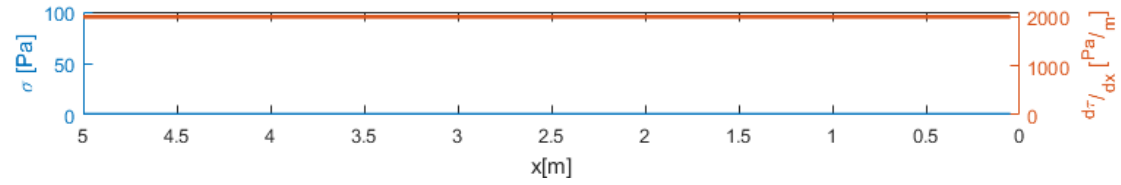

(d) Shear stress gradient of $\frac{\partial \tau}{\partial z} = 100Pa/cell = 2000Pa/m$.

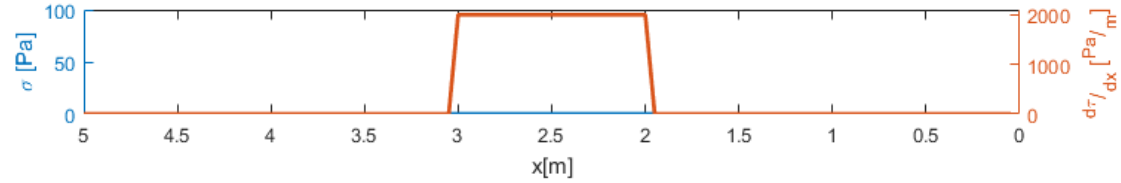

(e) Local shear stress gradient of $\frac{\partial \tau}{\partial z} = 100Pa/cell = 2000Pa/m$.

Figure 4.1: Computed simple load cases.

The initial situation of the model represents an unloaded soil. The only force acting on the soil is the gravitational force, balanced by the prevailing soil pressure. Consequently, effective stress and pore water pressure increase linearly with slope normal depth. Figure 4.2 shows the initial stress distribution of the effective stress and the pore water pressure respectively. The linearity of the stress increase and the matching the soil stresses in unloaded equilibrium and initial situation is clearly shown in Figure 4.4a.

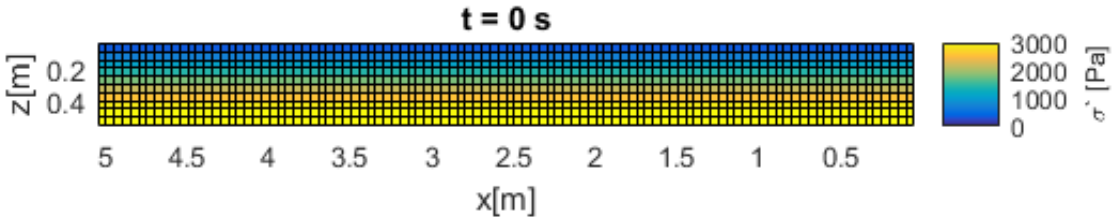

(a) Effective stress.

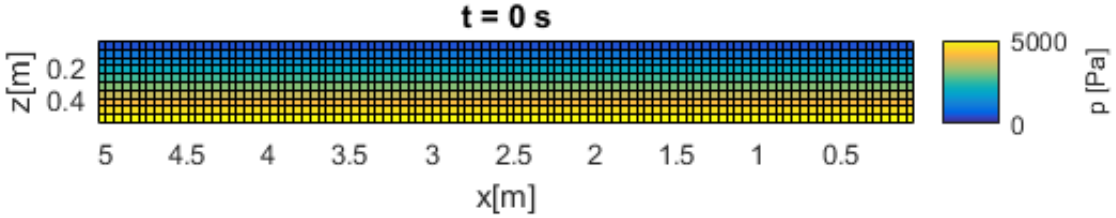

(b) Pore water pressure.

Figure 4.2: Initial stress distribution, showing a linear slope normal stress increase.

4.2.1 Unloaded slope

A model case without load was run, see Figure 4.1a. Here, the initial stress distribution must remain constant an alike initial conditions. Figure 4.3 shows the change in effective stress and water pressure respectively, with respect to the initial situation (given in Figure 4.2), which is zero. Figure 4.4 shows the stress distribution in depth, for the initial situation and after a model run. These figures show that the stress distribution at the start and the end of the model run is similar.

4.2.2 Slope loaded by homogeneous normal stress

A test case concerns a homogeneous load, being a normal stress of $\sigma = 1000Pa$ on the entire model surface, see Figure 4.1b. Figure 4.5, shows the development in time of computed total stress, effective stress and pore water pressure in the soil, at different depths. A similar model case, with normal stress changed to $\sigma = -1000Pa$ (a pulling force) was run. According to expectation, the stress develops inversely w.r.t. the case with pushing load.

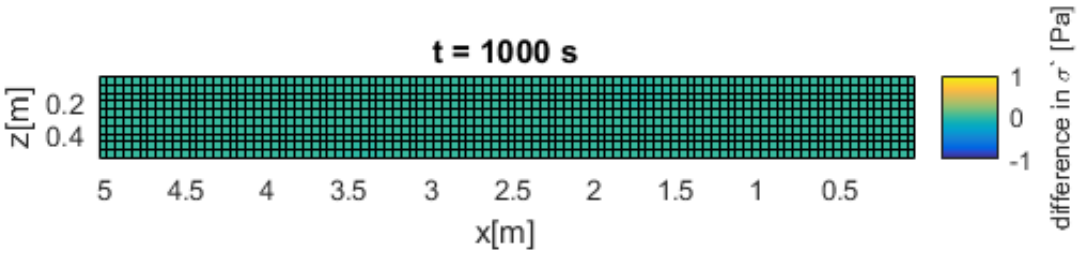

(a) Effective stress.

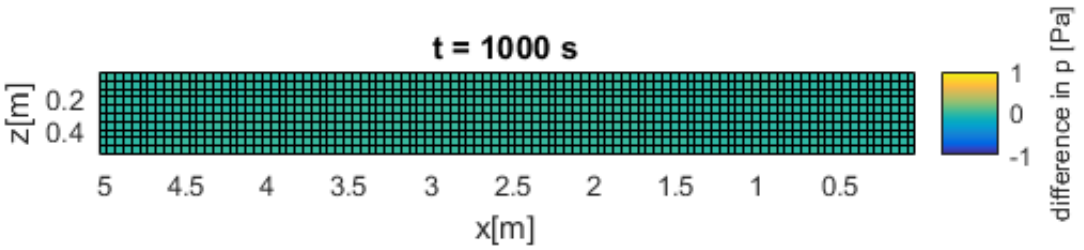

(b) Pore water pressure.

Figure 4.3: Value of the soil stress, relative to the initial stress state, after 1000 seconds of zero load.

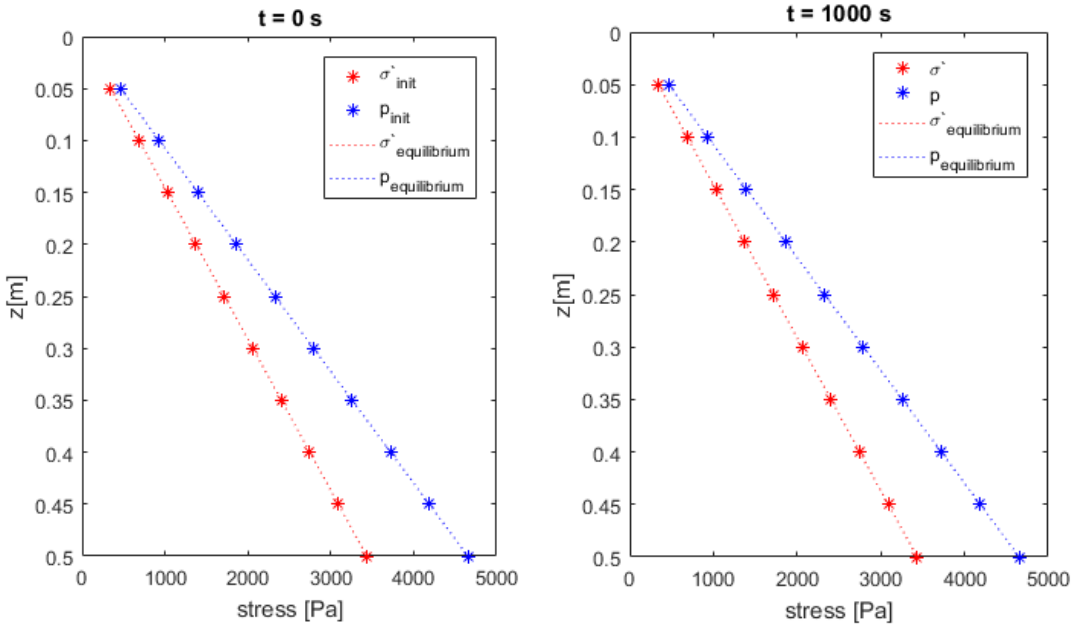

(a) Initial stress distribution. *(b) Resulting stress distribution.*

Figure 4.4: Comparison of the slope normal stress distribution of a soil in unloaded equilibrium with the initial slope normal stress distribution in the model and the slope normal stress distribution resulting from a model run.

Figure 4.5 shows the immediate response of the water pressure and the total stress to surface load. It shows that the effective stress does not respond and the pore water pressure immediately fully carries the surface load.
This behaviour can be explained with the combination of the load on the entire surface and the other boundary conditions (see Sections 3.3, 3.4 and 3.5). A stress increase,

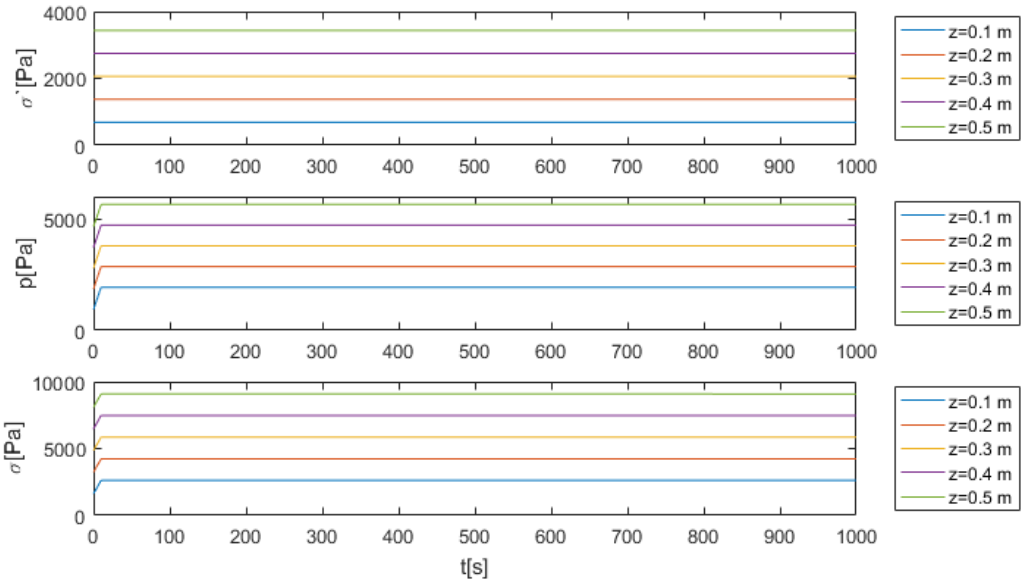

Figure 4.5: Development of effective stress (top plot), pore water pressure (middle plot) and total stress (bottom plot) for a homogeneous positive normal surface pressure, for points at different depths.

which is initially carried by the water pressure, is omnipresent in the modelled soil and the water pressure gradient remains unchanged. Consequently, water does not flow out, no strain occurs, so the effective stress does not change (see Equation 3.23). Note that this behaviour does not occur with an overtopping event in reality. For modelling overtopping waves that cover the entire model surface it is tackled by forcing the surface cell at the side boundary at the tail side of the wave to be unloaded.

The same stress is applied on a confined area of 1 m in the middle of the model, shown in Figure 4.1c. Also the results of this case show that the total stress is immediately in equilibrium. The equilibrium total stress distribution is shown by 4.6. The ratio between the effective stress and the water pressure develops. Initially the water pressure carries all the load and it develops to a situation where the effective stress carries all the load. This development is shown in Figure 4.7. The figure shows the deviation of the stresses from their values in the initial situation. The change in ratio is related to strain and flow of water. This implies that the stress distribution that is shown in Figure 4.6 equals the water pressure distribution immediately at the start of the load and it equals the effective stress distribution when a stress equilibrium is reached.

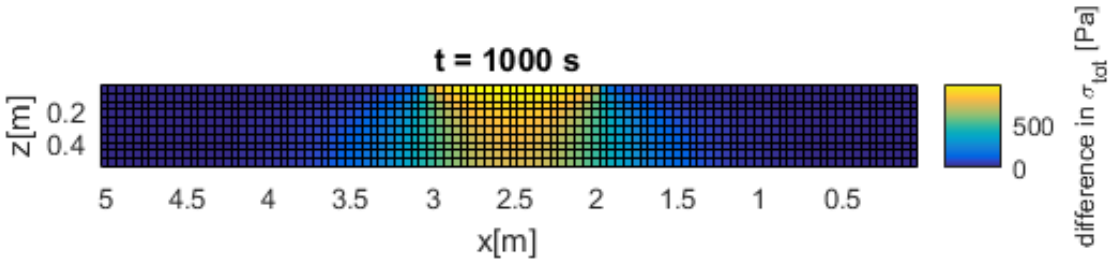

Figure 4.6: Deviation with respect to the unloaded situation of total stress in equilibrium state below a confined homogeneous normal stress load (see Figure 4.1c).

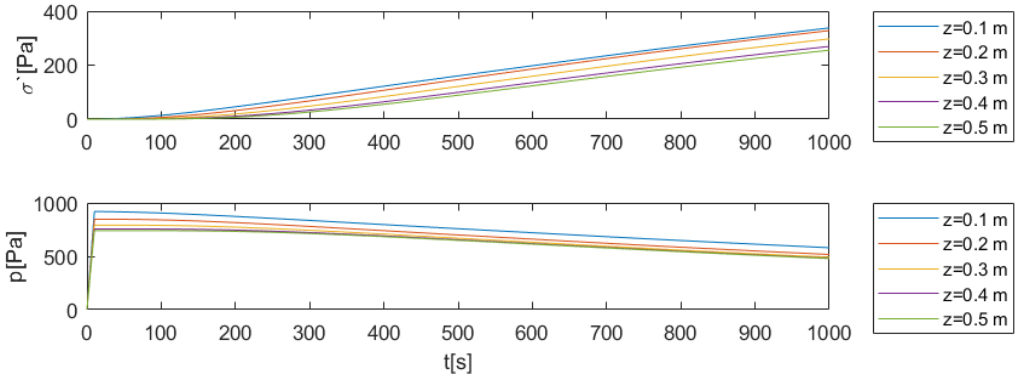

Figure 4.7: Development of the deviation from the initial values of effective stress (top plot) and pore water pressure (bottom plot) for a confined homogeneous normal stress load of 1000 Pa, for points at different depths at the middle vertical of the model.

4.2.3 Slope loaded by homogeneous shear stress gradient

A model case with a homogeneous shear stress load, with a constant gradient of $\frac{\partial \tau}{\partial z} = 100Pa/cell = 2000Pa/m$ on the entire model surface, was run, see Figure 4.1d. A positive shear stress gradient along the surface causes a pulling force on the soil (see Section 3.3.1).

Figure 4.8 shows the effect of a shear stress gradient on the total stress development. It is shown that the total stress is gets directly in an equilibrium. The deviation from to the initial situation is small. Additionally Figure 4.9 shows the development of the effective stress and water pressure.

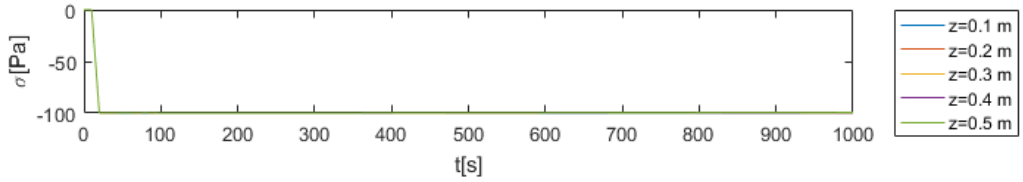

Figure 4.8: Development of the deviation from the initial values for the total stress for a homogeneous shear stress gradient load of 2000 Pa/m, for points at different depths at the middle vertical of the model.

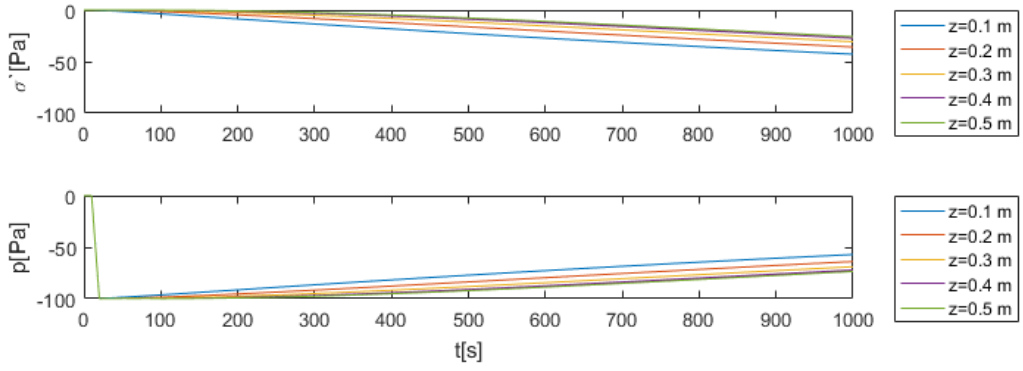

Figure 4.9: Development of the deviation from the initial values for the effective stress (top plot) and the water pressure (bottom plot) for a homogeneous shear stress gradient of 2000 Pa/m, for points at different depths at the middle vertical of the model.

The same stress is applied on a confined area of 1 m in the middle of the model, see Figure 4.1e. It shows a similar stress development for the total stress, with the difference that the deviation of the equilibrium stress with respect to the initial stress depends on the location in the soil, see Figure 4.10. At a larger depth the final stress deviation is larger. This is also valid for the effective stress and the water pressure, as shown in Figure 4.11.

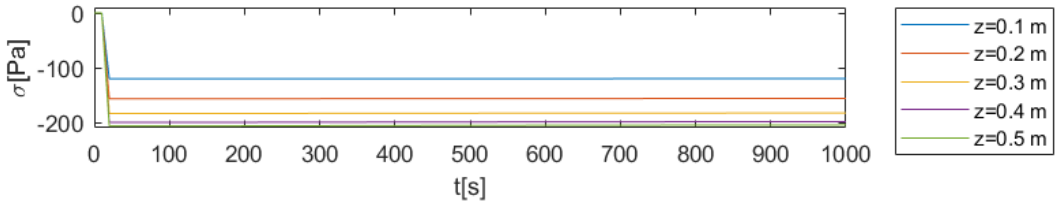

Figure 4.10: Development of the deviation from the initial values for the total stress for a confined homogeneous shear stress gradient load of 2000 Pa/m, for points at different depths at the middle vertical of the model.

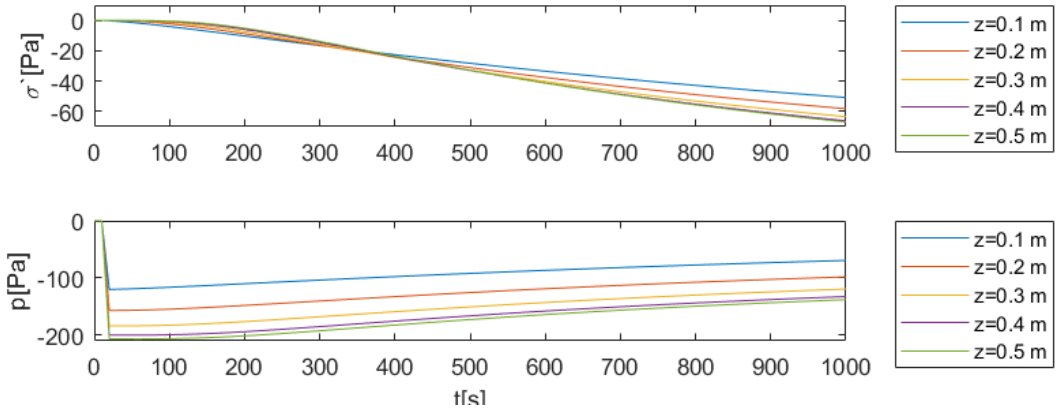

Figure 4.11: Development of the deviation from the initial values for the effective stress (top plot) and the water pressure (bottom plot) for a confined homogeneous shear stress gradient of 2000 Pa/m, for points at different depths at the middle vertical of the model.

Figures 4.9 and 4.11 suggest that inertia plays a role in the pressure propagation through the soil. The figures show that at smaller depths the stress change occurs earlier and the change is faster, than at larger depth.

4.2.4 Comparison with pressure measurements

For model verification, the measurements presented in Section 2.6 are modelled. For practical reasons an approach to the actual pressure signal is used: large stress gradients and the small time steps in the turbulent pressure signal raise the risk of instability and large inaccuracy in the current stage of model development. The approach is a smoothed wave signal, approaching the middle points of the turbulent oscillations. It is shown in Figure 4.12.
The shape of this wave signal matches the linear wave shape approach (Hughes [2011],

Hughes et al. [2012]). It states that wave characteristics decrease linearly, after passing of the wave front. The linearized wave signal in Figure 4.12 is shown by a bright red line. The characteristics of these approaches are given in Table 4.3.

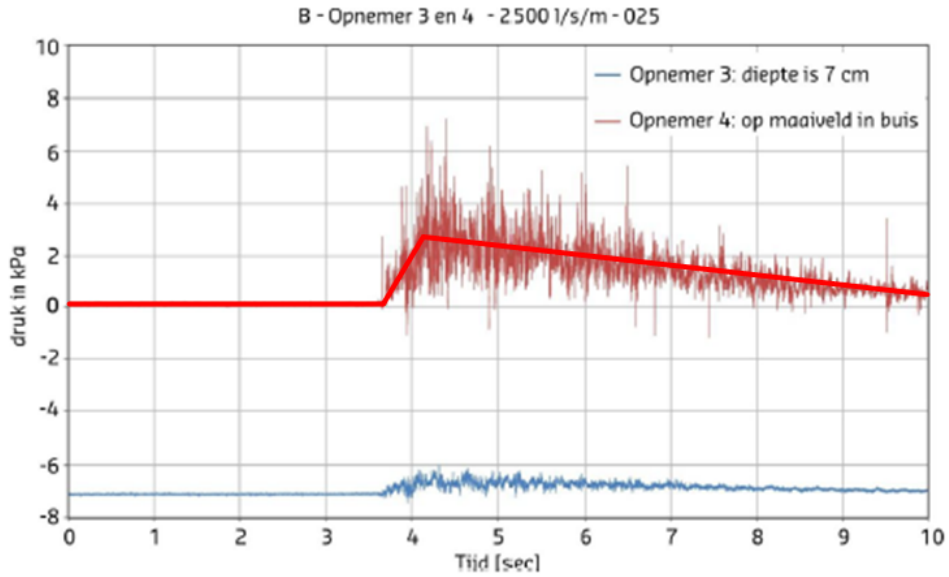

(a) Pressure development for an overtopping wave volume of 5000 l/m, at location B, during test series 1.

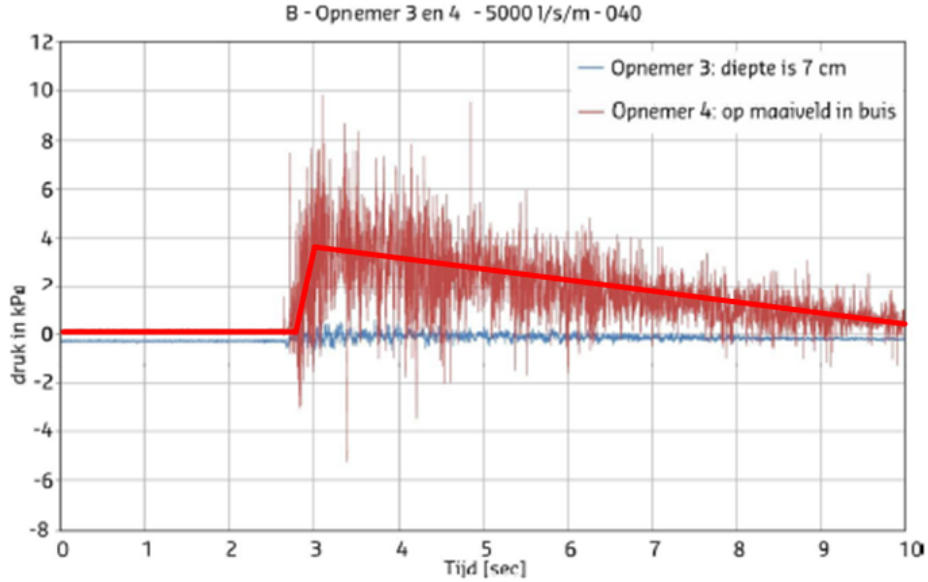

(b) Pressure development for an overtopping wave volume of 5000 l/m, at location B, during test series 1.

Figure 4.12: Pressure development as function of time for sensor 3 below surface and sensor 4 at surface and the linear wave shape approach for the surface wave given by a bright red line (for background of this figure, see Section 2.6).

Besides stress on the surface, shear stress acts on the surface. Shear stress (τ) is linked to the flow velocity (u), the density of water (ρ) and a friction factor (c_f), see Equation 4.1. A formula for the friction factor is given by Equation 2.18. Verheij et al. [2015] gives flow thickness measurements from the same campaign, showing that the maximum

Table 4.3: Characteristics of the linear approach of the pressure (σ) signals.

Wave number	**Figure**	σ_{max} $[Pa]$	$\partial\sigma/\partial t$ **front** $[Pa/s]$	$\partial\sigma/\partial t$ **tail** $[Pa/s]$
025	4.12a	2800	5000	400
040	4.12b	3800	14 000	450

flow thickness per wave for the considered cases is approximately 0.15 m, which is used to compute the friction factor.

$$\tau = c_f \rho u^2 \tag{4.1}$$

The velocity measurements of the selected waves, are shown in Figure 4.13. Per type of wave two different records are available, without any clear label on matching test wave number. The wave signals look alike. With lacking sufficient labeling and for simplification a linear approach on the wave velocity signal is drafted, alike the approach on the pressure signal. The characteristics of these approaches are given in Table 4.4.

Table 4.4: Characteristics of the linear approach of the wave velocity (u) signals.

Wave number	**Figure**	u_{max} $[m/s]$	$\partial u/\partial t$ **front** $[m/s^2]$	$\partial u/\partial t$ **tail** $[m/s^2]$
025	4.13a	8	40	0.98
040	4.13b	9	45	0.87

The results of the comparison computation are shown in Figure 4.14. In comparison with the measured pressure signals (see Figure 4.12) two significant differences on the pressure in the soil are observed.
First, the initial pressure in the soil is larger in the model results. The model computes the equilibrium pressure, based on a linear pressure increase linearly with depth. The measurements show negative initial pressures, indicating suction, with totally different values in both cases. This is supported by the observation that the initial stresses in the soil increased with increasing soil saturation, during the measurements (Verheij et al. [2015]).
Second, the change of pressure in the soil is larger in the model results. The change of pressure in the soil is almost as big as that on the surface, in the model results. The difference between the soil at the surface and in the soil in the measurements suggest the existence of pressure damping in the soil. The model results show no damping in vertical direction.

4.3 Model employment

To show the possibilities and the potential of the soil stress model, the current model is employed. A model case with a single wave was run. Section 4.3.1 gives the load computed with the concerned model function. This load is used as an input for the soil

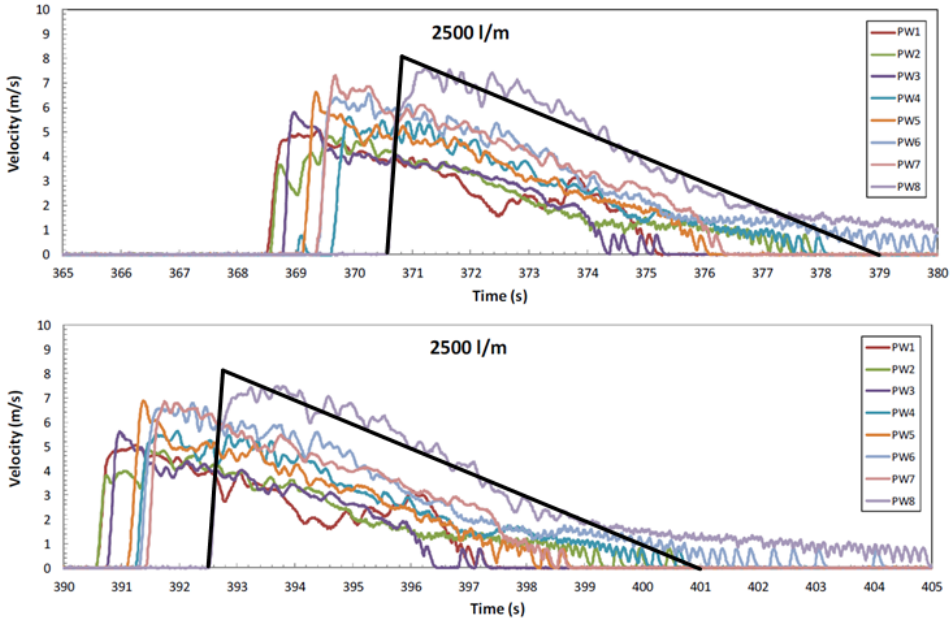

(a) Flow velocities for a wave volume of 2500 l/m.

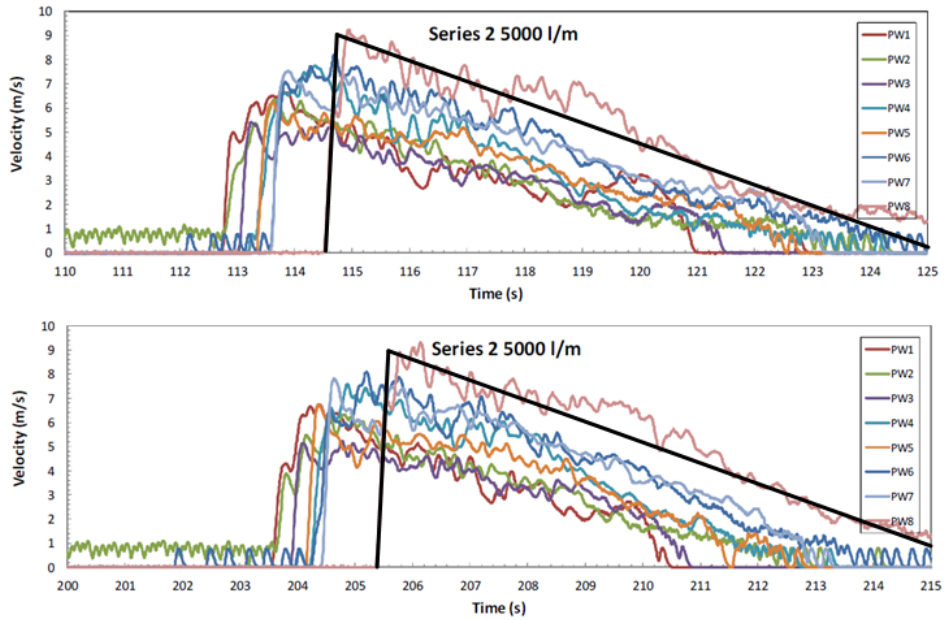

(b) Flow velocities for a wave volume of 5000 l/m.

Figure 4.13: Flow velocities for overtopping waves with location PW8 matching location B and linear wave velocity approach given by a black line (Verheij et al. [2015], edited).

stress model. The resulting stress distribution from the model run are shown in Section 4.3.2. The model is not finished yet and the resulting stresses are therefore considered to be a provisional approach. The resulting stresses are not further discussed in next chapters.

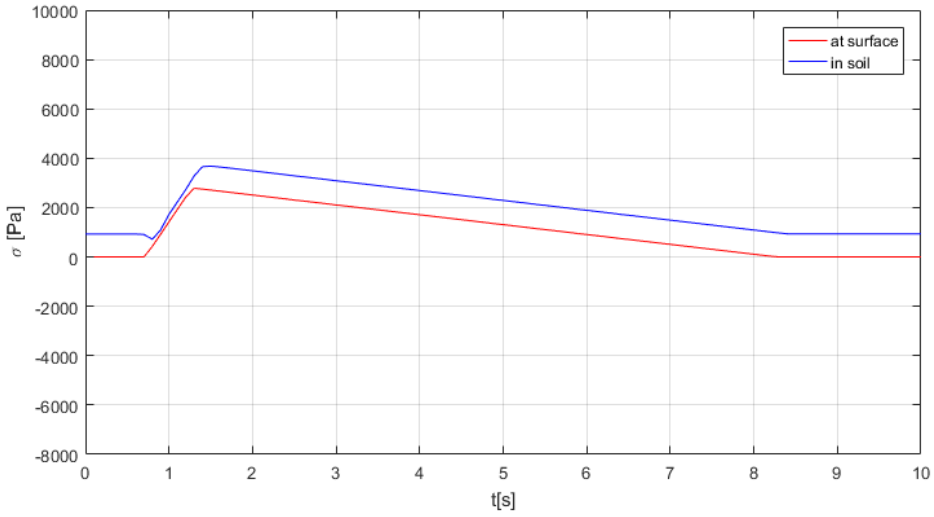

(a) Results of modelling wave 025, for comparison with Figure 4.12a.

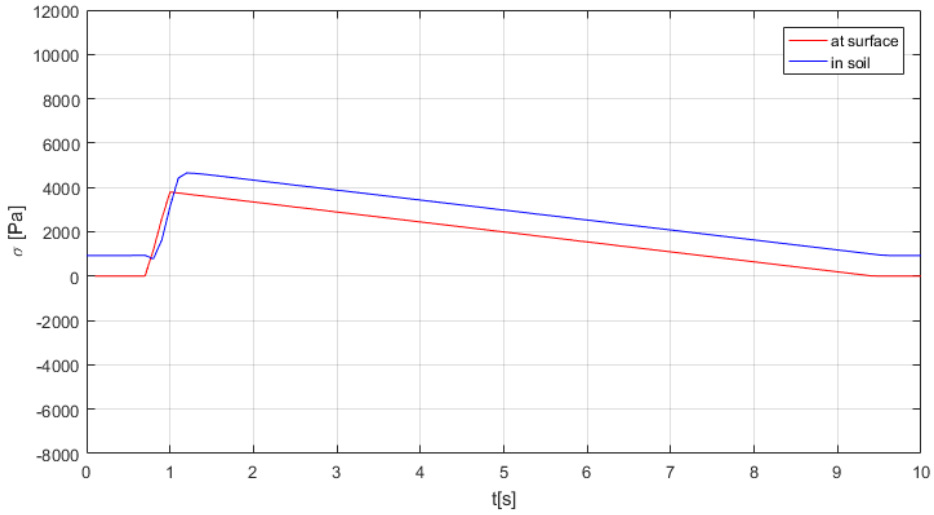

(b) Results of modelling wave 040, for comparison with Figure 4.12b.

Figure 4.14: Pressure development as function of time resulting from comparison computations, showing the measured stress at the surface (red) and the pore water pressure in the soil (blue).

4.3.1 Computed single wave load

Load on the slope is based on the approaches of wave distribution and development, presented in Section 2.2. The results for the default case are displayed in Figures 4.15 and 4.16. The location on the slope (x) is defined as distance along the slope surface to the crest.

Figure 4.15 shows the distribution of the peak flow depth and the peak flow velocity. It shows an increase in peak flow depth and a decrease in peak flow velocity, both declining with increasing distance to the crest. A decrease in peak flow depth causes an increase in peak shear stress and a decrease in peak normal stress.
It is assumed that stress by wave impact and by flow occur both in one overtopping cycle: A wave impacts and subsequently flows off. Figure 4.16 shows the normal and

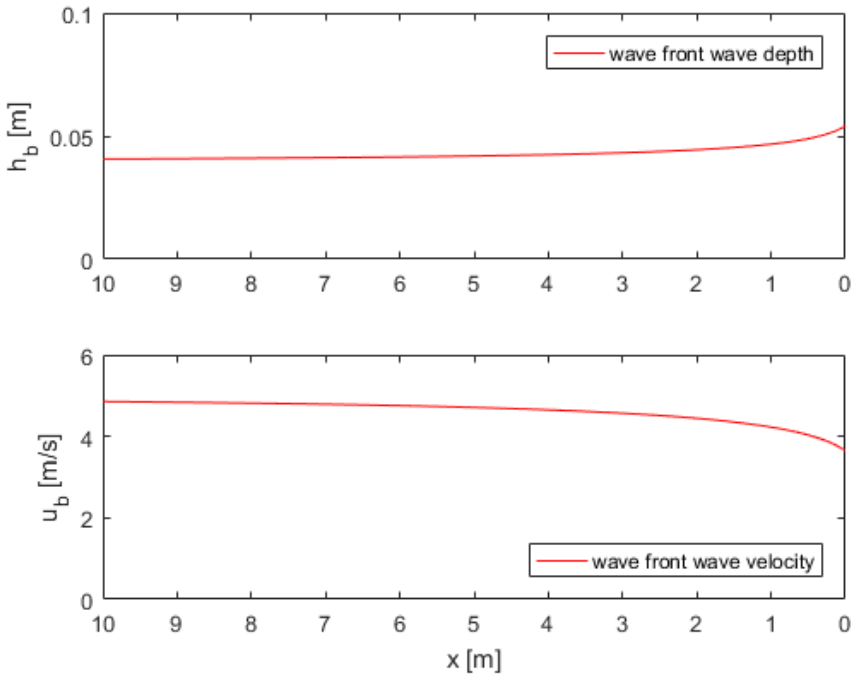

Figure 4.15: Distribution of wave depth and wave velocity of the wave front over a dike slope for the default overtopping case without wave separation.

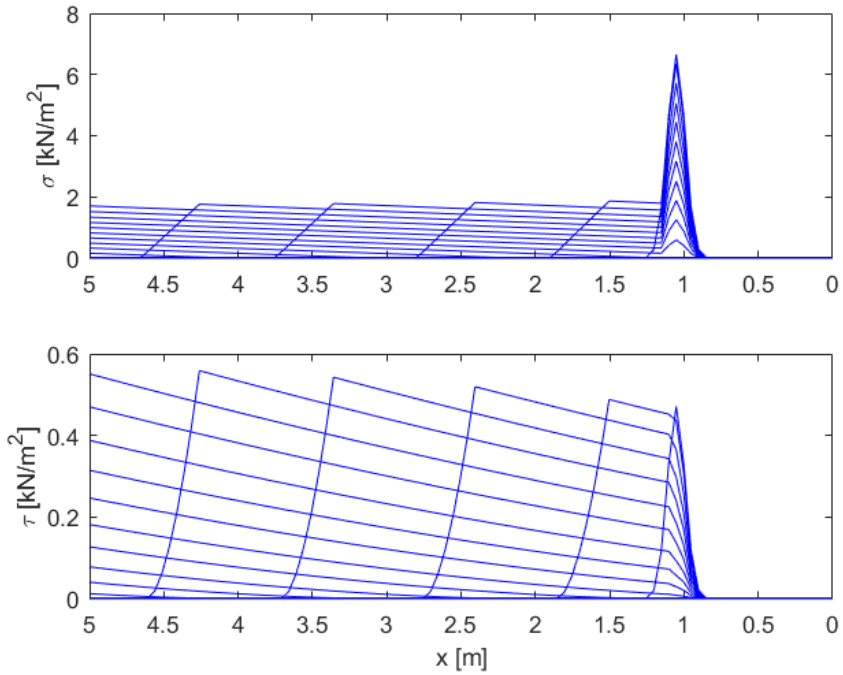

Figure 4.16: Instantaneous load, expressed in normal stress (upper plot) and shear stress (lower plot), of an overtopping wave with a display interval of $\Delta t = 0.2s$.

Table 4.5: Comparison of maximum values of different parts of the load for a default overtopping wave.

				wave impact		*dyn. pressure*	*shear stress*	
H_{m0}	$T_{m-1,0}$	$cot\theta$	R_c	$\sigma_{\zeta\zeta,max}$	$\tau_{\zeta\chi,max}$	p_m	τ	$\partial\tau/\partial z$
m	s	$-$	m	$[kN/m^2]$	$[kN/m^2]$	$[kN/m^2]$	$[kN/m^2]$	$[kN/m^3]$
1.0	4.0	1.0	3.0	6.66	0.47	2.27	0.60	4.31

shear stresses for this combined stress approach for the default load case. The plots show an instantaneous display of the wave load with a time interval of 0.2 seconds. They show a wave impact at approximately 1 meter from the crest, imposing a stress peak in normal stress. The shear stress increases when the waves flows down the slope. The normal stress decreases directly to values below the impact value and keeps slightly decreasing when the waves flows down the slope. The normative dynamic pressure is considered to be upward directed, in accordance with Hoffmans [2012].

4.3.2 Resulting soil stresses

This section shows some results of the soil stress computations for a case with load by a single overtopping wave. The model is able to produce more output than showed. Because the model is provisional and the results are not further discussed, the presented selection is limited to general soil stress results. Furthermore, the model is able to generate animations showing the development of soil stresses.

Figure 4.17 shows the development of the soil stresses different depths at one vertical at the slope. The stress signals look very similar. The maximum stress increase occurs later at a point deeper in below the surface. Furthermore the stresses directly prior to passing of the wave show a small decrease, which can be related to the total pull by the shear stress gradient at the wave front (see Section 3.3).

Figure 4.18 shows the deviation of the distribution of total stresses, with respect to the initial situation. Figure 4.18a shows it for a point in time during the passing of the wave front and Figure 4.18b shows it for a point in time during the passing of the wave tail. The figures show the largest stresses below the wave impact area and the wave front. They furthermore show limited horizontal dispersion of stresses, leaving the upper end of the dike (approximately $0m < x < 0.5m$) unloaded.

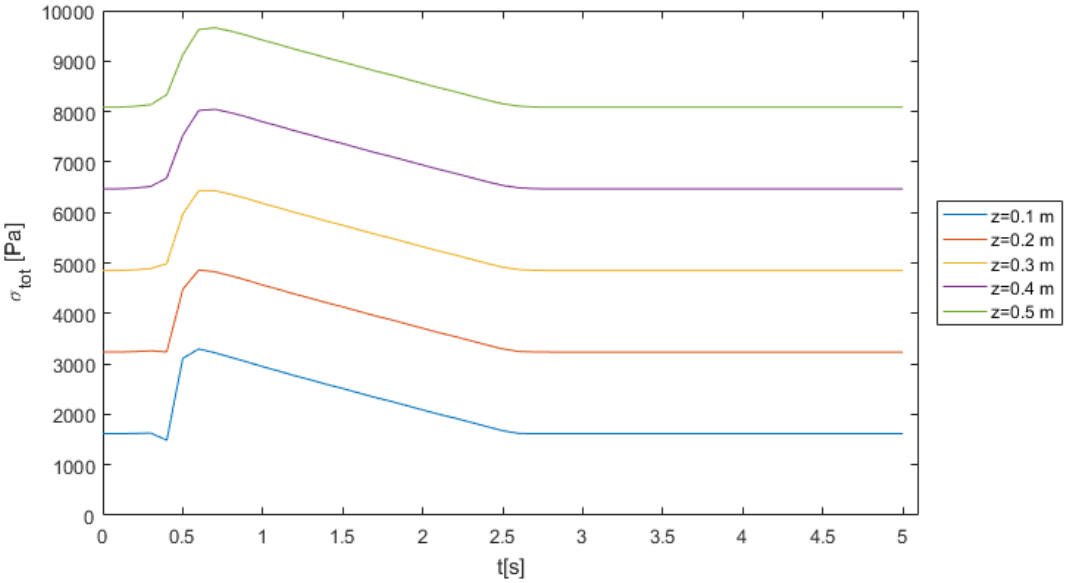

Figure 4.17: Development of total stress for a single wave overtopping load, for points at different depths at the middle vertical of the model.

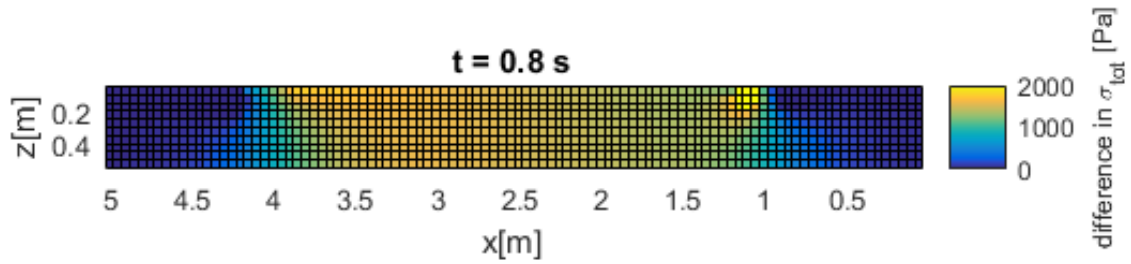

(a) Passing of the wave front.

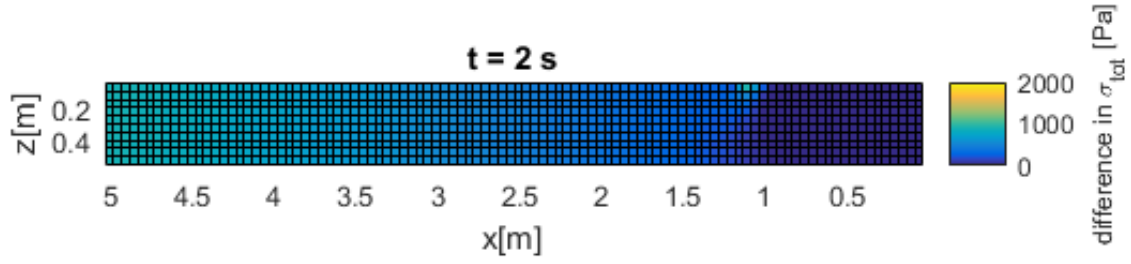

(b) Passing of the wave tail.

Figure 4.18: Deviation of the soil stress distribution with respect to the initial situation, at a distinct point in time, during the passing of a wave.

5 Discussion

The results are discussed in this chapter. The current model and the results of executed model runs are discussed Section 5.1. Next, in Section 5.2 adjustments to certain model characteristics, to improve the performance of the model, are discussed.

5.1 Current model

The current version of the soil stress model computes the distribution and development of soil stresses under a variable overtopping load in a 2D space. Comparison of stresses with soil strength, gives a prediction of failure caused by changes in soil stresses, alike soil lifting and head-cut damage. Further, the model can reveal blind spots in knowledge on geotechnical failure.
The model is unique in its ability to compute, aside from the soil stress reaction on load, the wave load on the soil itself. Based on the incoming wave conditions and dike geometry, considering multiple load mechanisms, the model computes a realistic wave load.

Results of soil stress computation for simple load cases are generally in agreement with the expectations based on analytical relations. The results can be explained, analytically or numerically. Load overtopping simulations by Verheij et al. [2015] are modelled as well. The resulting stresses from the model are compared with the measured soil stresses during simulations. The results show similarities and differences, indicating the need for further model development.

The model is developed with the intention to predict failure from comparing soil stress with soil strength, like e.g. Del [2016]. A good representation of occurring stresses is prioritized above adding soil strength and a comparison of stress and strength to the model. Implementation of soil strength is to be done. To predict failure it is required to consider variation of both wave load and soil strength (Zapata [1999], Verhaeghe [2005]).

To achieve this, a lot of effort has to be put in overcoming numerical difficulties (Chavent and Jaffré [1986]). In the current state of model development, the use of non-variable characteristics is sufficient.
Failure can be expected for the following combinations of stress and strength: Soil stress exceeding soil strength, negative stress exceeding soil tensile strength and stress gradient force exceeding soil strength (Section 2.1.2). Small negative stresses, significant increase in soil stresses and large stress gradients have been observed in the model results. This indicates the model's ability to compute failure. Note that the actual occurrence of failure depends on soil strength as well.

Further development makes the model applicable in dike design and assessment. This contains among other the introduction of probabilistic definitions, improvement of wave load definition, addition of damping (Sections 7.1 and 7.2). The fully developed model must be able to show accurately the soil stresses in realistic (minimal idealization) cover layers of realistic dike geometries and use that to determine the chance of local initiation of failure. These functions are useful in improving accuracy of safety calculations during dike design and assessment and in research on failure mechanisms caused by overtopping load (see Section 7.3).

5.1.1 Model structure

Balances
The model is based on an equilibrium of forces in the vertical and horizontal directions and irrotationality, limiting it to compute initiation of motion. Equilibrium of forces in a direction means the stresses at both sides of a soil section are equal, thus that all loads acting on one side of the model are transferred through the model. This neglects the soil strength, for instance provided by cohesion or internal soil deformation, which gives soil itself the ability to (partly) balance the load. This further neglects the presence of damping of forces in the soil, since all forces on the soil require an equal force in the opposite direction to keep forces balanced. This is supported by the validation case (Section 4.2.4), where the models shows a lack of stress decrease for a stress propagating through the soil. Rayhani and El-Naggar [2008] shows that the damping of forces in clay is significant. This gives rise to a significant difference between stresses in model results and reality. This difference and the lack of modelled damping is observed in Section 4.2.4.
The model is based on the assumption of mass balance, stating that no soil enters or leaves a grid cell. The effective stress and the pore water pressure are related via strain; strain is required for a change in effective stress to occur. However, strain violates the assumption of mass balance. For small strains and small grid cells, the change of mass in a cell is small. The model is valid till initiation of failure, thus deals with small strains only. Consequently, this violation of the mass balance is acceptable.

Surface boundary condition
For stability, the soil must satisfy horizontal, vertical and moment equilibrium. The boundary shear stress gradient matters for these, but is not considered previously. It is considered as a surface boundary condition in the developed soil stress model. Its effect when acting solely is shown in Section 4.2.3 and its effect at an overtopping wave front

in Figures 4.14 and 4.17. It seems to be of lesser influence than the normal stress. Its contribution to the total soil stress reaction has to be proved.
The shear stress from a flow on soil is debated, according to the number of existing definitions (e.g. Darcy [1857], Manning [1891], Colebrook and White [1937], Rouse [1943]). Mutual differences are usually small. For this research the Manning formula is used for its physical background, its open flow origin and its wide use.

Soil saturation
The conventional assumption of saturated soil during overtopping conditions, usually stormy conditions, is used (Young [2005], Hoffmans et al. [2008], Bijlard et al. [2017]). This makes the model apply on cases with a load on soil in a wet environment, like wave overtopping, wave run-up and dredging. However, considering some observations during tests this can be debated (Collison and Simon [2001], van Hoven et al. [2011], Verheij et al. [2015]). These test where during simulations, not during actual storm conditions. Observations indicating unsaturated soil are considered not representative for wet, stormy conditions. The conventional assumption is considered to be valid.
Fully saturated soil implies a ground water flow parallel to the slope. If the slope of the flow is more gentle, the degrees of saturation vary along the slope, which influences the soil behaviour (Sun et al. [2012]). According to the conventional assumption of saturated soil, the variation of saturation along the slope is considered to be small and the approach to be sufficient.

Stress definitions
The relation between the effective stress and pore water pressure, a *coupled approach*, is newly derived (Section 3.3.2). The initial situation and soil reaction is fully saturated, and becomes unsaturated under persistent load. The development of the pore water pressure and effective stress, w.r.t. each other, that is shown in simple load cases (Section 4.2) matches expectations (Section 2.7).
A conventional approach for wave overtopping computations is to consider fully saturated soil only. For instance, the *CSSM model*, based on the *critical state concept* is used in macro stability assessments (Roscoe et al. [1958], Schofield and Wroth [1968]). In reality the degree of saturation is somewhere in between and the load is distributed over the effective stress and the pore water pressure. Hence, saturated soil computations give an underestimation of effective stress. An *uncoupled approach* takes this distribution into account (Wang [2000]). The drawback of this approach is that it neglects the deformation of soil and the interaction between pore water and soil particles. *Coupled approaches*, relating soil particle behaviour to pore water behaviour, exist as well, e.g. Griffiths [1994], Elsafti [2015]. No approach is found to be applied on wave overtopping, making comparison with the developed soil stress model hard.

Soil stress development in time during a variable load is approached by an exponential function. This is considered as valid as the similar approach of a constant load (Churchill [1972], Verruijt [2008]), provided the application of an adjustment. Comparison of an original load with the approach shows small differences (see Section 3.3.3). These can arise from the inaccuracy in the exponential approach or the numerical approach. Deviations between the load applications are small w.r.t. load changes in time. The approach is sufficient for this research.

The total stress is defined as the sum of the effective stress and the pore water pressure.

Other modelling software, for instance Plaxis2D, defines total stress independently from the effective stress and pore water pressure (Brinkgreve et al. [2018]). Due to this definition, the model cannot deal with wave imposed liquefaction alike failure, where increase in pore water pressure and constant total stress lead to a loss of effective stress. This failure is observed by Suzuki and Takahashi [2003] and imaginable to occur in saturated soil. Since it is not acknowledged as a type of failure due to overtopping on dikes (Section 2.1), this deficiency is considered to be tolerable for the purpose of this research.

5.1.2 Verification and validation

Verheij et al. [2015] provides data of 28 waves that are used for validation. Unreliable measurements are indicated in the data set. No large deviations, indicating errors, are observed between different measurements. An omnipresent error, e.g. a sensor error, can flaw the data. Furthermore, soil discontinuities - the sensor itself is one - can affect transmission of stress on the sensor (Lamandé et al. [2015]). However, the results show reasonable wave data. Besides, the data is considered to be useful by experienced parties in this research field, suggesting reliable and useful data.
Note that the data originates from a single test location. It is representative for the tested dike sections and similar dikes only (see Greeuw [2013] and Verheij et al. [2015]).

Qualitative verification shows reasonable model results. Unloaded soil does not react, as is expected. Soil loaded a normal stress or a shear stress gradient shows a corresponding change in stress; stress increase for a pushing force and stress decrease for a pulling force. The pore water pressure carries initially all load and is gradually released by the effective stress, as expected. Deviating results (see Section 4.2.2) are explained numerically.
More complex overtopping loads (Sections 4.2.4 and 4.3) are hard to verify using analytical solutions. The results in Section 4.2.4 are compared to measurements, and show large similarities. The results in Sections 4.2.4 seem to be reasonable.

5.2 Limitations and points of improvement

Load by dynamic pressure is approached by a representative value, related to the water depth. This creates a smooth pressure signal. Pressure oscillations in the actual load create a dynamic stress environment in which the physics is hard to model. Christakos [2003] shows a difference in resulting soil pressure, for a variable and a constant load.

Wave impact load is defined using a continuum approach. Cooker and Peregrine [1995] show that impulsive load gives different stresses. This causes differences between the modelled stress and real stress.
The impulsive load approach applies on wave impact on convex slope transitions and objects as well. These are to be included.

The assumption of a very small angle of repose limits the domain of applicability to saturated soils. This assumption is fundamental for the model structure, thus it has a limiting effects on model extension. The current domain is sufficient for this research.

The current model is designed for a single wave load on a soil in force equilibrium. Bijlard [2015] shows that load repetition reduces the soil strength (fatigue). Furthermore, the load history, expressed in the *Overconsolidation ratio*, has an increasing effect on the soil strength (Stróżyk and Tankiewicz [2014]). These effects are to be included in the model to improve the accuracy of computing series of waves.

6 Conclusions

This chapter gives the final conclusions of this research, split up in conclusions on the research objectives (Section 6.1) and conclusions on the research aim (Section 6.2), both introduced in Section 1.2.

6.1 Objectives

In this section the conclusions on the accomplishment of the research objectives is given separately. The research objectives are given below, followed by the accompanying conclusions.

> *Develop a model to compute the development of soil stresses for an imposed hydrodynamical overtopping load.*

A new model is developed that computes stresses caused by surface load, for application on wave overtopping cases and cases of similar environmental conditions. The model contains a newly derived load definition, considering shear stress gradient force on the surface, and a newly derived coupled definition for the effective stress and pore water pressure. Next to soil stress computations, the model is able to compute overtopping wave load, from wave conditions and dike geometry characteristics.
During model development, some assumptions are made and some uncertainties are accepted. This gives rise to possibilities for further development that will improve the model.

> *Validate the soil stress representation of the model.*

The model results for simple loads match the expectations based on analytical solution. Model results for an overtopping wave show similarities with measurements during overtopping simulations. Observed differences emphasize the possibilities for further de-

velopment that are mentioned before.
Overall, the model gives a reasonably matching soil stress representation.

Employ the model to predict geotechnical failure.

The current model can indicate locations with a risk for failure, based on the stress distribution. These are failures by soil lifting (head-cut or of different scale) and possibly yet unknown mechanisms. It does not yet consider soil strength and is thus not yet able to give an accurate prediction of geotechnical failure. Soil strength is to be implemented. Model employment for an overtopping wave indicates a few locations that require attention regarding failure due to stresses: stress decrease at the wave front, large stress gradients below the wave front, large stress increase below the wave peak and local stress increase at the wave impact location.

6.2 Research aim

In this section the conclusions on the accomplishment of the research aim are given. The research aim is given below, followed by the accompanying conclusions.

Improve the understanding of initiation geotechnical failure of a dike cover during overtopping wave load.

The developed model is a tool to disclose and show the effects of an overtopping wave on the soil stress in the dike. This is a new and fundamental approach to researching and explaining overtopping failure.
The model development itself does not lead to an improved understanding of geotechnical failure caused by wave overtopping but use of this tool for multiple different cases does. Hence, this research has not yet improved the understanding of geotechnical failure caused by wave overtopping. However, by developing a tool that can be applied on individual overtopping cases it has made a large contribution to it.

7 Recommendations

The model development is not finished. This chapter addresses the future of the soil stress model. The model can be improved on many points. Section 7.1 gives the improvements that are most important and realistic to execute. The model improvement is defined as the trajectory till the model gives correct representation of soil stress for a certain load. In Section 7.2 long term developments are described. Once the current model works properly, these can be executed to extend the model and enlarge its domain of applicability. Finally, Section 7.3 gives a number of model runs that serve as goals in further development. At the start of this research it was intended to solve these cases with the soil stress model.

7.1 Model improvement

Do additional model validation.
The model is limitedly validated. Validation can be improved with comparing a model case with other suitable software, e.g. *PLAXIS 2D* or *COMSOL multiphysics*. It can also be improved with a comparison of accurately matching overtopping wave and model case. An accurate match can be best achieved by doing an overtopping wave simulation in a laboratory flume, from which all relevant characteristics from wave and dike are known or can be measured. Additional validation can lead to additional recommendations concerning further model development.

Improve input characteristics.
Most wave load and soil characteristics can appear in a range of values and are applied with uncertainty. Further research on the values of corresponding parameters, site research when computing real cases and application of probabilistic definitions decreases this uncertainty. It is advisable to use a Monte Carlo method for probabilistic analysis, as it is efficient, simple and commonly used (Kroese et al. [2014]). A sensitivity anal-

ysis indicates the parameters that have most influence on the model results have to be prioritized in further research.

Implement turbulent oscillations in the wave overtopping load.
Oscillatory turbulent wave load is replaced by a more constant representative value. Oscillatory and constant loads lead to different soil stresses. The correctness of wave load representation improves by addition of turbulent motion. Due to the complexity of turbulence and its role in the model, it is advisable to develop an approach to the turbulence induced load based on spectral analysis of turbulent flows (see e.g. Bolotnov et al. [2010]) or, if possible, to do load measurements. Short oscillatory motions increase the risk of model instability and significant inaccuracy. Measures must be taken to prevent this. For instance, by changing the size of the time step and model grid cells.

Improve the approach of wave impact load.
Wave impact load is modelled using a continuum approach, but it is not a continuous load. Continuous and non-continuous load lead to different soil reactions. Impact load representation improves with application of a method that suits impulsive loads caused by impacting water (Cooker and Peregrine [1995]).

Add damping on the soil stress.
Model results suggest the lack of soil damping in the model. Adding damping improves the model. To add damping an extra soil characteristic, concerned with damping, can be applied. Soil stress damping is extensively researched in the field of earthquake engineering (e.g. Ashmawy et al. [1995]). Further, it is advisable to study whether the water pressure propagation can be a source of damping: viz it can be reasoned that pore water pressure not immediately adapts to added load in a clay dike cover.

7.2 Model extension

Add computation step to determine chance of failure.
The model does not indicate the initiation of failure yet. A comparison between occurring soil stresses and present soil strength, accomplishes this. If model parameters are defined probabilistic, the chance of failure of each point in the model domain can be determined.

Add the option for computation with spatial variability in the soil.
The current model lacks spatial variability in the soil. To do research on the influence of soil discontinuities, such as holes and soil layer separation, it must be possible to model them. For calculating the chance of failure it is useful to input soil discontinuities, such as grass and pavement. To input spatial variability, soil characteristics must be determined for each point in the computation grid. Considering usability, soil characteristic definition must be less effort than manually importing all values for each point in the grid.

Enable computations for non-planar parts of the slope surface.
To apply on the entire dike slope, the model must be able to deal with objects on the slope, concave slope angle transitions and convex slope angle transitions. Application of a method that suits impulsive loads (Cooker and Peregrine [1995]) contributes to ability of the model to deal with objects and convex transitions. Further research on flow separation (Ramamurthy and Vo [1993]) contributes to ability of the model to deal

with concave transitions. Note that objects and slope transitions locally influence the flow and the amount of turbulence (see e.g. Dargahi [1989]). The effect of this influence must be researched.

Enable the connection with other hydrodynamic models.
Detailed hydrodynamic models computing overtopping load, exist (e.g. Bomers et al. [2016]). The applicability of the model profits from the option to connect it to existing models. This option reduces the urgency to improve load modelling to large accuracy (see Section 7.1), shifting priority to the improvement of the soil stress part of the model.

7.3 Future model employment

This research started with the intention to improve the knowledge on failure due to overtopping. The soil stress model development is started with the intention to compute the soil stress distributions and development in the soil under overtopping load. In this context model development started with the final goal to employ the model by computing cases that can contribute to the knowledge of wave overtopping. These employment cases must serve as long term goals in further development. The following employment cases are considered:

- Research on the influence of different load mechanisms: Compare results of different models with different single load mechanisms;
- Research on the difference between overtopping and overflow: Compare model results of a continuous overflow load without a point of impact wave with the results of repetitive overtopping waves of the same cumulative wave volume per unit of time;
- Research on the effect of pulsating load: Compare model results of one big overtopping wave with the results of multiple small waves of the same cumulative wave volume;
- Research on the required strength a grass cover: Compare resulting soil stress distribution with the soil strength distribution to determine the additional strength that grass have to provide to prevent failure;
- Research on the effect of local weak spots in the soil: Compare model results of models with and without different weak spots in the soil composition;
- Research on accumulating effect of an entire overtopping event: Model an overtopping load that represents an entire overtopping event, by using a probabilistic definition of model parameters.

List of Figures

1.1 Distinction of stages an incident wave on a dike runs through Schüttrumpf and Oumeraci [2005]) . . . 2
1.2 Locations of failure that are observed frequently during tests. . . . 3
1.3 Sketch of the setup of a numerical model with soil divided in grid cells, spatial variable loading forces (black arrows) and possible reaction forces (red arrows). . . . 6

2.1 Principle sketches of some distinguished types of failure due to overtopping (Valk [2009], Trung and Verhagen [2014]). . . . 11
2.2 Development of flow overtopping parameters on the crest of a dike van der Meer et al. [2016]) . . . 13
2.3 Conceptual scheme of instantaneous normal forcing on the soil surface generated by unbalanced pressure distributions (Bellin and Fiorotto [1995]) 16
2.4 Principle sketch of shear stress gradient load, with in red the shear stress and in blue the shear stress gradient force. . . . 17
2.5 Separation of an overtopping 1000 l wave before impacting on the land-side slope. (Ponsioen [2016]) . . . 19
2.6 Approach for forcing on the slope by an impacting wave, per unit width (Ponsioen et al. [2017]) . . . 19
2.7 Distinction of components of a grass cover layer (Muijs [1999]) . . . 21
2.8 The Mohr-Coulomb criterion. The circle represents possible combinations of shear and normal effective stress. The straight lines represent critical combinations of shear and normal effective stress. . . . 22
2.9 The effect of multiple loading events on the stiffness of soil (Verruijt and van Baars [2009]). . . . 25
2.10 Young's modulus of distinct groups of materials (Cambridge University [2002]) . . . 26
2.11 Kelvin-Voigt diagram with a spring element, representing elasticity (K), and a dashpot element representing damping (C). . . . 27
2.12 Soil layer springy and damping support modelled by a Winkler model with Kelvin-Voigt diagrams, for a random load. . . . 27
2.13 Cross section of the test setup during the measurement campaign that includes pressure measurement during wave overtopping simulations (Verheij et al. [2015], edited). . . . 29
2.14 Test setup for pressure measurement during wave overtopping simulations (Verheij et al. [2015]). . . . 29
2.15 Pressure development as function of time for sensor 3 below surface and sensor 4 at surface (Verheij et al. [2015]. . . . 30
2.16 Chain of events that is expected as a reaction on surface load. . . . 31

3.1 Forcing on an inclined soil element of finite dimensions. 34
3.2 Water pressure increase along the z-axis (blue) and effective stress increase along the actual depth (brown). 39
3.3 Overview of the spatial variable use of Dirichlet and Cauchy boundary conditions on the surface boundary at the locations with and without wave load. 40
3.4 Schematic representation of all boundary conditions (BC) on the soil model. The surface BC is explained in Section 3.3, the side BC in Section 3.4 and the bottom BC in Section 3.5. The BC for effective stress are shown in brown and the BC for water pressure are shown in blue. The surface BC for effective stress and water pressure are linked and are variable in configuration. More detail of this BC is given in Figure 3.3. . 41
3.5 Forces originating from stress gradients and gravity, that contribute to the 2D force equilibrium on a soil element. Displayed forces are not to scale. 42
3.6 Origin of the numerator and denominator in the definition of f_{load} (Equation 3.46). 44
3.7 Effective stress development in the soil resulting from a model with Dirichlet surface boundary conditions and an approach of this development with the exponential function derived from theory (Equation 3.48) with $s = 6.4 * 10^{-4}$. 45
3.8 Resulting effective stresses, water pressures and total stresses from model runs with application of different boundary conditions. 45
3.9 Model nesting as applied. 46
3.10 A 3 dimensional discrete model grid with a width of I cells and a depth of J cells on each time step t. 49
3.11 Stencil of the Theta-Central scheme with $\theta = 1$. In horizontal direction integration steps in space (i,j) and in vertical direction integration steps in time (n) are shown. The white dot is the computed value $\sigma'^{n+1}_{i,j}$. . . . 49
3.12 Stencil of the Central scheme. In horizontal direction integration steps in space (i,j) are shown. The white dot is the computed value $p^{n+1}_{i,j}$. 50
3.13 Stencil of the FTCS scheme. In horizontal direction integration steps in space (i,j) and in vertical direction integration steps in time (n) are shown. The white dot is the computed value $\sigma'^{n+1}_{i,j}$. 51

4.1 Computed simple load cases. 58
4.2 Initial stress distribution, showing a linear slope normal stress increase. 59
4.3 Value of the soil stress, relative to the initial stress state, after 1000 seconds of zero load. 60
4.4 Comparison of the slope normal stress distribution of a soil in unloaded equilibrium with the initial slope normal stress distribution in the model and the slope normal stress distribution resulting from a model run. . . . 60
4.5 Development of effective stress (top plot), pore water pressure (middle plot) and total stress (bottom plot) for a homogeneous positive normal surface pressure, for points at different depths. 61
4.6 Deviation with respect to the unloaded situation of total stress in equilibrium state below a confined homogeneous normal stress load (see Figure 4.1c). 61

4.7 Development of the deviation from the initial values of effective stress (top plot) and pore water pressure (bottom plot) for a confined homogeneous normal stress load of 1000 Pa, for points at different depths at the middle vertical of the model. 62
4.8 Development of the deviation from the initial values for the total stress for a homogeneous shear stress gradient load of 2000 Pa/m, for points at different depths at the middle vertical of the model. 62
4.9 Development of the deviation from the initial values for the effective stress (top plot) and the water pressure (bottom plot) for a homogeneous shear stress gradient of 2000 Pa/m, for points at different depths at the middle vertical of the model. 62
4.10 Development of the deviation from the initial values for the total stress for a confined homogeneous shear stress gradient load of 2000 Pa/m, for points at different depths at the middle vertical of the model. 63
4.11 Development of the deviation from the initial values for the effective stress (top plot) and the water pressure (bottom plot) for a confined homogeneous shear stress gradient of 2000 Pa/m, for points at different depths at the middle vertical of the model. 63
4.12 Pressure development as function of time for sensor 3 below surface and sensor 4 at surface and the linear wave shape approach for the surface wave given by a bright red line (for background of this figure, see Section 2.6). 64
4.13 Flow velocities for overtopping waves with location PW8 matching location B and linear wave velocity approach given by a black line (Verheij et al. [2015], edited). 66
4.14 Pressure development as function of time resulting from comparison computations, showing the measured stress at the surface (red) and the pore water pressure in the soil (blue). 67
4.15 Distribution of wave depth and wave velocity of the wave front over a dike slope for the default overtopping case without wave separation. 68
4.16 Instantaneous load, expressed in normal stress (upper plot) and shear stress (lower plot), of an overtopping wave with a display interval of $\Delta t = 0.2s$. 68
4.17 Development of total stress for a single wave overtopping load, for points at different depths at the middle vertical of the model. 70
4.18 Deviation of the soil stress distribution with respect to the initial situation, at a distinct point in time, during the passing of a wave. 70

A.1 **Afsluitdijk, section 1.** Final slope failure after 6 hours simulation with a maximum load of 75 l/s/m overtopping waves. Damage appears as rather even removal of the upper layer, starting at the toe of the dike and developing slope upward, but no hole develops. 112
A.2 **Boonweg, section 3, initial damage.** Slope failure of a saturated grass cover during a simulation, during the second hour of 75 l/s/m overtopping waves. The forcing of the water caused roots to snap, which enabled the formation of a protruding bulge filled with water under the grass cover. During further load the balloon bursted and the grass cover flushed away. 113

A.3 **Boonweg, section 3, final damage.** Failed slope after a simulation with a maximum load of 75 l/s/m overtopping waves. Failure started halfway the slope of the dike and developed down the slope. 113
A.4 **Boonweg, section 4.** Slope failure during a simulation with a load of 75 l/s/m overtopping waves. Development of a protruding bulge filled with water. Bulge withstood overtopping waves for 5 minutes before bursting. 114
A.5 **Kattendijke, section 1.** Slope failure after 5 hours and 40 minutes simulation with a maximum load of 75 l/s/m overtopping waves. Failure of the maintenance road down the toe of the dike, starting at the side away from the dike and developing towards the dike. 115
A.6 **Sint Philipsland.** Slope failure after a simulation with a maximum load of 50 l/s/m overtopping waves (right picture). Failure from the slope of the dike, expected weak spot of a large mole hole remained intact (left picture). 115
A.7 **Tholen, section 2.** Slope failure during a simulation, after 1 hour of 5 l/s/m overtopping waves. Clear development of damage in the juncture between the soil cover and the stairs. 116
A.8 **Tholen, section 3.** Failed slope after a simulation with a maximum load of 5 l/s/m overtopping waves. Failure shows macro instability: a large chunk of soil has slipped off. It is remarkable that a location at the slope cover was a weaker spot than the objects on the slope. 116
A.9 **Tholen, section 4.** Slope failure after a simulation with a maximum load of 30 l/s/m overtopping waves. Failure at the toe of the dike, in the transition from the sloping to flat soil surface. 117
A.10 **Tielrode, section 1.** Slope failure after 35 minutes simulation with a maximum load of 30 l/s/m overtopping waves. Start of failure of the slope cover close to the crest of the dike and developing downwards. 117
A.11 **Tielrode, section 4.** Slope failure after 3 hours simulation with a maximum load of 10 l/s/m overtopping waves. Start of failure of the slope cover at multiple locations. 118
A.12 **Vechtdijk, test 2.** Start of failure by heavy erosion around a protruding object. 118
A.13 **Vechtdijk, test 3.** Slope failure after incremental development. Damage started close to the crest, developed down slope as removal of grass layer and started to develop as a head-cut erosion at the lower half of the slope. 119
A.14 **Wijmeers II, section III.** Slope failure after 1,5 hours simulation with a maximum load of 25 l/s/m overtopping waves. Failure started as a shallow damage (removal of grass cover over the total length of the slope) and eroded to the core of the dike. 120

B.1 Model of action of forces for a crack exposed to an impacting pressure (Stanczak et al. [2007]) 122
B.2 Extended model of action of forces for a crack exposed to an impacting pressure (Stanczak et al. [2007]) 123
B.3 Root Volume Ratio (RVR) as a function of depth under the surface for dike grass (Sprangers [1999]) 124
B.4 Apparent root cohesion (Vavrina [2006]). 125

B.5 Principle sketch of flexible elastic perpendicular root reinforcement leading to apparent root cohesion (Wu et al. [1979]). 125
B.6 Slip circle model for stability calculation based on the weight of the soil (W) the normal bearing force (P), the horizontal soil pressures (E_n and E_{n+1}) and the shear stress along the slip circle (S) (Bishop [1955]) 126
B.7 Forces acting upon a turf element according to the turf element model (Hoffmans [2012]) 127

C.1 a) Failure of the clay cover with grass in breaching of a sea dike initiated by wave overtopping. b) Failure of the sand core in breaching of a sea dike initiated by wave overtopping. Modelling phases and simulated processes as described by d'Eliso [2007]. 130

D.1 Pressure impulse field for half a jet impacting on an infinite stiff wall normal to the direction of the jet flow. The center of the jet is at z/h = -1, the free surface of the jet at z/h = 0. 134
D.2 Decomposition of the forces of a jet impacting on an inclined surface. . . 135
D.3 Pressure field caused by impulse for half a jet impacting on an infinite stiff wall with an inclination with respect to the direction of the jet flow. The center of the jet is at z/h = -1, the free surface of the jet at z/h = 0. . . 136

E.1 Distribution of change in effective stress with respect to the initial situation, for a homogeneous surface load of -1000 Pa, after a COMSOL model run of 15 seconds. 138
E.2 Distribution of change in effective stress with respect to the initial situation, for a surface load of -1000 Pa at the middle 2 meters of the model surface, after a COMSOL model run of 15 seconds. 139
E.3 Distribution of change in effective stress with respect to the initial situation, for a surface load of -1000 Pa, after a model run of 15 seconds. . . . 139
E.4 Distribution of change in effective stress with respect to the initial situation, for a surface load of -1000 Pa at the middle 2 meters of the model surface, after a model run of 15 seconds. 139

List of Tables

3.1 Default spatial model dimensions. 48
3.2 Values of parameters used for indicative load computations, based on CLASH. 52
3.3 Values of non-variable coefficients used for indicative load computations. 52
3.4 Default parameter values for soil pressure modelling. 54

4.1 Changeable variables in the soil stress model. Sections from top to bottom contain variables considering the following characteristics: numerical, geotechnical, geometrical and hydrodynamical characteristics. 56
4.2 Overview of applied defective approaches on modelling of the surface boundary condition and corresponding flaws in the results. 57
4.3 Characteristics of the linear approach of the pressure (σ) signals. 65
4.4 Characteristics of the linear approach of the wave velocity (u) signals. . . 65
4.5 Comparison of maximum values of different parts of the load for a default overtopping wave. 69

E.1 Deviant and additional model parameter input for the COMSOL model. 137

Nomenclature

Latin symbols

a	Depth of a soil crack	m
a	Wave shape exponent	–
b	Wave shape exponent	–
C	Chezy coefficient	$m^{1/2}/s$
c	Soil cohesion	N/m^2
c_f	Friction factor	–
c_n	Dashpot coefficient in normal direction	–
C_p	Primary compression coefficient	–
C_R	Apparent root cohesion	$m^{1/2}/s$
C_s	Secondary compression coefficient	–
C_{10}	Logarithm compression coefficient	–
C_{clay}	Rupture strength of clay	N/m^2
$c_{h,2\%}$	Overtopping wave coefficient	–
$c_{v,2\%}$	Overtopping wave coefficient	–
D	Damage factor	–
E	Young's modulus	N/m^2
E_c	Constrained Young's modulus	N/m^2
F	Factor of stability	–
F_c	Cohesional shear force	N
F_P	Impact pressure force	N

F_p	Pulling strength of a root	N
F_p	Upward dynamic pressure force	N
F_t	Tensile force	N
F_w	Submerged weight of the soil	N
F_{crack}	Bearable force of a soil crack	N
f_{load}	Correctional load factor	–
F_{vb}	Absorbing boundary force	N
G	Shear modulus	Pa
g	Gravitational constant	m/s^2
h	Flow depth / wave thickness	m
H_{m0}	Significant wave height	m
K	Compression/Bulk modulus	Pa
k_l	Wave overtopping parameter	–
k_n	Spring coefficient in normal direction	–
k_s	Hydraulic conductivity of soil	m/s
L	Length of a crack	m
l	Length of a side of a turf element	m
N	Shape function	–
n	Manning roughness coefficient	$s/m^{1/3}$
n	Number of oscillating component Fourier series	–
n	Soil porosity (≈ 0.4)	–
n_r	number of roots	–
O	Order of magnitude	N/m^2
P	Bearable impact pressure pressure	N/m^2
P	Pressure impulse	Ns/m^2
p	Water pressure or total pressure	N/m^2

p_m	Maximum pressure fluctuation	N/m^2
p_{max}	Maximum impulse pressure	N/m^2
q	Specific discharge	m^2/s
R	Vertical distance above the mean water level	m
r_0	Depth averaged relative turbulence intensity	$-$
r_s	Radius sample area	m
S	Area absorbing boundary	m^2
S	Stress along shear plane	N/m^2
s	Exponential shape parameter	m
s_b	Distance along the slope	m
S_{bed}	Slope of the bed	$-$
t	Loading time for settlement calculation	$days$
t	Time	s
t	Wave overtopping parameter	$-$
T_0	Total wave duration	s
T_R	Tensile strength of a root	$-$
$T_{m-1,0}$	Significant wave period	m
U	Flow velocity	m/s
u	Flow velocity in x-direction	m/s
u	Soil displacement	m
u_*	Bed shear velocity	m/s
U_0	Depth averaged flow velocity	m/s
u_{imp}	Impact flow velocity of an overtopping wave	m/s
V	Volume of soil	m^3
v	Flow velocity	m/s
V_R	Volume of roots in the soil	m^3

W	Resisting force of a crack	N
w_p	Average velocity of soil particle in soil deformation	m/s
w_w	Average velocity of pore water in soil deformation	m/s
x	Longitudinal coordinate	m
z	Vertical coordinate	m
Z_{wave}	Vertical location of wave impact w.r.t. crest	m

Greek symbols

α	Angle of a shear plane of a crack	$^\circ$
α	Bottom slope angle of a soil slice of a slip circle	$^\circ$
α	Rotation angle for which the soil stress state exists of normal stresses only	$^\circ$
α_0	Turbulence coefficient	–
α_M	Load factor	–
α_n	Factor for dashpot coefficient in normal direction	–
α_s	Factor for dashpot coefficient in tangential direction	–
α_τ	Turbulence coefficient of Emmerling (≈ 18)	–
β	Impact angle bottom layer overtopping wave w.r.t. slope	$^\circ$
β_f	Compressibility of fluid	$^\circ$
χ	Longitudinal coordinate in coordinate system oriented to the slope	m
Δ	Change of unit	–
δ	Virtual sublayer thickness	m
η_a	Air concentration	–
γ	Specific weightr	N/m^3
γ_β	Influence factor for oblique wave attack	–
γ_b	Influence factor for berms	–
γ_f	Influence factor for slope roughness	–
λ	First Lamé parameter	–

μ	Second Lamé parameter	–
ν	Poisson's ratio	–
ϕ	Angle of repose (=internal friction angle)	$^\circ$
ϕ	Impact angle surface layer overtopping wave w.r.t. slope	$^\circ$
ρ	Density	kg/m^3
ρ_p	Particle density	kg/m^3
Σ	Summation	–
σ	Normal stress or normal strength	N/m^2
σ'	Effective normal stress	N/m^2
σ'_1	Effective major principle stress	N/m^2
σ'_3	Effective minor principle stress	N/m^2
σ_l	Stress before loading	N/m^2
σ_u	Longitudinal turbulence intensity	–
σ_{bot}	Normal stress on absorbing boundary	N/m^2
$\sigma_{dashpot}$	Reaction stress from absorbing boundary, acting dashpot alike	N/m^2
σ_{grass}	Normal strength of grass	N/m^2
σ_{spring}	Reaction stress from absorbing boundary, acting spring alike	N/m^2
τ	Shear stress or shear strength	N/m^2
τ	Truncation error	N/m^2
τ'	Effective shear stress or shear strength	N/m^2
τ_0	Mean bed shear stress	N/m^2
τ_r	Accumulated tensile strength of roots	N/m^2
τ_{grass}	Shear strength of grass	N/m^2
θ	Angle between jet and impact plane	$^\circ$
θ	Root angle of shear rotation	$^\circ$
θ	Slope angle	$^\circ$

ε	Strain	–
$\xi_{m-1,0}$	Breaker parameter	–
ζ	Vertical coordinate in coordinate system oriented to the slope	m

Other symbols

∇	3-dimensional vector differential operator

Subscripts

2%	Value reached by 2% of incoming waves	–
$\chi\zeta$	Acting on plane normal to χ, in the direction of ζ	
χ	Longitudinal coordinate in coordinate system oriented to the slope	
$\zeta\zeta$	Acting on plane normal to ζ, in the direction of ζ	
ζ	Vertical coordinate in coordinate system oriented to the slope	
b	Value at the slope	
$b, 0$	Value at the start of the slope	
c	Critical value	
c	Value at dike crest	
$crest$	Value at dike crest	
i	Index, representing different unit	
i	Value at current spatial step in x-direction	
j	Value at current spatial step in y-direction	
max	Maximum value	
min	Minimum value	
p	Concerning soil particles	
s	Concerning soil	
w	Concerning water	
x	Value in x-direction	
xx	Acting on plane normal to x, in the direction of x	

xy	Acting on plane normal to x, in the direction of y
xz	Acting on plane normal to x, in the direction of z
yx	Acting on plane normal to y, in the direction of x
yy	Acting on plane normal to y, in the direction of y
yz	Acting on plane normal to y, in the direction of z
z	Value in z-direction
zx	Acting on plane normal to z, in the direction of x
zy	Acting on plane normal to z, in the direction of y
zz	Acting on plane normal to z, in the direction of z

Superscripts

n	Value at current time step

References

M. M. Abood, B. Yusuf, T. A. Mohammed, and A. H. Ghazali. Manning roughness coefficient for grass-lined channel. *Suranaree Journal of Scientific Technology*, 13(4): 317–330, 2006.

I. K. J. Al-Kafaji. *Formulation of a Dynamic Material Point Method (MPM) for Geomechanical Problems*. PhD thesis, Institut für Geotechnik der Universität Stuttgart, 2013.

M. L. Albertson, Y. B. Dai, R. A. Jensen, and H. Rouse. Diffusion of Subermerged Jets. *Transactions of the American Society of Civil Engineers*, pages 639–664, 1950.

A. M. Ansal and A. Erken. Undrained Behavior of Clay under Cyclic Shear Stresses. *Journal of Geotechnical Engineering*, 115(7):968–983, 1989.

A. K. Ashmawy, R. Salgado, S. Guha, and V. P. Drnevich. Soil Damping and Its Use in Dynamic Analyses. In *Proceedings: Third International Conference on Recent Advances in Geotechnical Earthquake Engineering and Soil Dynamics.*, number 9, pages 35–41. Missouri University of Science and Technology, 1995.

J. H. Atkinson. Non-linear soil stiffness in routine design. *Géotechnique*, 50(5):487–508, 2000. doi: 10.1680/geot.2000.50.5.487.

J. J. Bakker and R. J. C. Mom. Factual report overslagproef Wijmeers 2. Technical report, INFRAM B.V., 2015.

J. J. Bakker, R. J. C. Mom, and G. J. Steendam. Factual Report. Golfoverslagproeven Zeeuwse zeedijken. Technical report, INFRAM B.V., 2008.

J. J. Bakker, R. J. C. Mom, G. J. Steendam, and J. W. van der Meer. Factual Report. Overslagproeven en oploopproef Tholen. Technical report, INFRAM B.V., 2011.

BAW. Merkblatt standsicherheit von dämmen an bundeswasserstraßen. Technical report, Bundes Anstalt für Wasserbau, 2005.

J. Bear. *Dynamics of Fluids in Porous Media*. Dover Publications Inc., New York, 1972.

A. Bellin and V. Fiorotto. Direct Dynamic Force Measurement on Slabs in Spillway Stilling Basins. *Journal of Hydraulic Engineering*, 121(10):686–693, 1995. doi: 10.1061/(ASCE)0733-9429(1995)121:10(686).

R. W. Bijlard. Strength of the grass sod on dikes during wave overtopping. Master's thesis, Delft University of Technology, 2015.

R. W. Bijlard, G. J. Steendam, H. J. Verhagen, and J. W. van der Meer. Determining the

critical velocity of grass sods for wave overtopping by a grass pulling device. In *Coastal Engingeering Proceedings*, volume 1, 2017. doi: 10.9753/icce.v35.structures.20.

A. W. Bishop. The use of the Slip Circle in the Stability Analysis of Slopes. *Géotechnique*, 5(7), 1955. doi: 10.1680/geot.1955.5.1.7.

A. W. Bishop and G. Eldin. Undrained Triaxial Tests on Saturated Sands and Their Significance in the General Theory of Shear Strength. *Géotechnique*, 2(1):13–32, 1950. doi: 10.1680/geot.1950.2.1.13.

F. Bles, K. Arbad, P. Beerling, C. de Boer, E. Steenbergen, K. van der Lugt, L. Wentholt, H. van Hemert, and R. Biemans. *Leidraad toetsen op veiligheid regionale waterkeringen. Module introductie met bijlagen.* STOWA, 2015.

I. A. Bolotnov, R. T. Lahey, D. A. Drew, K. E. Jansen, and A. A. Oberai. Spectral analysis of turbulence based on the DNS of a channel flow. *Computers and Fluids*, 39: 640–655, 2010. doi: 10.1016/j.compfluid.2009.11.001.

A. Bomers, J. P. Aguilar, J. J. Warmink, and S. J. M. H. Hulscher. Modelling erosion development during wave overtopping of an asphalt road covered dike. In *FLOODrisk 2016 - 3rd European Conference on Flood Risk Management*, volume 7. E3S Web of Conferences, 2016. doi: 10.1051/e3sconf/20160703003.

R. B. J. Brinkgreve, S. Kumarswamy, W. M. Swolfs, and F. Foria. *PLAXIS 2D Scientific Manual 2018.* Plaxis B.V., 2018.

W. R. Buessem and B. Nagy. The Mechanism of the Deformation of Clay. *Clays and Clay Minerals*, 2(1):480–491, 1953. doi: 10.1346/CCMN.1953.0020138.

Cambridge University. Material Selection Charts. http://www-materials.eng.cam.ac.uk/mpsite/interactive_charts/stiffness-density/NS6Chart.html, 2002.

A. Casagrande. Research on the Atterberg Limits of Soils. *Public Roads*, 12(3):121–136, 1932.

A. Casagrande. The Determination of the Pre-Consolidation Load and Its Practical Significance. In *Proceedings of the 1st International Conference on Soil Mechanics*, volume 3. ASCE, 1936.

H. Chanson. *Hydraulics of Open Channel Flow: An Introduction.* Elsevier Butterworth-Heinemann, 2nd edition, 2004.

G. Chavent and J. Jaffré. Mathematical Models and Finite Elements for Reservoir Simulation. *Studies in Mathematics and Its Applications*, 17, 1986.

A. H. D. Cheng and D. T. Cheng. Heritage and early history of the boundary element method. *Engineering Analysis with Boundary Elements*, 29:268–302, 2005. doi: 10.1016/j.enganabound.2004.12.001.

C. Cherubini, S. Filippi, A. Gizzi, and M. G. C. Nestola. On the Wall Shear Stress Gradient in Fluid Dynamics. *Communications in Computational Physics*, 17(3):808–821, 2015. doi: 10.4208/cicp.030714.101014a.

V. T. Chow. *Open-channel hydraulics*. McGraw-Hill, New York, 1959.

G. Christakos. Soil behaviour under dynamic loading conditions: experimental procedures and statistical trends. *Stochastic Environmental Research and Risk Assessment*, 17:175–190, 2003. doi: 10.1007/s00477-003-0132-x.

R. V. Churchill. *Operational Mathematics*. McGraw-Hill Book Company Inc., 3rd edition, 1972.

CIESIN, IFPRI, and CIAT. Global Rural-Urban Mapping Project, Version 1 (GRUMPv1): Population Count Grid, 2011.

C. F. Colebrook and C. M. White. Experiments with Fluid Friction in Roughened Pipes. In *Proceedings of the Royal Society of London. Series A, Mathematical and Physical Sciences.*, pages 367–381, 1937.

A. Collison and A. Simon. Modeling gully head-cut recession processes in loess deposits. In *Soil Erosion Research for the 21st Century, Proceedings of the International Symposium, Honolulu.*, pages 87–90, 2001. doi: 10.13031/2013.3209.

M. J. Cooker and D. H. Peregrine. Pressure-impulse theory for liquid impact problems. *Journal of Fluid Mechanics*, 297:193–214, 1995. doi: 10.1017/S0022112095003053.

N. J. Coppin and I. G. Richards. *Use of vegetation in civil engineering*. CIRIA, 2nd edition, 2007.

C. A. Coulomb. *Essai sur une application des règles de maximis & minimis à quelques problèmes de statique, relatifs à l'architecture*. De l'Imprimerie Royale, 1776.

G. Cuomo, G. Lupoi, K. ihiro Shimosako, and S. Takahashi. Dynamic response and sliding distance of composite breakwaters under breaking and non-breaking wave attack. *Coastal Engineering*, 58(10):953–969, 2011. doi: 10.1016/j.coastaleng.2011.03.008.

H. Darcy. *Les fontaines publiques de la ville de Dijon*. Dalmont, Paris, 1856.

H. Darcy. *Recherches Experimentales Relatives au Mouvement de L'Eau dans les Tuyaux*. Mallet-Bachelier, Paris, 2nd edition, 1857.

B. Dargahi. The turbulent flow field around a circular cylinder. *Experiments in Fluids*, 8(1,2):1–12, 1989.

M. de Visser. Voorlopige werkwijze macrostabiliteit i.c.m. golfoverslag OI2014v4. Technical report, Kennisplatform Risicobenadering, 2017.

M. de Wit, H. Buiteveld, W. van Deursen, F. Keller, and J. Bessembinder. Klimaatverandering en de afvoer van Rijn en Maas. *Stromingen*, 14(1):13–24, 2008. doi: 10.3208/sandf1972.22.3_77.

R. G. Dean, J. D. Rosati, T. L. Walton, and B. L. Edged. Erosional equivalences of levees: Steady and intermittent wave overtopping. *Ocean Engineering*, 37(1):104–113, 2010. doi: 10.1016/j.oceaneng.2009.07.016.

C. d'Eliso. *Breaching of sea dikes initiated by wave overtopping*. PhD thesis, University of Florence and University of Braunschweig, 2007.

D-Geo Stability. Slope stability software for soft soil engineering. Deltares, 16.2 edition, 2016.

A. Egger. Method of Finite Elements I: Shape Functions. https://www.ethz.ch/content/dam/ethz/special-interest/baug/ibk/structural-mechanics-dam/education/, 2015. Swiss Federal Institute of Technology Zürich.

H. Elsafti. *Modelling and Analysis of Wave-Structure-Foundation Interaction for Monolithic Breakwaters*. PhD thesis, Technischen Universität Carolo-Wilhelmina zu Braunschweig, 2015.

A. Emmerling. Die momentane Struktur des Wanddruckes einer turbulenten Grenzschichtströmung. *Max-Planck-Institut für Strömungsforschung und AVA Göttingen*, 1973.

A. Führböter. Der druckschlag durch brecher auf deichböschungen. Technical report, Mitteilungen des Franzius-Instituts für Grund- und Wasserbau der Technischen Universität Hannover, 1966.

F. J. H. Gijsen, A. M. Goijaerts, F. N. van de Vosse, and J. D. Janssen. A new method to determine wall shear stress distribution. *Journal of Rheology*, 41(5):995–1006, 1997. doi: 10.1122/1.550818.

H. Q. Golder and A. W. Skempton. The angle of shearing resistance in cohesive soils for tests at constant water content. In *Proceedings of the 2nd International Conference on Soil Mechanics and Foundation Engineering*, volume 1, pages 185–192, 1948.

W. H. Graf. *Fluvial Hydraulics, Flow and transport processes in channels of simple geometry.* Wiley and Sons, New York, 1998.

W. H. Green and G. A. Ampt. Studies on soil physics. *The Journal of Agricultural Science*, 4(1):1–24, 1911. doi: 10.1017/S0021859600001441.

G. Greeuw. Dynamic load tests on two sods from Millingen. Technical report, Deltares, 2013.

D. V. Griffiths. *Visco-plastic behaviour of geomaterials, Coupled analyses in geomechanics (eds. N. D. Cristescu and G. Gioda).* Springer-Verlag., New York, 1994.

K. Hähne. *Der Einflußvon Gräser- und Gehölzwurzeln auf die Scherfestigkeit von Böden und damit auf die Scherfestigkeit von Hängen und Böschungen,.* PhD thesis, TU Berlin, Fachbereich Landschaftsentwicklung, 1991.

M. R. Hendriks. *Introduction to Physical Hydrology.* Oxford University Press Inc., New York, 1st edition, 2010.

J. Hinkel, D. Lincke, A. T. Vafeidis, M. Perrette, R. J. Nicholls, R. S. J. Tol, B. Marzeion, X. Fettweis, C. Ionescu, and A. Levermann. Coastal flood damage and adaptation costs under 21st century sea-level rise. *PNAS*, 111(9):3292–3297, 2014.

G. J. C. M. Hoffmans. *The Influence of Turbulence on Soil Erosion.* Deltares Select Series. Eburon Academic Publishers, 2012.

G. J. C. M. Hoffmans, G. Akkerman, H. Verheij, A. van Hoven, and J. W. van der Meer. The erodibility of grassed inner dike slopes against wave overtopping. In *Proceedings of the 31st International Conference on Coastal Engineering, Hamburg, Germany*. ASCE, 2008. doi: 10.1142/9789814277426_0267.

B. Hofland. Impulsive loads of steep bore impact on a vertical wall. theoretical derivations, n.d.

P. Hölscher. Soil dynamics in urban areas, 2016.

S. A. Hughes. Adaptation of the Levee Erosional Equivalence Method for the Hurricane Storm Damage Risk Reduction System (HSDRRS). Technical Report May, US Army Corps of Engineers, 2011.

S. A. Hughes, C. Thornton, J. W. van der Meer, and B. Scholl. Improvements in describing wave overtopping processes. *Coastal Engineering*, 2012.

R. K. Jain and U. C. Kothyari. Cohesion influences on erosion and bed load transport. *Water Resourches Research*, 45, 2009. doi: 10.1029/2008WR007044.

J. Jimènez. The physics of wall turbulence. *Physica A: Statistical Mechanics and its Applications*, 263(1-4):252–262, 1999. doi: 10.1016/S0378-4371(98)00507-X.

J. Kerman-Nejad, M. Fathi-Moghadam, B. Lashkarara, and S. Haghighipour. Dynamic Pressure of Flip Bucket Jets. *World Applied Sciences Journal*, 12(9):1448–1454, 2011.

C. Keutner. Flow over a broad-crested weir or entrance structure. *Bauingenieur*, 15: 366–371, 1934.

A. S. Keverling Buisman. *Grondmechanica*. Waltman, 1941.

A. Kezdi. *Handbook of soil mechanics*. Elsevier, Amsterdam, 1974. Translation of: 'Handbuch der Bodenmechanik'.

M. Kok, J. K. Vrijling, and C. Zevenbergen. Towards an integrated evaluation framework for Multi-Functional Flood Defences. In *2nd European Conference on Flood Risk Management, FLOODrisk2012, Rotterdam, the Netherlands*, pages 921–926, 2013. doi: 10.1201/b13715-134.

A. W. Koppejan. A formula combining the Terzaghi load compression relationship and the Buisman secular time effect. In *Proceedings of the 2nd International Conference on Soil Mechanics and Foundation Engineering, Rotterdam*, volume 3, pages 32–38. ASCE, 1948.

A. Kortenhaus. *Probabilistische Methoden für Nordseedeiche*. PhD thesis, Technischen Universität Carolo-Wilhelmina zu Braunschweig, 2003.

D. P. Kroese, T. Brereton, T. Taimre, and Z. I. Botev. Why the Monte Carlo method is soimportant today. *WIREs Comput Stat*, 6:386–392, 2014. doi: 10.1002/wics.1314.

W. Kuijken. Deltaprogramma 2015, werk aan de delta. Technical report, Ministerie van Infrastructuur en Milieu en Ministerie van Economische Zaken, 2015.

M. Lamandé, T. Keller, F. Berisso, M. Stettler, and P. Schjonning. Accuracy of soil

stress measurements as affected by transducer dimensions and shape. *Soil and Tillage Research*, 145:72–77, 2015. doi: 10.1016/j.still.2014.08.011.

M. Lloret-Cabot, S. J. Wheeler, J. A. Pineda, E. Romero, and D. Sheng. From saturated to unsaturated conditions and vice versa. *Acta Geotechnica*, 13(1):15–37, 2018. doi: 10.1007/s11440-017-0577-6.

J. Lysmer and R. L. Kuhlmeyer. Finite dynamic model for infinite media. *Journal of the Engineering Mechanics Division*, 95:859–878, 1969.

R. Manning. On the flow of water in open channels and pipes. *Transactions of theInstitution of Civil Engineers of Ireland*, 20:161–207, 1891.

G. Mavko, T. Mukerji, and J. Dvorkin. *The Rock Physics Handbook*. Cambridge Universiy Press, 2nd edition, 2009. doi: 10.1017/CBO9780511626753.

J. L. Merkens, L. Reimann, J. Hinkel, and A. T. Vafeidis. Gridded population projections for the coastal zone under the Shared Socioeconomic Pathways. *Global and Planetary Change*, 145:57–66, 2016. doi: 10.1016/j.gloplacha.2016.08.009.

J. K. Mitchell. *Fundamentals of soil behavior*. John Wiley & Sons Inc., New York, 2nd edition, 1993.

O. Mohr. Welch Umsttinde bedingen die Elastizitltsgrenze und den Bruch eines Materials? . *Zeitschrift Verein Deutsch Iwenieur*, 44:1524–1530; 1572–1577, 1900.

W. D. Moss. Flow separation at the upstream edge of a square-edged broad-crested weir. *Journal of Fluid Mechanics*, 52(2):307–320, 1972. doi: 10.1017/S0022112072001430.

J. A. Muijs. *Grass cover as a dike revetment (Translation of TAW-brochure "Grasmat als Dijkbekleding" 9)*. Ministry of Public Works and Water Management, 1999.

NEN. *NEN-EN 1997-2:2007 en Eurocode 7: Geotechnisch ontwerp - Deel 2: Grondonderzoek en beproeving*. Nederlands Normalisatie Instituut, 2007.

B. C. O´Kelly. Atterberg Limits and Remolded Shear Strength—Water Content Relationships. *Geotechnical Testing Journal*, 36(6):939–947, 2013. doi: 10.1520/GTJ20130012.

H. Pan, G. Chen, and T. Sun. Experimental Research on Dynamic Poisson's Ratio of Silty Clay. *Advanced Materials Research*, 168-170:286–292, 2010. doi: 10.4028/www.scientific.net/AMR.168-170.286.

A. Patel, R. Ingale, and K. B. Bhanarkar. Effect of Compaction States and the Confining Pressure on Poisson's Ratio of Stratified and Non-Stratified Soils. *Arabian Journal for Science and Engineering*, 2017. doi: 10.1007/s13369-017-2846-y.

P. Peeters, L. de Vos, B. Vandevoorde, E. Taveniers, and F. Mostaert. Erosiebestendigheid van de grasmat bij golfoverslag: Golfoverslagproeven Tielrodebroek. Technical report, Waterbouwkundig Laboratorium, INBO en afdeling Geotechniek, 2012.

D. J. Pickering. Anisotropic elastic parameters for soil. *Geotechnique*, 20:271–276, 1970. doi: 10.1680/geot.1970.20.3.271.

L. A. Ponsioen. Overflow and wave overtopping induced failure processes on the land-side slope of a dike. Master's thesis, Delft University of Technology, 2016.

L. A. Ponsioen, M. van Damme, P. Peeters, and B. Hofland. Relating grass failure on the landside slope to wave overtopping induced excess normal stresses. preprint submitted to Coastal Engineering, November 2017, 2017.

M. Prat, E. Bisch, A. Millard, P. Mestat, and G. Cabot. *La modelisation des ouvrages.* AFPC - Emploi des éléments finis en génie civil. Hermes, Paris, 1995.

A. S. Ramamurthy and N.-D. Vo. Characteristics of Circular-Crested Weir. *Journal of Hydraulic Engineering*, 119(9):1055–1062, 1993.

M. H. T. Rayhani and M. H. El-Naggar. Dynamic Properties of Soft Clay and Loose Sand from Seismic Centrifuge Tests. *Geotechnical and Geological Engineering*, 2008. doi: 10.1007/s10706-008-9192-5.

W. Richwien. Die widerstandsfähigkeit von deichen beim wellenüberlauf und die entwicklung von deichbrüchen - eine bestandsaufnahme. Technical report, Essen, 2003.

Rijkswaterstaat. Handreiking ontwerpen met overstromingskansen. Veiligheidsfactoren en belastingen bij nieuwe overstromingskans-normen. Technical report, Ministerie van Infrastructuur en Milieu, 2017.

K. H. Roscoe. An Apparatus for the Application of Simple Shear to Soil Samples. In *Proceedings third ICSMFE*, volume 1, pages 186–191, 1953.

K. H. Roscoe, A. N. Schofield, and C. P. Wroth. On the Yielding of Soils. *Géotechnique*, 8:22–53, 1958. doi: 10.1680/geot.1958.8.1.22.

H. Rouse. Evaluation of boundary roughness. In *Proceedings Second Hydraulic Conference, University of Iowa Bulletin*, volume 27, 1943.

G. J. Schiereck and H. J. Verhagen. *Introduction to bed, bank and shore protection.* Delft Academic Press, 2nd edition, 2016.

A. N. Schofield and C. P. Wroth. *Critical State Soil Mechanics.* McGraw-Hill, 1st edition, 1968.

M. H. Schultz van Haegen. Besluit tot regeling veiligheid primaire waterkeringen 2017. *Staatscourant*, 65697, 2016.

H. Schüttrumpf and H. Oumeraci. Layer thicknesses and velocities of wave overtopping flow at seadikes. *Coastal Engineering*, 52:473–495, 2005. doi: 10.1016/j.coastaleng.2005.02.002.

H. Schüttrumpf and M. R. A. van Gent. Wave overtopping at seadikes. In *Proceedings of Coastal Structures, Portland, USA*, pages 431–443. ASCE, 2003. doi: 10.1061/40733(147)36.

N. Slootjes and H. van der Most. Achtergronden bij de normering van de primaire waterkeringen in Nederland. Technical report, Ministerie van Infrastructuur en Milieu, 2016.

D. M. J. Smeulders. *On wave propagation in saturated and partially saturated porous media*. PhD thesis, Eindhoven University of Technology, 1992.

J. Sprangers. *Vegetation dynamics and erosion resistance of seadyke grassland*. PhD thesis, Wageningen Agricultural University, 1999.

G. Stanczak, H. Oumeraci, and A. Kortenhaus. Laboratory tests on the erosion of clay revetment of sea dike with and without a grass cover induced by breaking wave impact. Technical report, HR Wallingford, UK, 2007.

G. Stanczak, H. Oumeraci, and A. Kortenhaus. Breaching of sead dikes initiated by breaking wave impacts. Technical report, HR Wellingford, 2008.

G. J. Steendam, J. W. van der Meer, H. Verhaeghe, P. Besley, L. Franco, and M. R. A. van Gent. The international database on wave overtopping. In *Proceedings International Conference on Coastal Engineering, Lisbon*. ASCE, 2004.

G. J. Steendam, A. van Hoven, J. W. van der Meer, and G. Hoffmans. Wave overtopping simulator test on transitions and obstacles at grass covered slopes of dikes. In *Proceedings International Conference on Coastal Engineering, Seoul*. ASCE, 2014.

J. Stróżyk and M. Tankiewicz. The Undrained Shear Strength of Overconsolidated Clays. *Procedia Engineering*, 91:317–321, 2014. doi: 10.1016/j.proeng.2014.12.067.

E. Sun, X. Zhang, Z. Li, and Y. Wang. Tailings Dam Flood Overtopping Failure Evolution Pattern. *Procedia Engineering*, 28:356–362, 2012. doi: 10.1016/j.proeng.2012.01.733.

K. Suzuki and S. Takahashi. Liquefaction of Loosely Deposited Sandbed Behind a Breakwater due to Wave Overtopping. In *Proceedings Conference Coastal Structures, Portland, Oregon*. ASCE, 2003. doi: 10.1061/40733(147)54.

R. 't Hart, H. de Bruijn, and G. de Vries. Fenomenologische beschrijving. faalmechanismen wti. Technical report, Deltares, 2016.

S. Tan. *Dynamic Finite Element Investigation of Wave Attack on Sea Dikes, A Coupled Approach using Plate and Volume Elements*. PhD thesis, Delft University of Technology, 2016.

TAW. Clay for dikes, technical advisory committee on water retaining structures. Technical report, Ministry of Public Works and Water Management, 1996a.

TAW. Flooding risk The Netherlands, technical advisory committee on water retaining structures. Technical report, Ministry of Public Works and Water Management, 1996b.

TAW. Fundamentals on Water Defences. Technical report, Ministry of Public Works and Water Management, 1998.

TAW. Technisch Rapport Waterkerende Grondconstructies. Geotechnische aspecten van dijken, dammen en boezemkaden. Technical report, Ministerie van Verkeer en Waterstaat, 2001.

K. Terzaghi. Tragfähigkeit der flachgründungen. In *IVBH Kongressbericht*. ETH Zürich, 1932. doi: 10.5169/seals-478.

K. Terzaghi. Simple tests determine hydrostatic uplift. *Engineering News-Record*, 116 (25):872–875, 1936.

K. Terzaghi. *Theoretical Soil Mechanics*. John Wiley & Sons Inc., New York, 1940.

L. H. Trung and H. J. Verhagen. Damage to grass covered slopes due to overtopping. In *Coastal Engineering Proceedings*, 2014. doi: 10.9753/icce.v34.structures.9.

C. V. Tu and D. H. Wood. Wall pressure and shear stress measurements beneath an impinging jet. *Experimental Thermal and Fluid Science*, 13(4):364–373, 1996. doi: 10.1016/S0894-1777(96)00093-3.

A. Valk. Wave overtopping. Impact of water jets on grassed inner slope transitions. Master's thesis, Delft University of Technology, 2009.

S. van Baars and I. van Kempen. The Causes and Mechanisms of Historical Dike Failures in the Netherlands. *E-WAter*, 2009.

M. van Damme. Distributions for wave overtopping parameters for stress strength analyses on flood embankments. *Coastal Engineering*, 116:195–206, 2016.

M. van Damme. Distinction water pressures and effective stresses. theoretical derivations, 2018a.

M. van Damme, 2018b. Personal correspondence with Myron van Damme, d.d. 19 February 2018.

M. van Damme, L. Ponsioen, M. H. Huerta, and P. Peeters. Comparing overflow and wave-overtopping induced breach initiation mechanisms in an embankment breach experiment. In *Flood Risk 2016: 3rd European Conference on Flood Risk Management, Lyon, France*, E3S Web of Conferences, volume 7. EDP Science, 2016. doi: 10.1051/e3sconf/20160703004.

M. van Damme, P. Peeters, and L. Ponsioen. Wave and overflow induced grass cover failure experiment at Wijmeers., 2017.

J. G. M. van der Grinten. *An experimental study of shock-induced wave propagation in dry, water-saturated, and partially saturated porous media*. PhD thesis, Eindhoven University of Technology, 1987.

J. W. van der Meer, H. J. Verheij, J. Lindenberg, A. van Hoven, and G. J. C. M. Hoffmans. Golfoverslag en sterkte binnentaluds van dijken. rapport predictiespoor sbw. Technical report, Sterkte & Belastingen Waterkeringen (SBW), 2007.

J. W. van der Meer, B. Hardeman, G. J. Steendam, H. Schüttrumpf, and H. J. Verheij. Flow depths and velocities at crest and inner slope of a dike, in theory and with the wave overtopping simulator. In *Proceedings International Conference on Coastal Engineering, Shanghai*. ASCE, 2010a.

J. W. van der Meer, H. J. Verheij, and A. van Hoven. SBW Golfoverslag en Sterkte Grasbekleding. Technical report, Deltares, 2010b.

J. W. van der Meer, J. Provoost, and G. J. Steendam. The wave run-up simulator, theory

and first pilot test. In *Proceedings International Conference on Coastal Engineering, Santander*. ASCE, 2012.

J. W. van der Meer, A. van Hoven, M. Paulissen, G. J. Steendam, H. J. Verheij, G. J. C. M. Hoffmans, and G. Kruse. Handreiking dijkbekledingen. deel 5: Grasbekledingen. Technical report, Deltares, 2015.

J. W. van der Meer, N. W. H. Allsop, T. Bruce, J. D. Rouck, A. Kortenhaus, T. Pullen, H. Schüttrumpf, P. Troch, and B. Zanuttigh. *Manual on wave overtopping of sea defences and related structures. An overtopping manual largely based on European research, but for worldwide application*. EurOtop, 2 edition, 2016.

A. van Hoven, B. Hardeman, J. W. van der Meer, and G. J. Steendam. Sliding stability of landward slope clay cover layers of sea dikes subject to wave overtopping. In *Proceedings of the International Conference on Coastal Engineering*, volume 1. ASCE, 2011.

M. T. H. van Vliet, W. H. P. Franssen, J. R. Yearsley, F. Ludwig, I. Haddeland, D. P. Lettenmaier, and P. Kabat. Global river discharge and water temperature under climate change. *Global Environmental Change*, 23(2):450–464, 2013. doi: 10.1016/j.gloenvcha.2012.11.002.

L. Vavrina. Erosion Processes on Dike Slopes. Master's thesis, University of Duisburg-Essen, 2006.

R. Vergouwe. De veiligheid van Nederland in kaart. Technical report, Rijkswaterstaat Projectbureau VNK, 2016.

H. Verhaeghe. CLASH database. http://www.vandermeerconsulting.nl/english/downloads/databases-excel-files/, 2005.

H. J. Verheij, G. J. C. M. Hoffmans, and J. W. van der Meer. Evaluation and Model Development; Grass Erosion Test at the Rhine dike. Technical report, Deltares, 2015.

A. Verruijt. *Soil Dynamics*. Delft University of Technology, 2008.

A. Verruijt and S. van Baars. *Soil Mechanics*. VSSD, 7th, improved edition, 2009.

P. J. Visser. Breach growth in sand-dikes. *Communications on Hydraulic and Geotechnical Engineering*, 98(1):172 pp, 1998.

C. F. Wan and R. Fell. Investigation of Rate of Erosion of Soils in Embankment Dams. *Journal of Geotechnical and Geoenvironmental Engineering*, 130(4):373–380, 2004. doi: 10.1061/(ASCE)1090-0241(2004)130:4(373).

H. Wang. *Theory of linear poroelasticity with applications to geomechanics and hydrogeology*. Princeton University Press, 1st edition, 2000.

E. Winkler. *Die Lehre von der Elasticitaet und Festigkeit mit besonderer Rücksicht auf ihre Anwendung in der Technik : für polytechnische Schulen, Bauakademien, Ingenieure, Maschinenbauer, Architecten, etc.* Dominicus, Prague, 1867.

T. H. Wu, W. P. McKinnell, and D. N. Swanston. Strength of tree roots and landslides

on Prince of Wales Island, Alaska. *Canadian Journal of Geotechnical Research*, 16(1): 19–33, 1979.

K. Yasuhara, T. Yamanouchi, and K. Hirao. Cyclic strength and defromation of normally consolidated clay. *Japanese Society of Soil Mechanics and Foundation Engineering, Soil and Foundations*, 22(3):77–91, 1982. doi: 10.3208/sandf1972.22.3_77.

K. Yasuhara, K. Hirao, and A. F. L. Hyde. Effects of cyclic loading on undrained strength and compressibility of clay. *Japanese Society of Soil Mechanics and Foundation Engineering, Soil and Foundations*, 32(1):100–116, 1992. doi: 10.3208/sandf1972.32.100.

K. Yokota and M. Konno. Dynamic Poisson's Ratio of Soil. In *Proceedings of 7th World Conference Earthquake Engineering Istanbul.*, volume 3, pages 475–478, 1980.

M. J. Young. Wave Overtopping and Grass Cover Layer Failure on the Inner Slope of Dikes. Master's thesis, UNESCO, Institute for Water Education, 2005.

C. E. Zapata. *Uncertainty in soil-water-characteristic curve and impacts on unsaturated shear strength predictions.* PhD thesis, Arizona State University, 1999.

M. Zijlema. *Computational Modelling of Flow and Transport.* Delft University of Technology, 2015.

A

Appendix: Pictures of overtopping simulations

In this appendix pictures are collected of a number of overtopping simulations that have been executed. The pictures show a number of differences in the failures mechanisms. The differences that can be observed from the pictures are described in this appendix.

Location of damage
It appears from simulations that different overtopping situations have a different location of initial damage. Initial failure close to the crest of the dike or at the toe are expected types of failure and most often observed. Figures A.10 and A.13 show examples of initial damage close to the crest of the dike. Figure A.9 shows initial damage at the toe of the dike. Also initial damage somewhere halfway the slope is observed, see Figure A.3. It is even observed that damage initiates at multiple independent locations on the slope. Figure A.11 shows an example where damage initiated at three locations on the slope.

Reason for damage initiation
Regarding the reason for damage overtopping simulations have shown different results. Objects on the slope prove to be often a weak spot. An example of this is the tree that protrudes into the flow in Figure A.13. Another example is the juncture between the soil cover and the stairs that are constructed in the slope surface, shown in Figure A.7.
It appears from simulations that not always expected weak spots are indeed the locations of initial failure. Figure A.8 proves that not always the object is the weakest spot. Here the slope cover has failed at an open area, whereas the slope cover is intact around the fence. The reason for damage on a slope without objects gets not very clear from simulations. Figures A.6 and A.5 show that initial damage, caused by burrowing animals do not have to be normative. Initial unevenness, either a protrusion or a hole, can lead to failure by bulging, as is shown in Figure A.4.

Development of damage
Simulations show differences in the way in which initial damage develops towards large

scale failure. An often observed type of damage development is the deepening of initial damage into a head-cut erosion hole. An example of this is shown in Figure A.14. Other simulations show erosion that develops evenly over a large part of the slope. The damage development into the soil is slow with respect to the development parallel to the slope. This is shown in Figures A.10 and A.1. Also a combination of previous mentioned types of development is observed, see Figure A.13. A third type of damage development is macro instability. Figure A.8 shows a simulation for which a large chunk of soil slipped off.
Another observation from the simulation is the difference in direction of damage development. Development is observed in the direction of the flow and against the direction of the flow. Both are observed for head-cut erosion and for even, shallow erosion. (Note that the development of a slip circle macro instability is always in the same direction.) Simulations where head-cut erosion developed in and against the flow direction are shown in Figures A.14 and A.5 respectively. Simulations where even, shallow erosion developed in and against the flow direction are shown in Figures A.10 and A.1 respectively.

A.1 Afsluitdijk

The picture in this section is obtained from van der Meer et al. [2015].

Figure A.1: ***Afsluitdijk, section 1.*** *Final slope failure after 6 hours simulation with a maximum load of 75 l/s/m overtopping waves. Damage appears as rather even removal of the upper layer, starting at the toe of the dike and developing slope upward, but no hole develops.*

A.2 Boonweg

The pictures in this section are obtained from Bakker et al. [2008].

Figure A.2: ***Boonweg, section 3, initial damage.*** *Slope failure of a saturated grass cover during a simulation, during the second hour of 75 l/s/m overtopping waves. The forcing of the water caused roots to snap, which enabled the formation of a protruding bulge filled with water under the grass cover. During further load the balloon bursted and the grass cover flushed away.*

Figure A.3: ***Boonweg, section 3, final damage.*** *Failed slope after a simulation with a maximum load of 75 l/s/m overtopping waves. Failure started halfway the slope of the dike and developed down the slope.*

Figure A.4: ***Boonweg, section 4.*** *Slope failure during a simulation with a load of 75 l/s/m overtopping waves. Development of a protruding bulge filled with water. Bulge withstood overtopping waves for 5 minutes before bursting.*

A.3 Kattendijke

The picture in this section is obtained from Bakker et al. [2008].

Figure A.5: ***Kattendijke, section 1.*** *Slope failure after 5 hours and 40 minutes simulation with a maximum load of 75 l/s/m overtopping waves. Failure of the maintenance road down the toe of the dike, starting at the side away from the dike and developing towards the dike.*

A.4 Sint Philipsland

The picture in this section is obtained from Bakker et al. [2008].

Figure A.6: ***Sint Philipsland.*** *Slope failure after a simulation with a maximum load of 50 l/s/m overtopping waves (right picture). Failure from the slope of the dike, expected weak spot of a large mole hole remained intact (left picture).*

A.5 Tholen

The pictures in this section are obtained from Bakker et al. [2011].

Figure A.7: ***Tholen, section 2.*** *Slope failure during a simulation, after 1 hour of 5 l/s/m overtopping waves. Clear development of damage in the juncture between the soil cover and the stairs.*

Figure A.8: ***Tholen, section 3.*** *Failed slope after a simulation with a maximum load of 5 l/s/m overtopping waves. Failure shows macro instability: a large chunk of soil has slipped off. It is remarkable that a location at the slope cover was a weaker spot than the objects on the slope.*

Figure A.9: ***Tholen, section 4.*** *Slope failure after a simulation with a maximum load of 30 l/s/m overtopping waves. Failure at the toe of the dike, in the transition from the sloping to flat soil surface.*

A.6 Tielrode

The pictures in this section are obtained from Peeters et al. [2012].

Figure A.10: ***Tielrode, section 1.*** *Slope failure after 35 minutes simulation with a maximum load of 30 l/s/m overtopping waves. Start of failure of the slope cover close to the crest of the dike and developing downwards.*

Figure A.11: ***Tielrode, section 4.*** *Slope failure after 3 hours simulation with a maximum load of 10 l/s/m overtopping waves. Start of failure of the slope cover at multiple locations.*

A.7 Vechtdijk

The pictures in this section are obtained from van der Meer et al. [2015].

Figure A.12: ***Vechtdijk, test 2.*** *Start of failure by heavy erosion around a protruding object.*

Figure A.13: ***Vechtdijk, test 3.*** *Slope failure after incremental development. Damage started close to the crest, developed down slope as removal of grass layer and started to develop as a head-cut erosion at the lower half of the slope.*

A.8 Wijmeers II

The pictures in this section are obtained from Bakker and Mom [2015].

Figure A.14: ***Wijmeers II, section III.*** *Slope failure after 1,5 hours simulation with a maximum load of 25 l/s/m overtopping waves. Failure started as a shallow damage (removal of grass cover over the total length of the slope) and eroded to the core of the dike.*

B

Appendix: Geotechnical resisting mechanisms

This appendix shows multiple approaches to the geotechnical resistance of a grassed dike cover to overtopping load. The different approaches are based on different failure mechanisms. Most approaches consider small scale failure. Since some larger scale sliding is observed as well (see Appendix A), this type of failure is given as well.

B.1 Soil crack strength

The strength of soil under impacting water load is described by Führböter [1966]. He states that an impacting pressure on a water filled soil crack, instantly and fully transfers on the sides of the crack. Note that a water filled soil crack is a valid assumption under overtopping conditions. The transfer of pressure is because the dimensions of the crack are negligible with respect to the speed of a pressure wave in water. Führböter [1966] states that the cohesion is the resisting force for this type of load. This leads to the relation given by Equation B.1. In this equation P_{max} stands for the maximum bearable impacting pressure and c stands for the cohesion of the soil.
With the maximum bearable pressure, the maximum bearable force on the wall of a crack (F_{crack}) is determined. This is done with Equation B.2. In this equation a is the depth of the crack and L is the length of the crack.

$$P_{max} = 2c \tag{B.1}$$

$$F_{crack} = P_{max} a L \tag{B.2}$$

The shear strength of the soil counteracts the impact forces. The result is a failing soil that slides on a shear plane. This shear plane makes angle α with the impact force. This is schematized in Figure B.1. Since the dimensions of a single crack are small, the weight

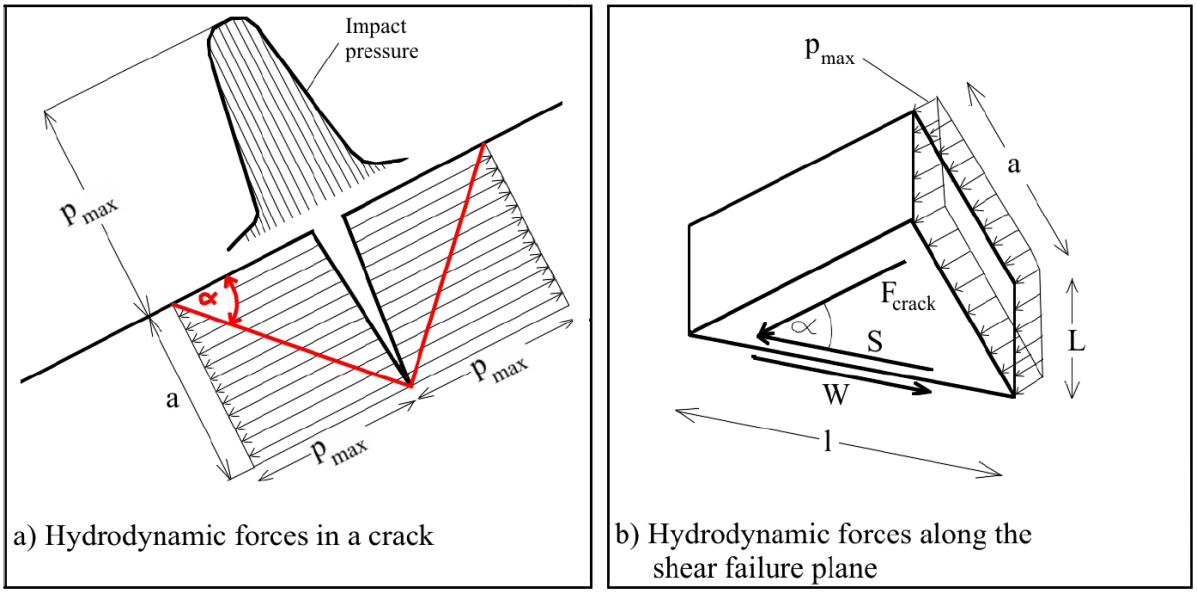

Figure B.1: Model of action of forces for a crack exposed to an impacting pressure (Stanczak et al. [2007])

of the soil body is negligible small compared to the impact forces (Führböter [1966]). The shear stress (S) along the shear plane is given by Equation B.3. The resisting force (W) is given by Equation B.4. In laboratory tests Stanczak et al. [2007] found that considering additional forces on the approach by Führböter [1966] leads to better results.

$$S = aLP_{max} \cos \alpha \tag{B.3}$$

$$W = \frac{aLc}{\sin \alpha} \tag{B.4}$$

Richwien [2003] extended Führböters model by considering forces that where neglected: the weight of the soil (G), the pore water pressure (U) and the soil reaction (Q). Considering these forces changes the total action of the forces, see Figure B.2. For this extended model, no equation exists to determine the maximum impact force that is possible to resist (S_{poss} in the figure). That must be done visually. The maximum resistible impact force is the force that closes the force polygon.

B.2 Pulling force of grass

In literature study Trung and Verhagen [2014] found that grass roots provide the soil cover with an additional cohesion and the ability to resist a pulling force. The root density in the soil decreases with depth. This is described by Sprangers [1999] with the Root Volume Ratio (RVR), see figure B.3. Accordingly, the strength of the soil decreases with the depth.
The accumulated tensile strength at a depth is given by Equation B.5. It is assumed

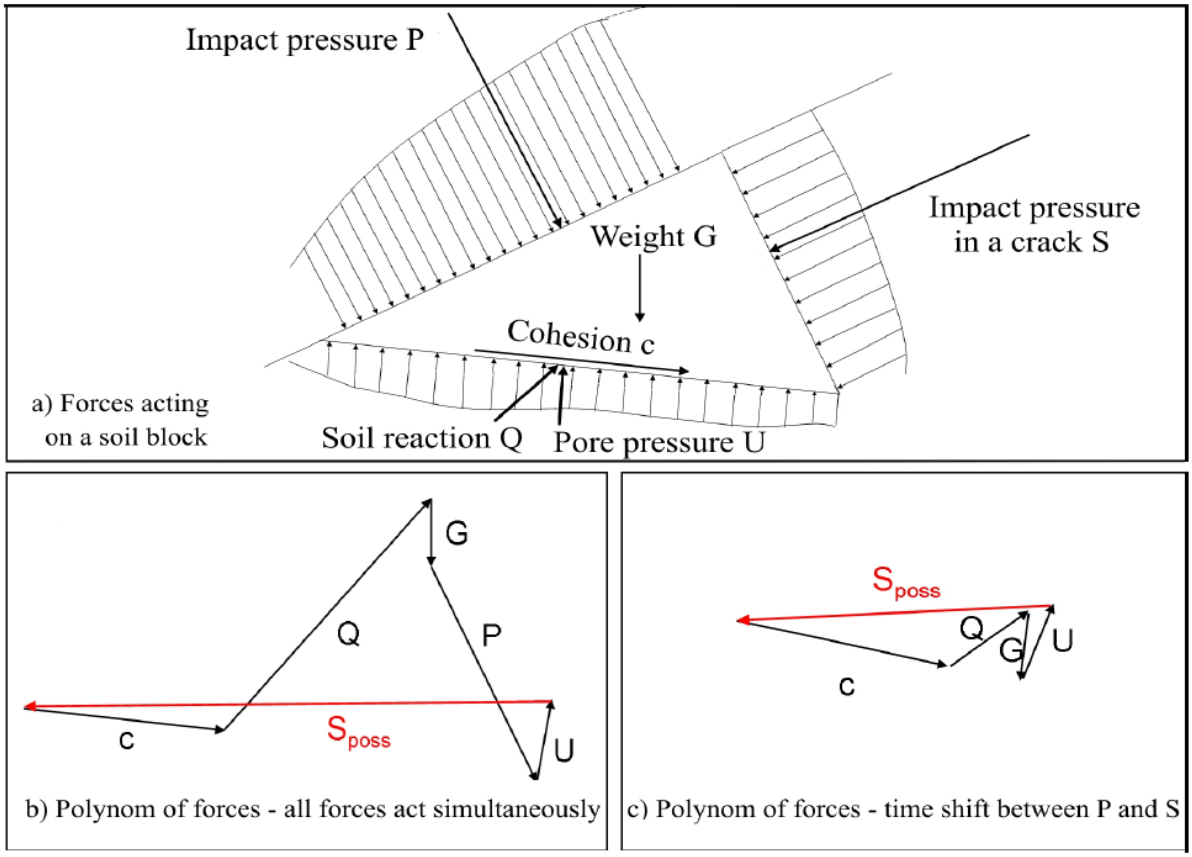

Figure B.2: Extended model of action of forces for a crack exposed to an impacting pressure (Stanczak et al. [2007])

that all roots resist a force simultaneously. In this equation n_r is the number of roots, r_s is the radius of the sample area and F_p is the pulling force that a root can resist.

$$\sum \tau_r = n_r F_p \frac{1}{\pi r_s^2} \tag{B.5}$$

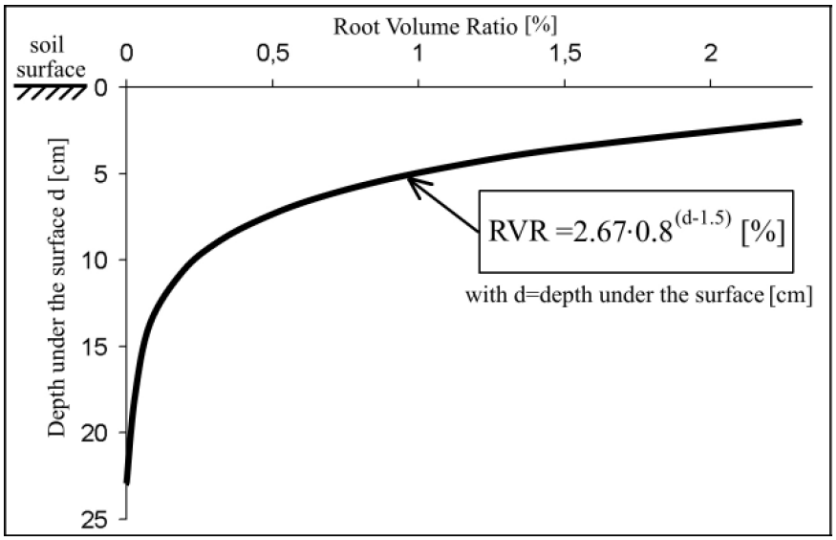

Figure B.3: Root Volume Ratio (RVR) as a function of depth under the surface for dike grass (Sprangers [1999])

B.3 Shear strength, apparent root cohesion

The presence of roots in the soil adds cohesion to the soil. The cohesion added by the presence of roots is called the *apparent root cohesion* (C_R). Its effect is shown in Figure B.4. A way root presence contributes to the apparent root cohesion is by the tensile strength of the roots. This is shown in Figure B.5. According to Wu et al. [1979] it can be calculated by Equation B.6. In this equation T_R is the root tensile strength, $\frac{V_R}{V}$ is the ratio of volume of roots over volume of the soil, θ is the root angle of shear rotation at which a root breaks and ϕ is the internal friction angle of the soil.

$$C_R = T_R \frac{V_R}{V} (\cos\theta \tan\phi + \sin\theta) \tag{B.6}$$

The tensile strength depends on a large number of variables, and can range from 1.3 - 56 MPa (Young [2005]). For *Festuca*, a genus of grass that is used for dike covers, in a saturated soil, Hähne [1991] did tests and determined that the tensile strength is roughly 5 kN/m^2. He included the ratio of the roots over the soil in this value. BAW [2005] states that this value proves local stability only for depths up to 0.2 m. Research on the root angle of shear rotation is very limited, but for grass values close to an upper limit of 70° are suggested (Young [2005]). The ratio of volume of roots over volume of the soil

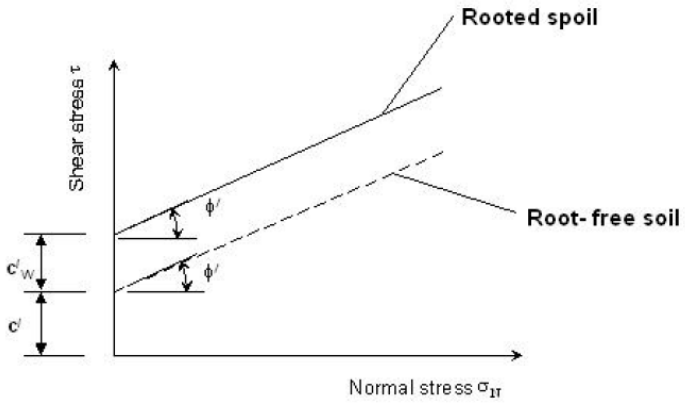

Figure B.4: Apparent root cohesion (Vavrina [2006]).

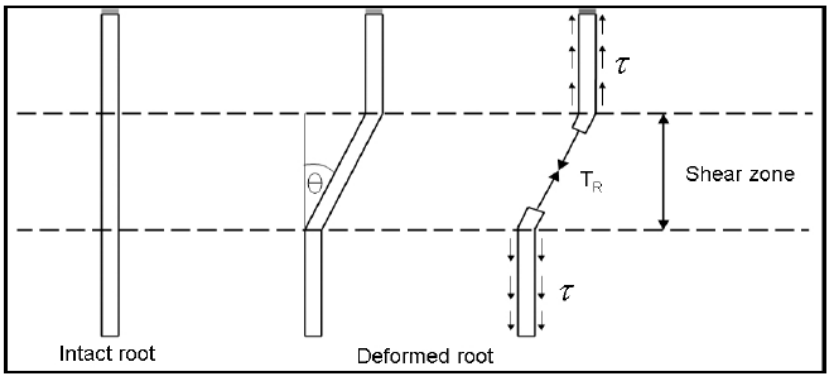

Figure B.5: Principle sketch of flexible elastic perpendicular root reinforcement leading to apparent root cohesion (Wu et al. [1979]).

is depth dependent, see Figure B.3. Results from this method match the results from laboratory tests by Stanczak et al. [2007].

B.4 Slip circle

The model by Bishop [1955] is one of the methods that is developed to determine the resistance against a failure along a slip circle. In this model the stability of a slip circle is determined by dividing the subsurface part of the slipping circle into small slices and determining the forces on each slice. Forces considered are the weight of the soil, the horizontal soil pressure from adjacent slices, normal bearing force of the subsoil and the shear stress along the slip circle. Note that the internal shear resistance that is triggered by deformation of the slipping soil, is not considered. The model is shown in Figure B.6.

The stability of the slip circle is expressed in stability factor F. The resisting forces of the slip circle are larger than the driving forces if $F > 1.0$. In that case the slope can be considered safe. Equation B.7 determines the stability of a slip circle according to Bishops model. This equation contains the following soil parameters: c is the cohesion, γ is the specific weight and ϕ is the angle of repose. Further parameters are the height

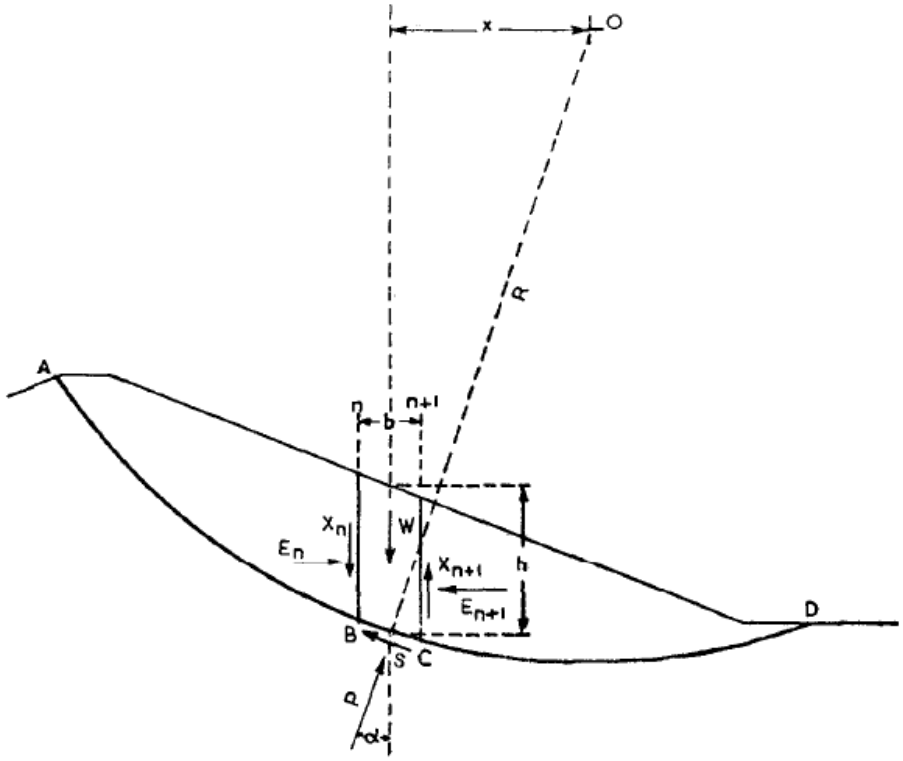

Figure B.6: Slip circle model for stability calculation based on the weight of the soil (W) the normal bearing force (P), the horizontal soil pressures (E_n and E_{n+1}) and the shear stress along the slip circle (S) (Bishop [1955])

of the soil slice h, the pore water pressure p and angle between the slip circle at the base of the soil slide and the horizontal α.

$$F = \frac{\sum \left(\frac{c + (\gamma h - p) \tan \phi}{\cos \alpha (1 + \frac{\tan \alpha \tan \phi}{F})} \right)}{\sum (\gamma h \sin \alpha)} \tag{B.7}$$

According to Verruijt and van Baars [2009] this model is the best method regarding the accuracy of the results with respect to the complexity of the model. Results from the simpler Fellenius' model are less accurate than the results from Bishops model. The results of more extended models hardly deviate from it. Therefore Bishops model is a good approach to the failure of a slope along a slip circle.

B.5 Turf element model

The turf element model is a model by Hoffmans [2012] that describes the equilibrium of forces on a cube of turf (soil with roots) with finite dimensions. The equilibrium of forces is shown in Figure B.7. The model assumes that the loading force is the upward directed dynamic pressure (F_p). The model can be applied on other types of load if the equilibrium of forces is redrafted. All other forces are resisting forces. These are the tensile force at the bottom (F_t), the shear force at four sides that are caused by cohesion (F_c) and the submerged weight of the soil (F_w). The dimensions of the element are given

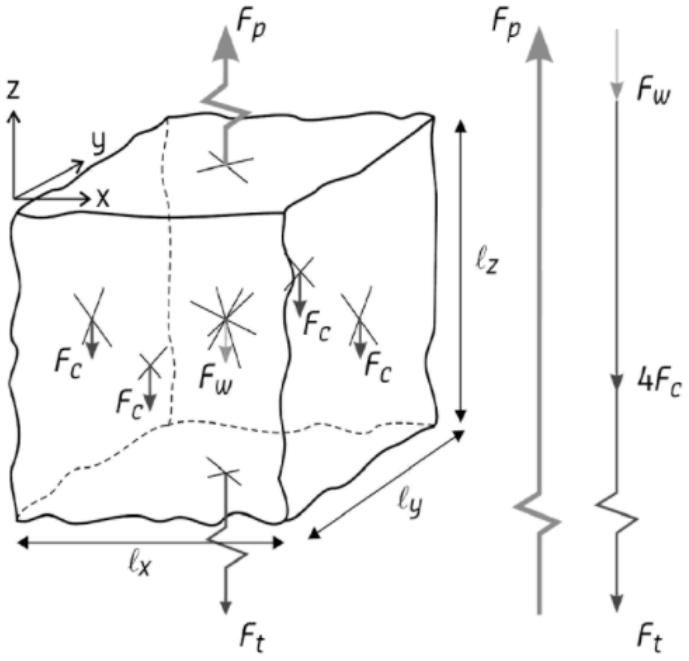

Figure B.7: Forces acting upon a turf element according to the turf element model (Hoffmans [2012])

by l_x, l_y and l_z respectively. Since the element is cubic it holds that $l = l_x = l_y = l_z$. The turf element model states that the soil is stable if the summed resisting force is larger than the summed loading force.

The turf element model provides equations that approach the value of the forces. Based on the assumption that the loading force is caused by the upward dynamic pressure, the loading force is given by Equation B.8. The tensile strength at the bottom of the element is given by Equation B.9. The combined cohesion induced shear strength of the four sides of the element is given by Equation B.10. The submerged weight of the turf element is given by Equation B.11. In these equations $C_{clay,c}$ is the critical rupture strength of clay, $\tau_{grass,c}$ is the critical mean shear strength of grass of the intersected roots per side wall averaged over l_z, $\sigma_{grass,c}$ is the critical normal strength of the intersected grass roots averaged over the bottom of the element, ρ is the water density, ρ_s is the soil density and n (≈ 0.4) is the porosity.

$$F_p = p_m l^2 \tag{B.8}$$

$$F_t = (1-n)(C_{clay,c} + \sigma_{grass,c}(z=-l))l^2 \tag{B.9}$$

$$4F_c = 4(1-n)(C_{clay,c} + \tau_{grass,c})l^2 \tag{B.10}$$

$$F_w = (1-n)(\rho_s - \rho)gl^3 \tag{B.11}$$

C

Appendix: Phases of dike breaching

In the process of dike breaching different phases can be distinguished. Based on experimental research Visser [1998] introduced the 5 phase model, describing different phases of dike breaching. Phase I and II describe the initial failure in this model. d'Eliso [2007] extended this to a description of dike failure consisting of 6 phases, see Figure C.1. Both models state that breaching initiates by failure of the grass cover.

The stages that are distinguished by d'Eliso [2007] are:

1. Failure of the grass due to gradual erosion.
2. Local erosion of the clay cover.
3. Scour erosion and head-cut advance
   (a) Scour erosion and head-cut advance in the clay cover up to sand core exposure to flow action
   (b) Instantaneous sliding of the clay cover, initial breaching channel at the inner slope with bed of sand and slopes of clay.
4. Dike crest shortening due to scour erosion in sand, progressive failure of the clay cover at the crest.
5. Dike lowering
   (a) Dike crest lowering and breach widening due to scour erosion in sand and breach slopes instability, progressive failure of clay cover at the outer slope, driven by wave overtopping.
   (b) Dike crest lowering and breach widening due to scour erosion in sand and breach slopes instability, progressive failure of clay cover at the outer slope, driven by combined flow.
6. Breach widening up to equilibrium final breach

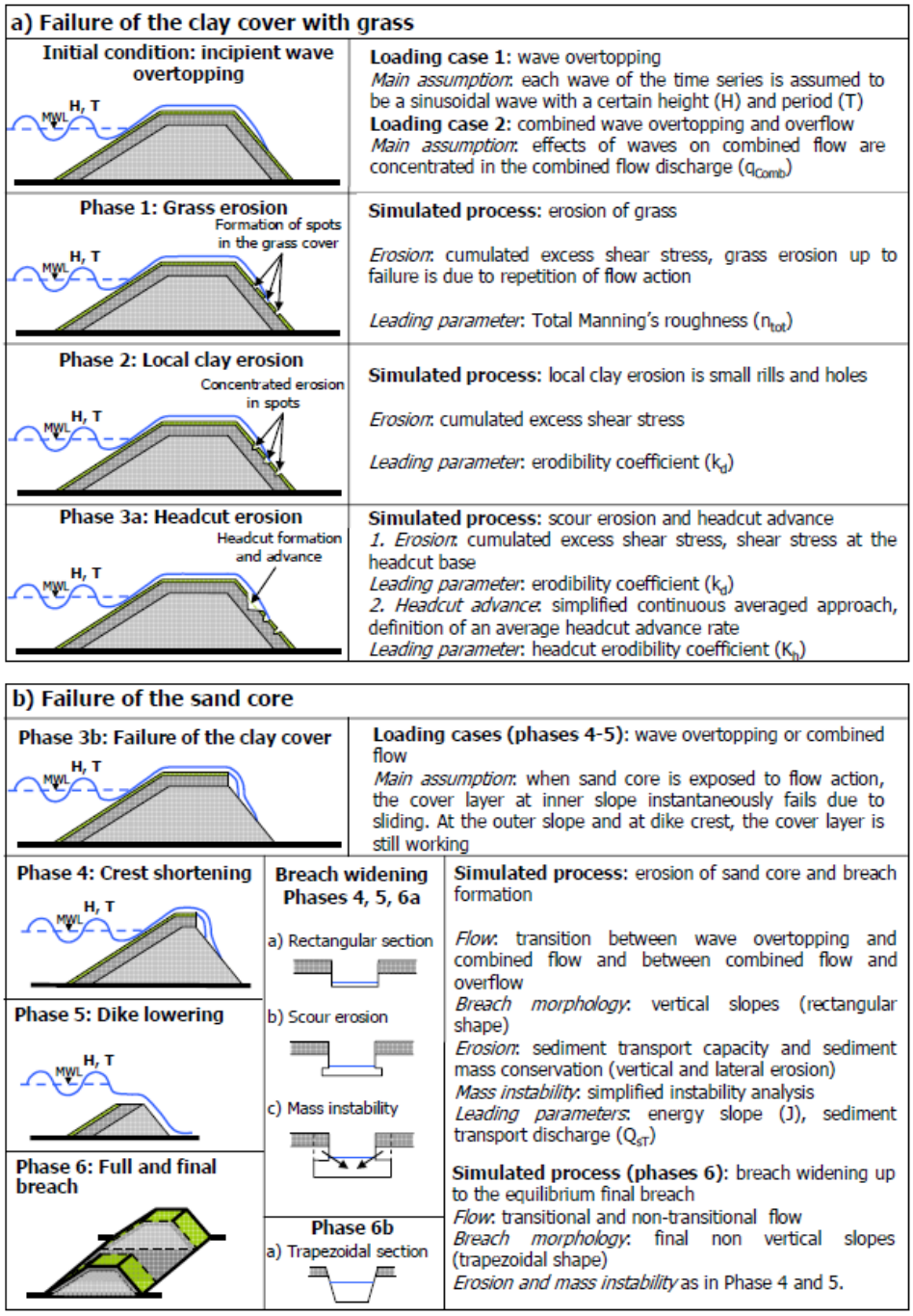

Figure C.1: a) Failure of the clay cover with grass in breaching of a sea dike initiated by wave overtopping. b) Failure of the sand core in breaching of a sea dike initiated by wave overtopping. Modelling phases and simulated processes as described by d'Eliso [2007].

(a) Full breach, breach widening due to scour erosion in sand and breach slopes instability driven by super-critical flow in the breach (transitional flow).

(b) Breach widening due to scour erosion in sand and breach slopes instability up to equilibrium final breach driven by sub-critical flow in the breach (non-transitional flow).

Stage 1, 2 and 3 describe the failure of the grass and clay cover, of which stages 1 and 2

describe the initial failure. van der Meer et al. [2007] distinguishes a fourth step in the cover failure: the erosion of loose material that happens before the failure of the grass. The remainder of the described stages correspond with the first three stages recognized by d'Eliso [2007]. Phase 1 and 2 according to d'Eliso [2007] are in the interest of this research. The processes that play a role in these phases are discussed hereafter.

D

Appendix: Pressure impulse by wave impact

An accurate approach of wave impact forcing is given by the *pressure impulse theory for liquid impact problems* (Cooker and Peregrine [1995]). Accompanying impact stresses are derived from this theory.

D.1 Derivation of pressure impulse forcing

Pressures imposed by an impacting wave deviate from the pressure imposed by a continuous flow (Cooker and Peregrine [1995]). The maximum pressure distribution over the wave impact area in space is not linear, but close to quadratic (Hofland [n.d.]).
The pressure impulse field is given by Equation D.1 and shown in Figure D.1. P is the pressure impulse, z is the distance from the free surface normal to the flow direction, x is the distance from the plane of impact in flow direction, h is the depth of the flow, ρ is the density of water and U_0 is the depth averaged incoming flow velocity. Note that the flow depth corresponds with half the radius of a jet.

The boundary condition at the bottom ($z/h = -1$) is $\partial P/\partial z = 0$. This is valid for the centre line of the jet as well, assuming a symmetrical jet. The boundary condition at the free surface ($z/h = 0$) is $P = 0$. This is valid for the free surface of the jet as well. The boundary condition at the impact plane ($x/h = 0$) is $\partial P/\partial x = \rho U_0$, meaning that the total flow velocity impulse is transmitted from the water to the impact surface.

$$P = \rho h U_0 \sum_{n=1,2\ldots} \frac{-4 \sin\left((n - \frac{1}{2})\pi \frac{z}{h}\right) \exp\left((n - \frac{1}{2})\pi \frac{x}{h}\right)}{(2n - 1)(n - \frac{1}{2})\pi^2} \tag{D.1}$$

The presented pressure impulse field is maximum in the center of the jet. The maximum value is approached by Equation D.2 (Hofland [n.d.]). The impulse is the product of the pressure and the time. Assuming a pressure peak shaped like a right-angled triangle, with a peak at the start and a total duration Δt (a rough version of the approach of

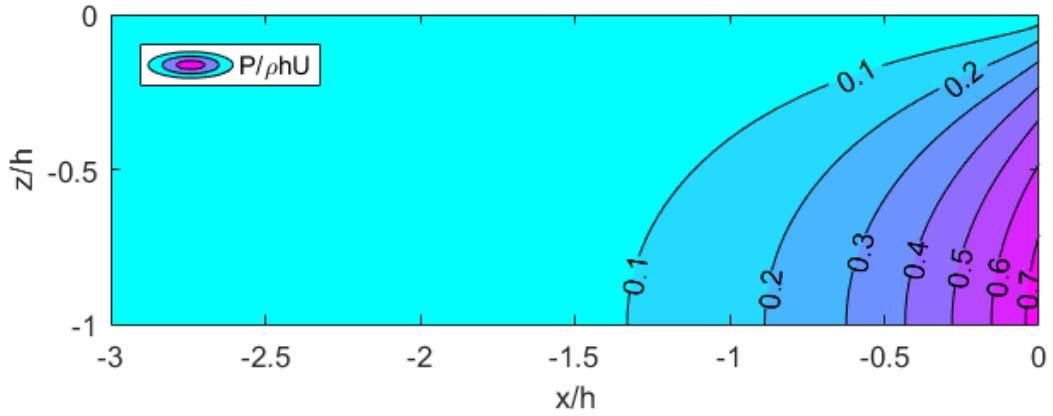

Figure D.1: Pressure impulse field for half a jet impacting on an infinite stiff wall normal to the direction of the jet flow. The center of the jet is at z/h = -1, the free surface of the jet at z/h = 0.

Hughes [2011]), the maximum pressure due to pressure impulse is given by Equation D.3. The total force on the impact plane is found by integrating the impact pressure over the impact plane, giving Equation D.4.

$$P = 0.742\rho h U_0 \tag{D.2}$$

$$p_{max} = \frac{1.484\rho h U_0}{\Delta t} = \frac{1.484\rho q}{\Delta t} \tag{D.3}$$

$$F_P = 0.543\rho h^2 U_0 \tag{D.4}$$

D.2 Effect of impact angle

Section D.1 describes an impact on a wall that is perpendicular to the flow direction. Overtopping waves impact under an angle, comparable with an impact on an inclined wall. The position of the wall influences the boundary condition at the impact side of the computation domain. This influences the forcing. The impact inclination is added to the pressure impulse equations.

Inclined wave impact is schematized as a jet impacting on an inclined wall, as shown in Figure D.2. In this impact not all incoming momentum is stopped, it partly travels along the wall. The fraction of the force that is stopped by the impact, equals the reaction forces of the soil. The normal and shear reaction forces are given by Equations D.5 and D.6 respectively. The resulting shear forces are multiplied by a friction factor (c_f).
For this situation a new boundary condition must be set. The interaction of forces on

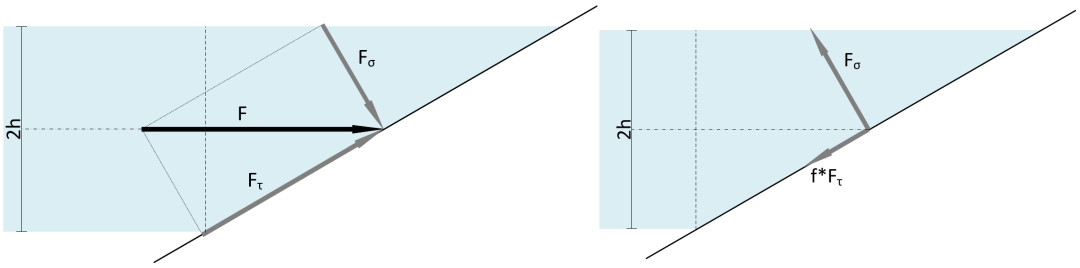

(a) Impact forces. *(b)* Reaction forces.

Figure D.2: Decomposition of the forces of a jet impacting on an inclined surface.

the inclined plane is assumed to be on a plane perpendicular to the centre line of the jet, making the approach compatible with Section D.1. The considered reaction forces are the forces that are in the opposite direction of the incoming jet flow. The boundary condition at the impact side of the domain, state that only the amount of impulse that is transferred to the soil, does not pass the boundary. The impulse travelling along the slope, travels through the boundary. The resulting boundary condition is given in Equation D.7.

$$\sigma = F_P sin\theta \tag{D.5}$$

$$\tau = c_f F_P cos\theta \tag{D.6}$$

$$\frac{\partial P}{\partial x} = \rho U_0 (sin\theta + c_f cos\theta) \tag{D.7}$$

D.3 Demonstration case

To demonstrate the approach an impact case is calculated.

Hughes et al. [2012] shows that for a situation with an average wave overtopping discharge of q = 0.370 m^2/s, the maximum overtopping discharge (q_{max}) is usually lower than 2 m^2/s. The maximum discharge coincides with the the leading edge of the wave. This value is used to determine the normative impact pressure. The use of a maximum value makes assumptions on the total duration of an overtopping wave redundant. For the slope angle 14° is used, which matches a slope with $cot\theta = 4$. For the friction factor a value of 0.1 is assumed.
This case results in a maximum pressure on the wall of 0.880 kN/m^2 in the direction of the flow. Note that this pressure is not normal to the slope surface. The maximum pressure occurs in the center of the jet. The pressure distribution that results from the wave impact in the incoming jet is shown in Figure D.3. Note that the figure gives the stresses in one half of the jet.

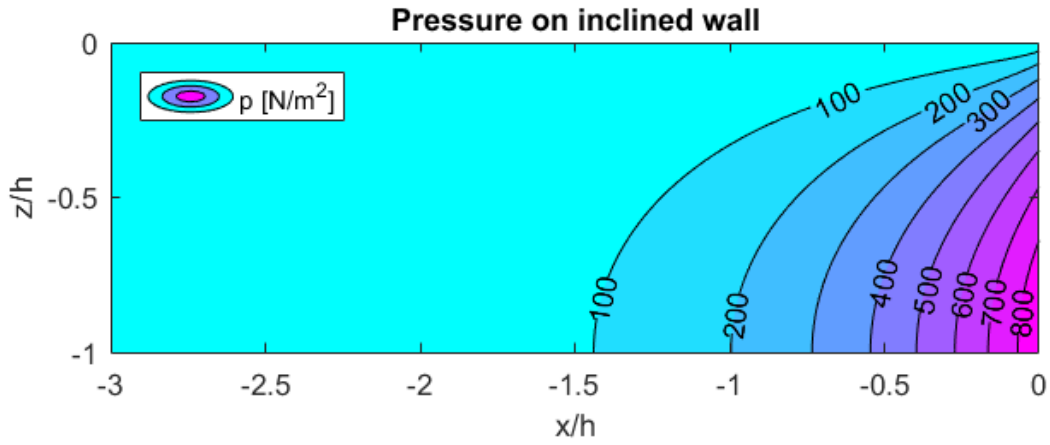

Figure D.3: Pressure field caused by impulse for half a jet impacting on an infinite stiff wall with an inclination with respect to the direction of the jet flow. The center of the jet is at z/h = -1, the free surface of the jet at z/h = 0.

E

Appendix: Comparison with modelling in COMSOL multiphysics

The soil stress model is verificated using *COMSOL multiphysics* computations. Cases with a normal stress of -1000 Pa (pull) on the middle meter of the surface and on the total surface, are computed. Some input parameters for COMSOL differ from the default case in the soil stress model or are not present in it. They are displayed in Table E.1. Another difference in COMSOL is the definition of the boundary conditions. The bottom boundary and the side boundaries have no displacement normal to the boundary. In the soil stress model approach this means that the stresses at both sides of the boundary are equal (derivative of Equation 3.24). The side boundary conditions remain the same, the bottom boundary conditions change to Equations E.1 and E.2.

Table E.1: Deviant and additional model parameter input for the COMSOL model.

Symbol	**Unit**	**Explanation**	**Value**
$I * dx$	m	Model width	10
E	MPa	Young's modulus	15
β_f	Pa^{-1}	Compressibility fluid	$5.0E^{-7}$
n	-	Porosity	0.4

$$\frac{\partial \sigma'}{\partial z} = (\rho_s - \rho)g \tag{E.1}$$

$$\frac{\partial p}{\partial z} = \rho g \cos\theta \tag{E.2}$$

The resulting distributions of the changes in stress, are shown in Figures E.1 and E.2. The results of matching soil stress model runs are shown in Figures E.3 and E.4.

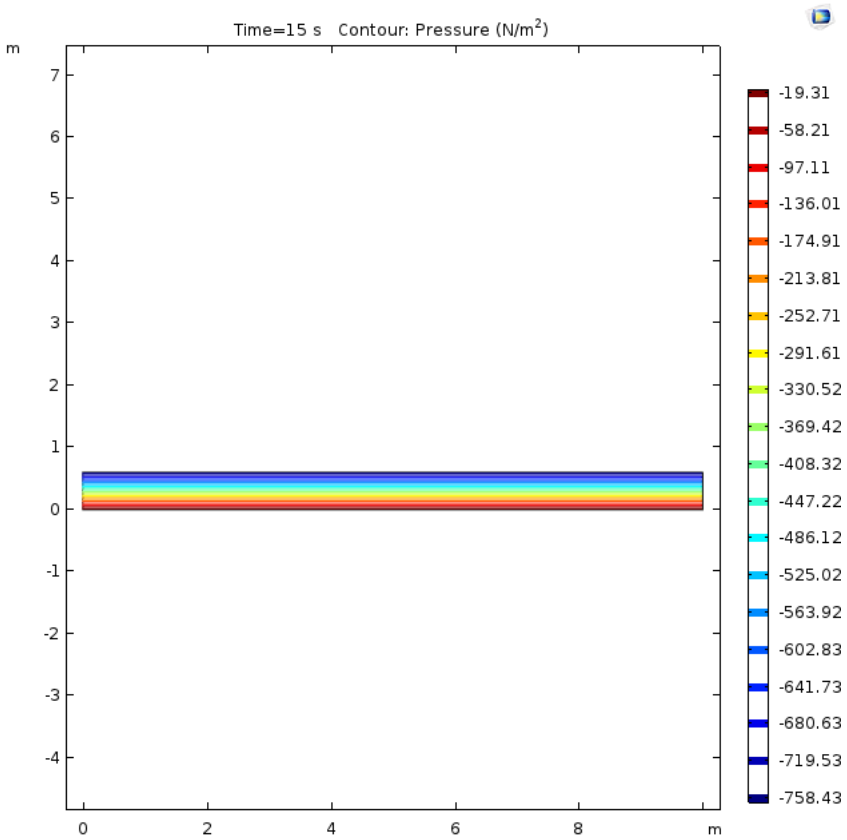

Figure E.1: Distribution of change in effective stress with respect to the initial situation, for a homogeneous surface load of -1000 Pa, after a COMSOL model run of 15 seconds.

Comparison of Figure E.1 with Figure E.3 and Figure E.2 with Figure E.4 shows differences. In general, both the change in stress and the penetration depth of the reaction are larger in the COMSOL results.
Comparison of Figures E.1 and E.3 shows that the soil stress increase at the surface is of comparable value: ≈-600 Pa according to the soil stress model and ≈-750 Pa according to the COMSOL model. The difference is largely caused the calculation grid size.
Figures E.1 and E.3 both show an area of soil stress decrease below the load, of comparable shape. The decreases are of different different magnitude.
Figure E.2 shows a negative surface pressure causing positive soil stress in the soil below the load and in the soil adjacent to the load. Areas of positive and negative soil stress seem to be arranged such that the sum of the soil stress on each horizontal and vertical equals zero. Furthermore, the negative stress in the soil below the load exceed the value of the load.

Comparison of soil stress model results with the COMSOL results show limited similarities, but the difference dominate. Figure E.2 shows behaviour that is not realistic in reality. This indicates that the COMSOL computation is flawed. The origin of the flaw is unknown and can be present in the other COMSOL results as well. It is concluded that this comparison is not suited for verification of the model, due the large amount of differences and the indication of flaws in the COMSOL computation. Considering the limited availability of time within this research, no further effort is put in this verification case.

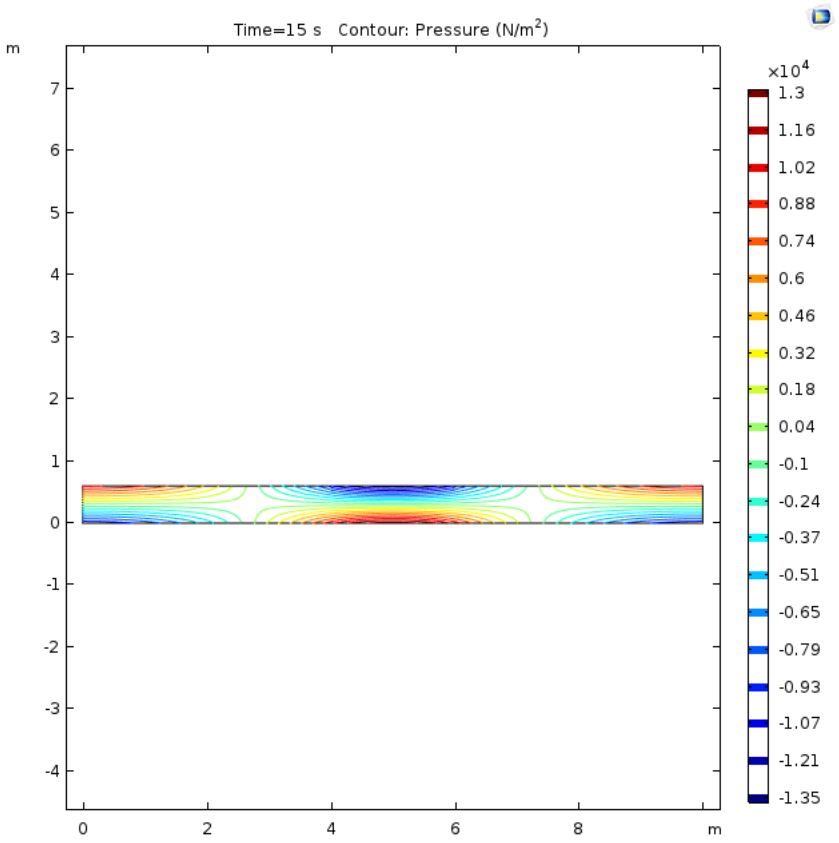

Figure E.2: Distribution of change in effective stress with respect to the initial situation, for a surface load of -1000 Pa at the middle 2 meters of the model surface, after a COMSOL model run of 15 seconds.

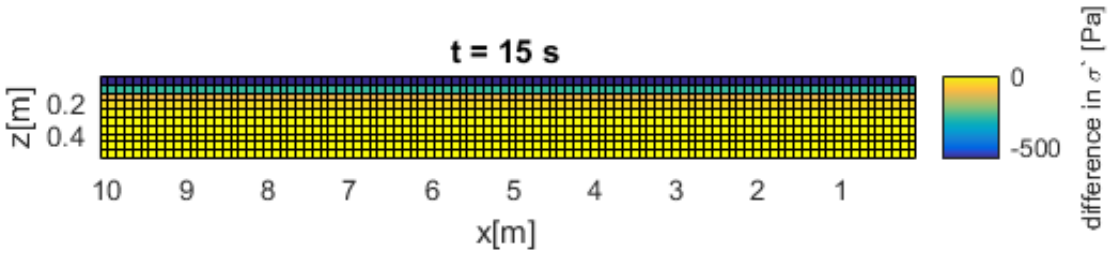

Figure E.3: Distribution of change in effective stress with respect to the initial situation, for a surface load of -1000 Pa, after a model run of 15 seconds.

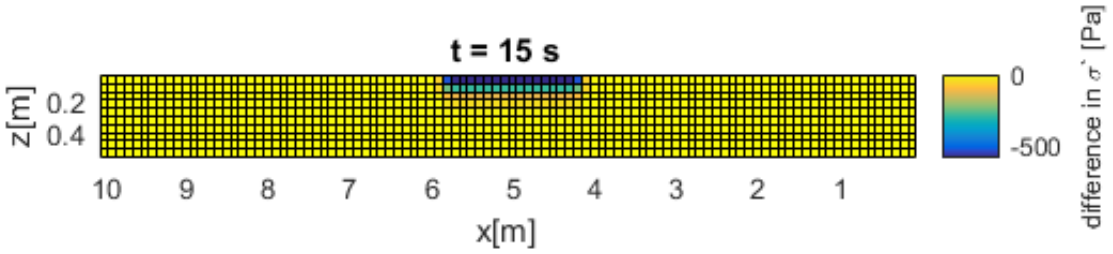

Figure E.4: Distribution of change in effective stress with respect to the initial situation, for a surface load of -1000 Pa at the middle 2 meters of the model surface, after a model run of 15 seconds.